OBSERVATION AND VALIDATION OF METHANE FROM FT-IR OVER ADDIS ABABA.

By

Endale Gemechu

SUBMITTED IN PARTIAL FULFILLMENT OF THE
REQUIREMENTS FOR THE DEGREE OF
MASTER OF SCIENCE IN PHYSICS
AT
ADDIS ABABA UNIVERSITY
ADDIS ABABA, ETHIOPIA
JUNE 2011

ADDIS ABABA UNIVERSITY
DEPARTMENT OF
PHYSICS

Supervisor: _____
Dr. Gizaw Mengistu

Examiners: _____
Dr. Elias Lewi

_____
Professor A.V.Gholap

ADDIS ABABA UNIVERSITY

Date: **June 2011**

Author: **Endale Gemechu**

Title: **OBSERVATION AND VALIDATION OF METHANE FROM FT-IR OVER ADDIS ABABA.**

Department: **Physics**

Degree: **M.Sc.** Convocation: **June** Year: **2011**

Permission is herewith granted to Addis Ababa University to circulate and to have copied for non-commercial purposes, at its discretion, the above title upon the request of individuals or institutions.

Signature of Author

Table of Contents

List of Figures

Abstract

The concentration of methane, the most abundant organic trace gas in the atmosphere has increased dramatically, over the past few centuries, to more than double its value. The increase in its concentration is of special concern because of its effects on climate and atmospheric chemistry. High resolution Mid infra-red (MIR) solar absorption FTIR spectra have been routinely recorded between May 2009 and Nov 2010 at Addis Ababa Observatory (9.01^oN, 38.76^oE). By analyzing the shape of the pressure dependent absorption lines and their different temperature sensitivities, the vertical distribution and column amount of methane is retrieved. Unique time series of the column abundances and volume mixing ratio (vmr) of methane are presented. The effects of both dynamical and chemical seasonally varying trace gas cycles can be seen in the retrieved profiles. These include little variabilities in summer and winter seasons, which is typical of tropical atmosphere. Particular events are selected and origin of air mass flow is identified with the help of Air Resource Laboratory's (ARL) Hybrid Single Particle Lagrangian Integrated Trajectory (HYSPLIT) model. A detailed error analysis has been performed for each profile. The output from Atmospheric Infra-Red Sounder (AIRS) is compared to the total column amount. Results agree well with a correlation coefficient of 0.8.

Acknowledgements

I would like to express my gratitude to my advisor, Dr. Gizaw Mengistu for his support and guidance during my study. I am deeply indebted to him for his many suggestions and constant support during this research. His tireless follow up and consistent support is unforgettable. I am grateful to Milkessa G. and Gezahegn S. for their support in the operation of the FTIR spectrometer, training on LINEFIT software and discussions on the result and for their patience in the elaboration of the retrieval code (PROFFIT), technical support, and discussion of important ideas on the retrieval procedures and results.
My strongest thank is addressed to my Family. I also thank Samuel T., a PhD. student, with whom I have shared and discussed important ideas during the whole measurement time. I am so glad to thank my friend Tadese D. for providing me his PC during the time when I need it very badly. I derived materials from many research journals and books, and I am indebted to the authors of those publications and books.

Introduction

The most general goal in the field of Atmospheric Science is to improve our understanding of, and hence our predictive capabilities regarding, the dynamical and chemical state of the atmosphere. To achieve this goal, atmospheric scientists strive to make computer models of the atmosphere agree well with increasingly precise and accurate observations by including more sophisticated representations of the underlying chemical, micro physical and dynamical processes. Only mature, i.e. validated, models of climate and atmospheric composition can be used with confidence to inform public policy regarding the control and mitigation of human impacts on the environment.

While the general large-scale features of dynamics and chemistry in the atmosphere and many small-scale micro physical features are captured by current models, outstanding questions remain unanswered. In order to identify missing or poorly represented processes in atmospheric models, there exists a global Earth observation effort using satellite, aircraft, balloon and ground-based platforms. The role of ground-based observatories is to provide long-term high-quality correlative measurements of trace gases, aerosols, and dynamical variables, which can be used for unique scientific studies (both long-term and short-term), as well as for satellite and model validation.

In this context, the Addis Ababa University Science Faculty FTIR Spectrometer Observatory was established in 2009, and has since become a Complementary Station in the international Network for the Detection of Atmospheric Composition Change (NDACC/IRWG), formerly known as the Network for the Detection of Stratospheric Change (NDSC) described by Kurylo and Zander [**1**] and shown in Fig. 1.

Figure 1: Global distribution of IRWG Stations(http://www.acd.ucar.edu.irwg).

The goal of this study is the implementation of retrieval algorithms and derivation of vertical profile, seasonal total and partial columns of a trace gas methane (CH_4) from the infrared solar absorption spectra recorded by the spectrometer after optimizing the retrieval procedure for Addis Ababa's FTIR Spectrometer. In addition, part of this dataset is compared to other observations (Atmospheric Infra Red Sounder or AIRS), as appropriate or available, and several case studies of particular events are undertaken.

Atmospheric methane, one of the major greenhouse gases absorbs IR radiation and emits thereby increasing the the global warming. Recent studies have shown that the concentration of atmospheric methane has increased more than double since the industrial revolution [16]. The main sources of atmospheric methane are of anthropogenic origin such as agriculture, animal husbandry, rise cultivation, land fills, biomass burning and so on.

The remainder of this thesis is structured as follows. In Chapter 1 an introduction to planetary atmospheric structure and chemistry is given. In Chapter 2 we introduce the radiative transfer theory. Here the mathematical formulation of radiative transfer in the Earth's atmosphere is discussed in detail. Chapter 3 deals with the general trends (sources, sinks)

and global impacts of methane . In chapter 4 we present the experimental set up and techniques implemented to gather datasets used in the retrieval. Chapter 5 specifically deals with computational costs associated with atmospheric inverse sounding and presents a computationally efficient methods. Chapter 6 contains details of the experimental results and discussions. In addition, this chapter includes validation of the experimental results with satellite data. Finally in chapter 7 summary of the results and conclusion is presented.

Chapter 1

The Earth's atmosphere, structure and chemistry

For a complete understanding of the atmosphere, we need to know about its evolution and the processes which have determined its mass and its composition. We also need to know about its physical structure and the distribution of density, composition and motion within the atmosphere. Further because of our concern about climatic change, it is necessary to understand the factors which determine the average state of the atmosphere over periods of years and centuries.

Much of the current level of interest in the Earth's atmosphere has to do with the fact that it is perceptibly changing at present, and the accumulated change over a period of time is thought likely to have serious consequences on the habitability of the planet as a whole. From this perspective, it is imperative to study the natural and anthropogenic effects on the atmosphere.

1.1 Chemical composition of the atmosphere

The objective of atmospheric chemistry is to understand the factors that control the concentrations of chemical species in the atmosphere. The atmosphere is a relatively stable mixture of gases, during the day, the proportion of which, excluding water vapor are uniform up to approximately 80 km above the Earth's surface [2].

The major components of the atmosphere by volume are oxygen (21%), nitrogen (78%) and argon (0.93%), which have not varied significantly in abundance over the last several millenia at least and are not expected to vary much in the foreseeable future. Furthermore, these three gases each contain atoms of a single element and so possess molecular symmetries that prevent them from absorbing or emitting infra-red radiation under most conditions of temperature and pressure found in the Earth's atmosphere. These gases do affect the propagation of solar radiation through the process of Rayleigh scattering and hence contribute to global cooling of the planet despite the fact that they do not contribute directly to the greenhouse effect. They do moderate the greenhouse effect indirectly, as the atmospheric pressure they produce affects the efficiency by which the infra-red-active molecules absorb the Earth's thermal radiation emitted to space.

The atmosphere is thought of as a dynamic system, with its gaseous constituents continuously being exchanged with vegetation, oceans and biological organisms. The cycle of atmospheric gases involve a number of physical and chemical processes. Gases are produced chemically by biological activity, volcanic eruption, radioactive decay and human activity, while, removal is through chemical reactions, physical processes and deposition. Also present are a number of trace gases that occur relatively in small amount and sometimes highly variable amounts. Even with this remarkably small composition, temperature and atmospheric chemistry are believed to be controlled by the trace gases. There is evidence that environmentally significant trace gases are changing because of both natural and human factors. Carbon dioxide (CO_2), nitrous oxide (N_2O) and methane (CH_4) are changing in concentration through actions like the burning of fossil fuels, biomass burning, release from metabolic processes of micro-organisms in the soil, industries, traffic and oceans of the planet.

In the present terrestrial atmosphere, the trace gases, water vapor (H_2O), carbon dioxide (CO_2), methane (CH_4), nitrous oxide (N_2O) and ozone (O_3), are the main greenhouse gases [2]. The man-made chlorofluorocarbons (CFCs), associated with cosmic sprays and refrigeration also contribute to the present greenhouse effect. These are minor constituents of the atmosphere in terms of abundance, and, unlike the major constituents, these abundances are prone to change. CO_2, CH_4, N_2O and CFCs have increased systematically within the past century. Water-vapor abundance is largely controlled by the ocean surface, temperature and transport processes, and the global distribution of its atmospheric concentration is highly variable.

There is increasing evidence that the percentages of trace gases are changing because of both natural and human factors. Some of the gases do not have uniform mixing ratios (e.g. ozone, water vapor, etc.) in the lowest 100 km. They can have a source at the surface or in the atmosphere or, a sink at the surface or in the atmosphere. If the gas's lifetime is shorter than the time it takes to get transported from one place to another, then the gas may not be uniformly distributed throughout the atmosphere. Table 1.1 lists the mixing ratios of some major atmospheric gases.

As shown in the Table, nitrogen and oxygen are the two main constituents of the Earth's atmosphere with their combined proportions approaching almost 99% by mass as well as by volume. Their compositions vary little with time, so they are treated as permanent gases. Other gases exist in small amounts only. The proportions of carbon dioxide and ozone are variable. Water vapor, carbon dioxide and ozone, though they occur in small proportions, play very important roles in atmospheric processes because of their radiative and thermodynamic properties. Minor constituents at low levels of the atmosphere may include variable quantities of dust, smoke and toxic gases and vapors such as sulfur dioxide, methane, oxides of nitrogen, etc., some of which pollute the atmosphere and are highly toxic.

Table 1.1: List of some major and trace atmospheric gases
(http://www.buzzle.com/articles/earth's-atmosphere)

Species	Relative abundance(ppbv)	Source	Comment
N_2	7.81×10^8	biological	long lived
O_2	2.10×10^8	biological	long lived
H_2O	$10^6 - 10^7$	physical	long lived
Ar	9.34×10^6	radiogenic	permanent
CO_2	3.5×10^5	biological industrial	variable increasing
Ne	1.8×10^4	interior	permanent
He	5.2×10^3	radiogenic	escaping
CH_4	1.70×10^3	biological	variable, increasing
Kr	1.0×10^3	interior	permanent
H_2	5.0×10^2	biological photochemical	variable
N_2O	3.0×10^2	biological industrial	increasing
CO	1.0×10^2	photochemical industrial	variable increasing
SO_2	$< 10^2$	industrial photochemical	variable
O_3	$< 10^2$	photochemical	variable
Xe	9×10^1	interior	permanent
NO,NO_2,NO_x	variable,	industrial biological	
CH_3Cl	6.0×10^{-1}	biological	short lived
CCl_2F_2(CFC-12)	2.9×10^{-1}	industrial	increasing
CCl_3F(CFC-11)	1.7×10^{-1}	industrial	increasing
CCl_4	1.2×10^{-1}	industrial	increasing
CH_3CCl_3	9.8×10^{-2}	industrial	increasing
CF_4	7.2×10^{-2}	industrial	increasing
CH_3Br	1.0×10^{-2}	biological industrial	possibly increasing

1.2 Regions and characteristics of the atmosphere

The gaseous area surrounding the planet is divided in to several concentric spherical layers or strata, and are characterized by differences in chemical composition. Fig. 1.1 shows the different regions of the atmosphere.

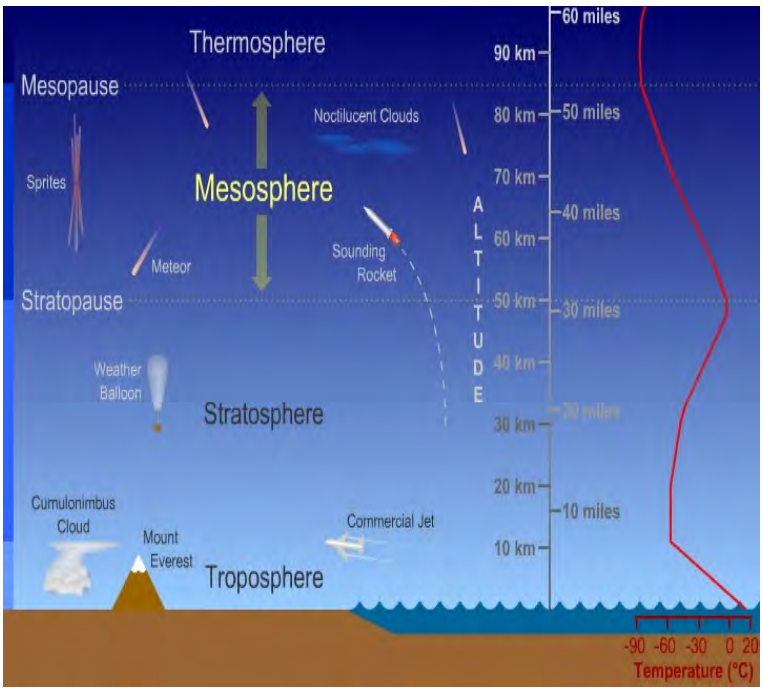

Figure 1.1: The layers of the atmosphere.
(http://www.windows2universe.org/earth/Atmosphere/images.html)

1.2.1 Troposphere

The troposphere (region of mixing) because of the vigorous convective air current within the layer is the atmospheric layer closest to the planet and contains the largest percentage of the mass of the total atmosphere. The surface layer of the atmosphere is known as the planetary boundary layer, which extends vertically to between a few hundred meters and about 2 km. This layer interacts directly with the Earth's surface so it is important for transfer of surface emissions in to the troposphere. Emitted species become very well mixed in the boundary layer and are then mixed out in to the free troposphere.

Chemical, physical and biological processes play a central role in determining the behavior and composition of the Earth's troposphere. The chemical transformations that occur in the atmosphere contribute to the changes in the distribution of trace gases (e.g. ozone), and so affect other atmospheric systems. Approximately 10% of total atmospheric ozone resides in the lower atmosphere, where it serves as a greenhouse gas in the upper troposphere. However, in the lower troposphere, ozone is a pollutant which is harmful to plants and animals because of its toxicity [3].

The upper boundary layer ranges in height from 8 km to 17 km above the equator. Its height varies with seasons: highest in the summer and lowest in the winter. Temperature decreases with altitude, however, within the tropopause which separates the troposphere from the stratosphere, temperature remains constant.

1.2.2 Stratosphere

The stratosphere is the second major stratum of air in the atmosphere. It resides between 10 km and 50 km above the planet's surface. The air temperature in the stratosphere increases gradually with altitude to 200-220K. Because the the air temperature in the stratosphere increases with altitude, it doesn't cause convection and has a stabilizing effect on atmospheric conditions in the region. Ozone plays the major role in regulating thermal regime of the stratosphere. Solar energy is converted to kinetic energy when ozone molecules absorb ultraviolet (UV) radiation in the wave length range from 290 nm to 320 nm, resulting in heating of the stratosphere. The ozone layer is located at an altitude of approximately 10-35 km, and 90% of the ozone in the atmosphere resides in the stratosphere. Meteorological conditions strongly affect the distribution of ozone. Most ozone production and destruction occurs in the tropical upper stratosphere, where the largest amounts of ultraviolet radiation are present [2].

1.2.3 Mesosphere

Moving upward, the next layer is the mesosphere. At this height the atmosphere is very thin. Temperature once again decline with increasing altitude (as was the case in the troposphere), falling as -100^{o}C (-146^{o}F) in the upper mesosphere. This layer is relatively poorly studied, for it is above the reach of most aircraft and ground based instruments but below where satellites orbit. Most meteors burn up in the mesosphere. The top of the mesosphere lies about 80 to 85 km above the earth's surface.

1.2.4 Thermo sphere

Above the mesosphere lies the extremely tenuous thermo sphere. This layer is so thin, in fact, that many satellites orbit within it. This region is one in which temperature once again rises with increasing altitude reaching as high as 2,500^{o}C (4,500^{o}F) in the day time. Embedded within the thermo sphere are several layers of the ionosphere: regions where ionized gas particles can reflect radio waves, a feature that people used to send message beyond the line-of-sight range of the horizon before the advent of satellites. The thermo sphere extends to somewhere between 500 and 1,000 km above the Earth's surface. Many of the atoms and molecules in the thermo sphere (and above) have lost electrons and thus becoming electrically charged ions; so the motion of particles in the upper atmosphere are partially influenced by electrical currents and the Earth's magnetic field.

Though not universally recognized as a layer of our atmosphere, some scientists consider the exosphere to be the outer most layer of the Earth's atmosphere. Starting at the top of the atmosphere, this extremely tenuous layer gradually gives a way to the vacuum of interplanetary atmosphere.

1.3 Solar electromagnetic radiation penetration into the Earth's atmosphere

The Sun emits a broad range of frequencies, from high energy x-rays and UV radiation through visible light, on down the spectrum to the lower energy infrared and radio waves. Different wavelengths of this solar radiation behave differently as they enter the earth's atmosphere. All of the high-energy x-rays are absorbed by the atmosphere well above our heads which is very fortunate for us indeed! Likewise, most of the UV radiation (especially the highest energy shortest wavelength regions of the UV spectrum) is blocked by the thermo sphere, mesosphere and stratosphere. The relatively low energy long wavelength portion of the UV spectrum that does reach the ground forces us to wear sunglasses and cover ourselves with sunscreen to protect from sunburn and skin cancer.

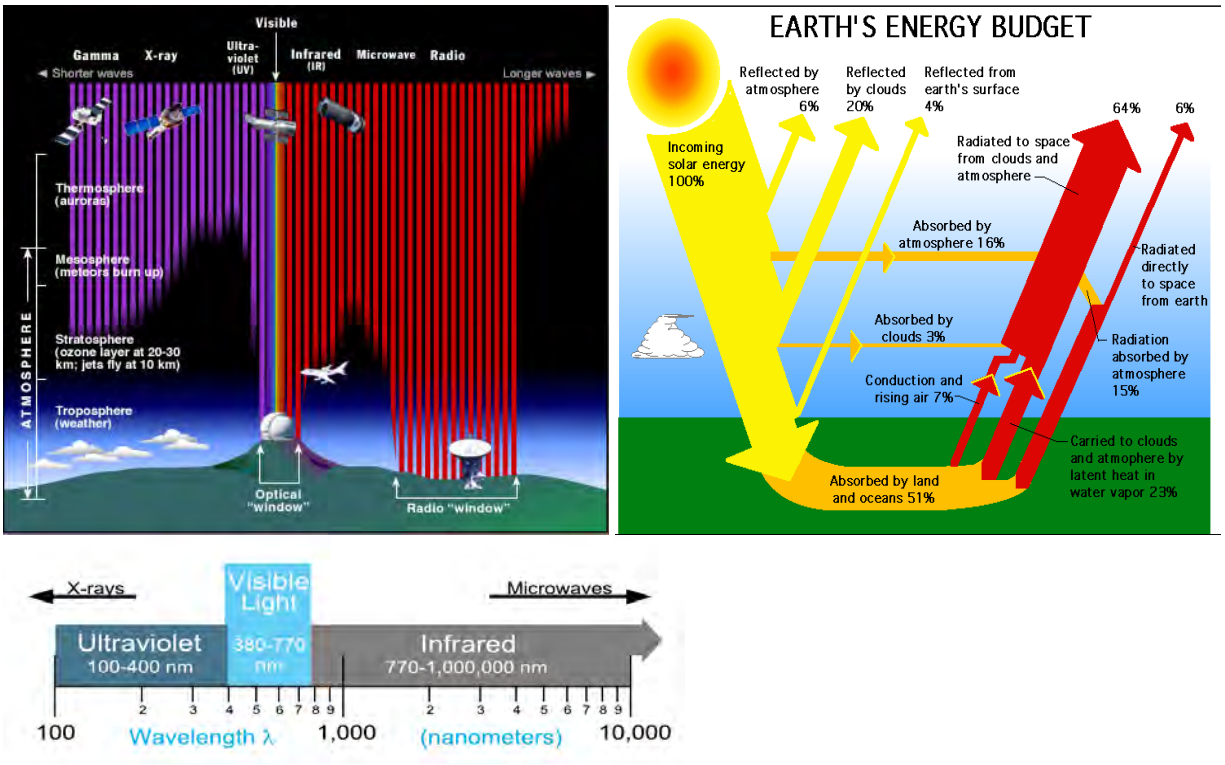

Figure 1.2: Solar EM radiation penetration into the earth's atmosphere (left), the Earth's energy budget (right) **Credit**:image NASA's Earth Radiation Budget Experiment program.

A relatively narrow "window" of electromagnetic wavelengths around visible light reaches the ground. It includes some of the longer UV frequencies, some of the shorter IR frequencies and all of the visible light region of the spectrum. Most of the longer wavelength IR waves and many of the shorter radio waves are absorbed by the stratosphere before reaching the ground. There is a sizable "radio window" of radio wave frequencies that also reach terra firma (solid earth). The longest wavelength radio waves also fail to penetrate the atmosphere; many are absorbed or reflected by the ionosphere.

The temperature of the various layers of the Earth's atmosphere rises and falls as one moves upward from the ground in a seemingly haphazard fashion. First the temperature drops as we move upward through the troposphere; then it rises as we rise through the stratosphere; then it falls again through the mesosphere, only to rise again in the thermo sphere. What is going on here? Near the Earth's surface, the Sun light that does reach the ground warms the Earth which in turn warms the air immediately above it. So the troposphere is warmest next to the warm ground, and cooler higher up away from the warm ground.

However, in the stratosphere, the ozone layer is especially good at absorbing UV radiation; which shields us from most of these high-energy rays, and also heats this layer as the UV photons transfer their energy to the unusual type of oxygen molecules (O_3). The air varies in its chemical composition at different altitudes; and various chemical species absorb different wavelengths of EM radiation preferentially. Whenever there is the right combination of certain chemicals, and an abundance of radiation of a type that those chemicals are good at absorbing, the atmosphere absorbs a lot of energy and its temperature rises.

Just as certain elements emit specific wavelengths of EM radiation, certain elements and compounds preferentially absorb certain specific wavelengths.

1.4 The Greenhouse effect

Most of the solar radiation that reaches the Earth or its lower atmosphere, where albedo from clouds and features on the ground come into play is thus, in the form of visible light. So what is the fate of that Sun light? Averaged over the surface of the Earth's globe about 342 Wm^{-2} of energy reaches the top of the Earth's atmosphere. Although the atmosphere blocks out much of the range of the Sun's EM emissions at various altitudes, the bulk of EM radiation from the sun in the form of visible light does reach at least as far as the troposphere.

Earth's overall average albedo, including clouds, is around 0.3 (30%). So about 30% of the incoming sun light is reflected back into space by clouds or light areas on the Earth's surface, or scattered back out into space by gas molecules in the atmosphere (that scattering is what makes the sky blue). Of the 70% that makes it through, about $2/3^{rd}$ makes it to the ground, while $1/3^{rd}$ is absorbed or reflected by clouds. When the ground or cloud absorbs sun light, it heats up. Anything that is warmer than absolute zero emits infrared radiation. So both the ground and the cloud emit in IR wavelengths. At this point a critical player in the atmospheric phenomena enters the scene-the greenhouse effect.

Some substances are transparent to certain wavelength's of EM radiation, but largely opaque to others. Such is the case with the panes of glass in the greenhouse. Sun light readily passes in, providing energy needed for photosynthesis and warming inside of the greenhouse; but the IR radiation that the warmed interior emits does not readily pass back out through the glass, for the glass is largely opaque at the IR frequencies. Thus the greenhouse traps in the IR radiation and stays quite warm, even on a winter day.

Earth's atmosphere is much like the glass in the greenhouse. Our atmosphere is opaque across much of the IR spectrum. Fig. 1.2 shows how much of the IR radiation from the Sun fails to make it to the ground.

On the way in, most of the EM radiation is in the form of visible light, which easily passes through clear air. On the way back however, much of the radiation is in the form of IR, which is absorbed and thus stopped before it reaches space. Earth's atmosphere, like the panes of glass in the greenhouse, traps much of the IR radiation, and heat that it carries, warming our planet. Several different gases play a role in this greenhouse effect; water vapor, carbon dioxide and methane are amongst the most prominent.

As IR radiation from the ground and low-lying clouds works its way up through the atmosphere, much of it is absorbed by gases in the air and by clouds (which have lots of IR opaque water vapor). The atmosphere and clouds warm once again emitting IR radiation. Some of that radiation goes upward escaping into space, but some goes downward, further warming the ground and the lower atmosphere. This cycling of the IR radiation's energy through the lower atmosphere warms our planet to a much more comfortable temperature.

1.5 Oxidizing power of the troposphere

The atmosphere is an oxidizing medium. Many environmentally important trace gases are removed from the atmosphere mainly by oxidation: greenhouse gases such as CH_4, toxic combustion gases such as CO, agents for stratospheric O_3 depletion such as HCFCs and others. Oxidation in the troposphere is of key importance because the troposphere contains the bulk of atmospheric mass (85%) and because gases are generally emitted at the surface.

The most abundant oxidants in the Earth's atmosphere are O_2 and O_3. These oxidants have large bond energies and are hence relatively nonreactive except toward radicals (O_2 only towards highly unstable radicals). With a few exceptions, oxidation of non-radical atmospheric species by O_2 or O_3 is negligibly slow. Work in 1950s first identified the OH radical as a strong oxidant in the stratosphere. OH reacts rapidly with most reduced

non radical species, and particularly reactive toward H-containing molecules due to H-abstraction reactions converting OH to H_2O [4].

Production of OH is by reaction of water vapor with $O(^1D)$:

$O_3 + h\nu \rightarrow O_2 + O^1D \qquad (R_1)$

$O^1D + M \rightarrow O + M \qquad (R_2)$

$H_2O + O^1D \rightarrow 2OH \qquad (R_3)$

A simple expression for the source P_{OH} from reactions (R_1)-(R_3) can be obtained by assuming steady state for $O(^1D)$. According to WMO [4] reaction R_2 is much faster than R_3 at the H_2O mixing ratios found in the atmosphere, allowing for simplification:

$$\begin{aligned} P_{OH} = 2k_3[O(^1D)][H_2O] &= \frac{2k_1k_3}{k_2[M] + k_3[H_2O]}[O_3][H_2O] \\ &\approx \frac{2k_1k_3}{k_2[M]}[O_3][H_2O] \end{aligned} \tag{1.5.1}$$

Critical to the generation of OH is the production of $O(^1D)$ atoms by reaction (R_1). Until 1970 it was assumed that the production of $O(^1D)$ would be negligible in the troposphere because of near total absorption of UV radiation by the O_3 column overhead. It was thought that oxidation of species emitted from the Earth's surface, such as CO and CH_4, required transport to the stratosphere followed by reaction with OH in the stratosphere:

$CO + OH \rightarrow CO_2 + H_2 \qquad (R_4)$

$CH_4 + OH \rightarrow CH_3 + H_2O \qquad (R_5)$

This mechanism implied long atmospheric life times for CO and CH_4 because air takes on average 5-10 years to travel from the troposphere to the stratosphere and the stratosphere accounts for only 15% of the total atmospheric mass [5]. Later concern emerged that accumulation of CO emitted by fossil fuel combustion would soon represent a global air pollution problem.

1.5.1 The hydroxyl radical

Sufficient OH produced in the troposphere by reactions (R_1)-(R_3) allows for oxidation of species such as CO and CH_4 within the troposphere. Tropospheric production of $O(^1D)$ takes place in a narrow wavelength band between 300 and 320 nm; radiation of shorter wavelengths doesn't penetrate into the troposphere, while radiation of longer wavelengths is not absorbed by ozone. Although the production of $O(^1D)$ in the troposphere is considerably slower than in the stratosphere, this is compensated in terms of OH production by the larger H_2O mixing ratios in the troposphere (102-103 times higher than in the stratosphere) [5].

1.5.2 Global mean OH concentration

The life time of OH in an air parcel is given by

$$\tau_{OH} = \frac{1}{\sum_i k_i n_i} \tag{1.5.2}$$

where n_i is the number density of species i reacting with OH, k_i is the corresponding rate constant, and the sum is over all reactants in the air parcel. One finds that CO is the dominant sink of OH in most of the troposphere, and CH_4 is next in importance.
The resulting life time of OH is of order of one second [2]. Because of this short life time, atmospheric concentrations of OH are highly variable; they respond rapidly to changes in the sources or sinks. Calculating the atmospheric life times of gases against oxidation by OH requires a knowledge of OH concentrations averaged approximately over time and space. This averaging can not be done from a direct OH measurements because OH concentrations are so variable. An impossibly dense measurement network would be required. In the late 1970s it was discovered that the industrial solvent, methyl chloroform (CH_3CCl_3) could be used to estimate the global mean OH concentration. The source of CH_3CCl_3 to the atmosphere is exclusively anthropogenic [2]. The main sink is oxidation by OH in the troposphere (oxidation and photolysis in the stratosphere and uptake by the oceans,

provide small additional sinks). The concentration of CH_3CCl_3 in surface air has been measured continuously at world wide network of sites.

Rapid increase of CH_3CCl_3 was observed in the 1970s/80s due to rising industrial emissions, but concentrations began to decline later because CH_3CCl_3 was one of the gases banned by the Montreal protocol to protect ozone layer. Although only a small fraction of CH_3CCl_3 is oxidized or photolized in the stratosphere, the resulting Cl radical source was sufficient to motivate the ban.

Industry statistics provides a reliable historical record of the global production rate P (moles yr^{-1}) of CH_3CCl_3 and it is well established that essentially all of this production is volatilized to the atmosphere within a few years [4]. The global mass balance equation for CH_3CCl_3 in the troposphere is

$$\frac{dN}{dt} = P - L_{trop} - L_{strat} - L_{ocean} \tag{1.5.3}$$

where N is the number of moles of CH_3CCl_3 in the troposphere, L_{trop} is loss rate of CH_3CCl_3 in the troposphere, L_{strat} and L_{ocean} are the minor loss rates of CH_3CCl_3 in the stratosphere and to the ocean respectively. We calculate L_{trop} as

$$L_{trop} = \int_{trop} k(T) C n_a [OH] dv \tag{1.5.4}$$

where k(T) is the temperature dependent rate constant for oxidation of CH_3CCl_3 by OH, C is the mixing ratio of CH_3CCl_3, n_a is the air density and the integral is over the tropospheric volume.

We define global mean OH concentration in the troposphere as

$$[\bar{OH}] = \frac{\int_{trop} k(T) n_a [OH] dv}{\int_{trop} k(T) n_a dv} \tag{1.5.5}$$

where $k(T)n_a$ is an averaging kernel (weighting factor) for the computation of the mean. Replacing Eqs. (1.5.3) and (1.5.4) into Eq. (1.5.5) yields

$$[\bar{OH}] \approx \frac{P - \frac{dN}{dt}}{C \int_{trop} k(T) n_a dv} \tag{1.5.6}$$

where we have assumed C to be uniform in the troposphere and neglected the minor terms L_{strat} and L_{ocean}.

All terms on the RHS of Eqn. (1.5.6) are known. The values of C and $\frac{dN}{dt}$ can be inferred from atmospheric observations. The integral $\int_{trop} k(T) n_a dv$ can be calculated from laboratory measurements of k(T) and climatological data for tropospheric temperature. Substituting numerical values this gives $[\bar{OH}] = 1.2\text{x}10^6$ molecules cm^{-3} [5].

This empirical estimate of the concentration of OH is useful because it can be used to estimate the life time $t_i = \frac{1}{k_i[OH]}$ of any long lived gas i against oxidation by OH in the troposphere. For example, one infers a life time of 9 years for CH_4 and a life time of 2 years for methyl bromide (CH_3Br) [5]. One can also determine the atmospheric life times of different hydrochlorofluoro carbons (HCFC) species and hence the fraction of these species that penetrate into the stratosphere to destroy ozone.

1.5.3 Cycling of HO_x and production of ozone

When the the importance of OH as a tropospheric oxidant was first realized, it was thought that O_3 molecules necessary for OH production would be supplied by transport from the stratosphere. The chemical life time of O_3 in the lower stratosphere is several years, sufficiently long to allow transport of O_3 to the troposphere. The transport rate F of O_3 across the tropopause is estimated to be 1-2x10^{13} molecules yr^{-1} [5]. One can make a simple argument that this supply of O_3 from the stratosphere is in fact far from sufficient to maintain tropospheric OH levels. Each O_3 molecule crossing the tropopause can yield at most two OH molecules in the troposphere by reactions $(R_1) + (R_3)$, some of the O_3 is consumed by other reactions in the troposphere and some is deposited at the Earth's surface. The resulting maximum source of OH is 2-4x10^{13} molecules yr^{-1}. In comparison the global source of CO to the atmosphere is 6-10x10^{13} molecules yr^{-1} and the global source of CH_4 is about 3x10^{13} molecules yr^{-1}. There are therefore, more molecules of CO and CH_4 emitted to the atmosphere each year than can be oxidized by

OH molecules originating from O_3 transported across the tropopause [6].

In the absence of additional sources, OH would be titrated; CO, CH_4, HCFCs and other gases would accumulate to very high levels in the troposphere, with catastrophic environmental implications.

A key factor preventing this catastrophe is the presence in the troposphere of trace levels of NO_x (NO + NO_2) originating from combustion, lightning and soils. The presence of NO_x allows the regeneration of OH consumed in the oxidation of CO and hydrocarbons and concurrently provides a major source of O_3 in the troposphere to generate additional OH.

1.6 CO oxidation mechanism

Oxidation of CO by OH produces the H atom which reacts rapidly with O_2: $CO + OH \rightarrow CO_2 + H$.

$H + O_2 + M \rightarrow HO_2 + M \qquad (R_6)$.

The resulting HO_2 radical can self react to produce hydrogen peroxide (H_2O_2),

$HO_2 + HO_2 \rightarrow H_2O_2 + O_2 \qquad (R_7)$.

H_2O_2 is highly soluble in water and is removed from the atmosphere by deposition on a time scale of a week. It can also photolyze or react with OH:

$H_2O_2 + h\nu \rightarrow 2OH \qquad (R_8)$

$H_2O_2 + OH \rightarrow HO_2 + H_2O \qquad (R_9)$

Reaction (R_8) regenerates OH, while (R_9) consumes additional OH. In the presence of NO, an alternate reaction for HO_2 is

$HO_2 + NO \rightarrow OH + NO_2 \qquad (R_{10})$

which regenerates OH and also produces NO_2 which goes on to photolyze as

$NO_2 + h\nu \xrightarrow{O_2} NO_2 + O_3 \qquad (R_{11})$

Reaction (R_{11}) regenerates NO and produces an O_3 molecule which can then go on to photolyze by reactions (R_1)-(R_3) to produce two additional OH molecules. Reaction (R_{10}) thus yields up to three OH molecules boosting the oxidizing power of the atmosphere. The sequence of reactions (R_4) + (R_6) + (R_{10}) + (R_{11}) is a chain mechanism for O_3 production in which the oxidation of CO by O_2 is catalyzed by HO_x chemical family (HO_x = H+OH+HO_x) and by the NO_x.

$$CO + OH \xrightarrow{O_2} CO_2 + HO_2$$

$$HO_2 + NO \rightarrow OH + NO_2$$

$$NO_2 + h\nu \xrightarrow{O_2} NO + O_3.$$

The resulting net reaction is

$$CO + 2O_2 \rightarrow CO_2 + O_3$$

The chain is initiated by the source of HO_x from reaction (R_3) and is terminated by the loss of the HO_x radicals through reaction (R_7). The propagation efficiency of the chain (chain length) is determined by the abundance of NO_x. A diagram of the mechanism emphasizing the coupling between the O_3, HO_x and NO_x cycles, hydrocarbons and some climatically important tropospheric species is shown in the figure below.

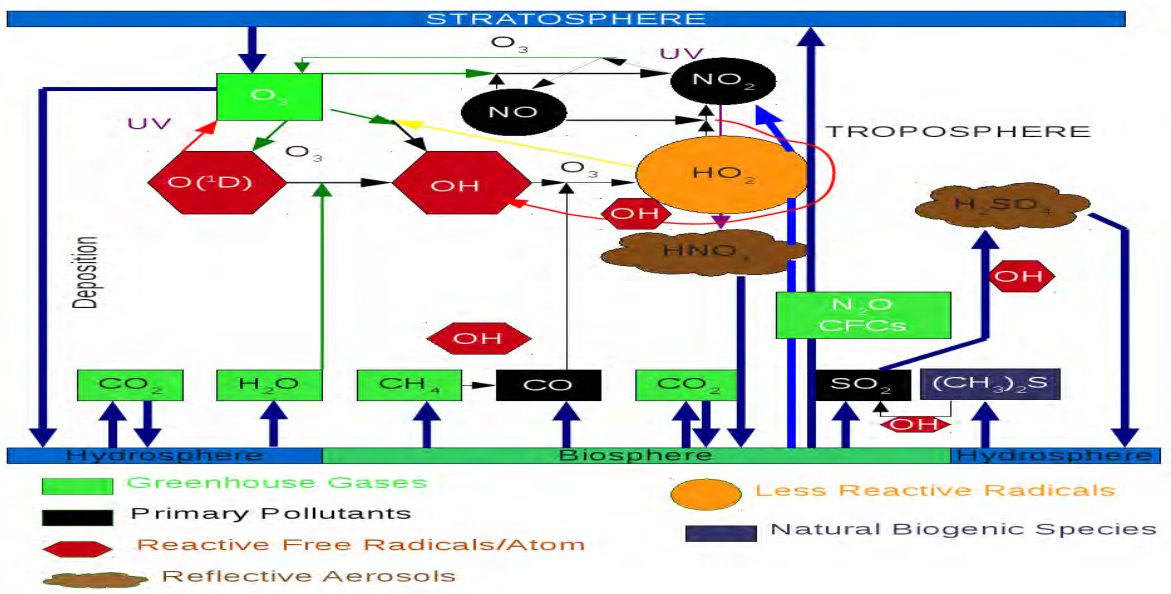

Figure 1.3: Coupling of climatically important tropospheric species [2].

Remarkably, HO_x and NO_x catalyze O_3 production in the troposphere and O_3 destruction in the stratosphere. The catalytic HO_x and NO_x cycles for O_3 loss in the stratosphere:

$$OH + O_3 \rightarrow HO_2 + O_2 \qquad (R_{12})$$

$$HO_2 + O_3 \rightarrow OH + 2O_2 \qquad (R_{13})$$

$$NO + O_3 \rightarrow NO_2 + O_2 \qquad (R_{14})$$

$$NO_2 + O \rightarrow NO + O_2 \qquad (R_{15})$$

The key difference between the stratosphere and the troposphere is that O_3 and O concentrations are much lower in the troposphere. In the troposphere (R_{12}) is much slower than (R_4) and (R_{15}) is negligibly slow. Ozone loss by the HO_x catalyzed mechanism (R_{12})-(R_{13}) can still be important in remote regions of the atmosphere where NO concentrations are sufficiently low for (R_{13}) to compete with (R_{10}). Ozone loss by NO_x catalyzed mechanism (R_{14})-(R_{15}) is of no importance anywhere in the troposphere.

Chapter 2

Radiation transfer in the atmosphere

The production of radiation by bodies around us is usually from what are essentially blackbody surfaces, that absorb most of the thermal radiation incident on them. Planetary atmospheres are usually non-ideal blackbodies unless they contain high amounts of absorbing molecules. Radiation that is emitted by a surface or an atmospheric layer undergoes absorption and/or scattering, by the molecules that constitute the atmosphere as it is transferred through the atmosphere. Absorption and emission by a surface take place over the projected area of the surface in the direction of the radiation. Hence a planet absorbs solar radiation basically as a disc and emits thermal infra-red radiation as a sphere.

The emission from a blackbody is described by the laws of Planck, Wein and Stefan-Boltzmann. The first gives the spectral distributions of the photons, the second the location of the wave length of maximum emission and the third gives the dependence of the total amount of radiation emitted on temperature. As the temperature increases photons at progressively higher energies are emitted. In planetary atmosphere natural emission is thus restricted to infra-red whilst absorption can occur at all wavelengths from gamma rays to radio waves. For thermal infra-red radiation, we need to include absorption and emission in the equation of radiation transfer.

2.1 Radiation transfer theory

Radiative transfer is a branch of atmospheric physics. Like a nation composed of many different ethnic groups, radiative transfer has a rich, but sometimes confusing language that reflects its diverse heritage, which derives from quantum physics, astronomy, climatology, and electrical engineering. Solving radiative transfer problems requires consideration of the geometry and spectral distribution of radiation, both of which are straightforward in principle, but can be quite involved in real world situations. We now present some simple classical methods for solving the radiation transfer equation, as these methods form the basis for obtaining and understanding the radiation field within the planetary atmosphere.

2.1.1 Quantitative description of radiation

Let us assume that at the center of a virtual sphere of surface area A, there is an infinitesimally small body that is radiating isotropically in all directions.

Then, the fraction of the total emitted radiation that is transferred through an element of area dA on the sphere is dA/A. The emitted radiation can be regarded as consisting of small conical bundles of rays with the base of the cone having an element of area dA. The cone of radiation comprises a solid angle, dΩ, measured in steradian (sr) and given by

$$d\Omega = \sin\theta d\theta d\phi \tag{2.1.1}$$

where θ is the zenith angle and ϕ is the azimuth angle as defined in Fig. 2.1. In polar co-ordinates, the polar axis defines the zenith angle, whilst the equatorial axis defines the azimuth angle. The element of area dA is then given by

$$dA = (r\sin\theta d\phi)(rd\theta) \tag{2.1.2}$$

so that the total area of the sphere is

$$A = \int_0^{2\pi} d\phi \int_0^{\pi} r^2 \sin\theta d\theta = 4\pi r^2 \tag{2.1.3}$$

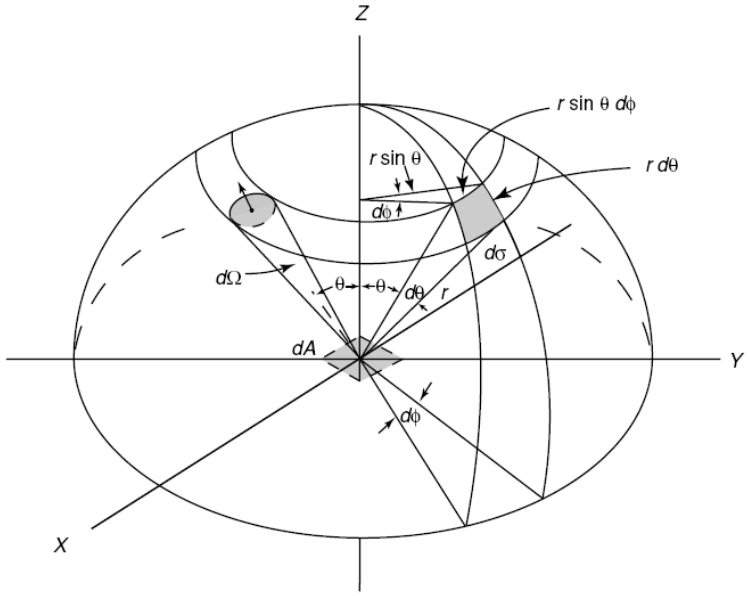

Figure 2.1: Radiation sphere with radius r, zenith angle θ, azimuth angle ϕ and element of solid angle dΩ.

Thus the fraction of the total radiation transferred through dA is given by

$$\frac{dA}{A} = \frac{1}{4\pi} \sin\theta d\theta d\phi = \frac{d\Omega}{4\pi} \tag{2.1.4}$$

Thus the surface of the radiation sphere can be divided into units of steradians with a total 4π (sr) for the whole sphere.

Radiance (or Intensity)

The monochromatic radiance, I_λ is defined as the energy (J) emitted by or transferred through an element of area δA (m^2) in a direction defined by the unit vector $\hat{n}$ within an element of solid angle dΩ (sr) per second (s) within a wavelength interval $\delta\lambda$ about λ [7]. If the wave length is measured in μm, then the units of radiance are $\frac{J}{m^2.s.sr.\mu m_\lambda}$, where we include the subscript λ to distinguish it from the dimensions of the emitting element of area.

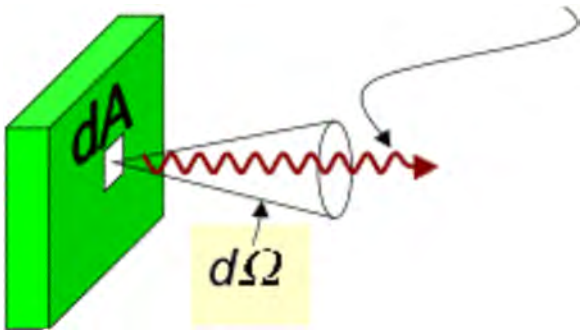

Figure 2.2: Radiance

If we denote the direction that is perpendicular to the infinitesimal element of area, taken to be planar, by the unit vector $\hat{k}$, then the projection of the element of area, in the direction of the radiation is $\delta \mathrm{A}(\hat{k}.\hat{n})$. Hence, the projected area is reduced as the radiation direction moves towards the horizon according to $\cos\theta$, where θ is the angle between the perpendicular direction and the direction of radiation. The total energy (J) that is emitted or transferred through the element of area in the direction $\hat{n}$ is then

$$\delta E = I_\lambda \delta A(\hat{k}.\hat{n})\delta\Omega\delta\lambda\delta t \tag{2.1.5}$$

in a time interval δt, within the spectral interval $\delta\lambda$ and within solid angle $\delta\Omega$.

From Eq. (2.1.5) the radiance is given by

$$I_\lambda = \frac{\delta E}{\delta A(\hat{k}.\hat{n})\delta\Omega\delta\lambda\delta t} \tag{2.1.6}$$

I_λ is called the monochromatic intensity or radiance. Monochromatic does not mean at a single wavelength λ, but a very narrow (infinitesimal) range of wavelength $\mathrm{d}\lambda$ centered at λ.

In general, the intensity is a function of coordinates ($\vec{r}$), direction ($\vec{\Omega}$), wavelength (or frequency) and time. Thus it depends on seven independent variables: three in space, two in angle, one in wavelength or frequency and one in time. Intensity, as a function of position and direction, gives a complete description of the electromagnetic wave. If it does not depend on the direction, the electromagnetic field is said to be *isotropic* and if intensity does not depend on position, the field is said to be *homogenous*.

Mean radiance and flux

The monochromatic mean radiance at a point in space $\vec{r}$ is defined as the radiance averaged over all directions according to

$$J_\lambda = \frac{1}{4\pi} \oint I_\lambda(\vec{r}, \hat{n}, t) d\Omega \tag{2.1.7}$$

The monochromatic *radiation flux* (or *irradiance*) is the radiance emitted by or transferred through an element of area, δA , located at a point $\vec{r}$ averaged over all directions, accounting for the projection of the surface area according to

$$f_\lambda(\vec{r}, t) = \oint I_\lambda(\vec{r}, \hat{n}, t) cos\theta d\Omega \tag{2.1.8}$$

and has units W $m^{-2}\mu\ m_\lambda^{-1}$. We can perform the above integral using Eqn. (2.1.1) to express $d\Omega$ in polar co-ordinates and setting $\mu = cos\theta$ we have

$$f_\lambda(\vec{r}, t) = \int_0^{2\pi} \int_{-1}^{1} I_\lambda(\vec{r}, \hat{n}, t) \mu d\mu d\phi \tag{2.1.9}$$

We note that if the radiance is isotropic then the integral vanishes for an element of area that is simply transferring radiation, as in the case within an atmosphere, and we have no net flux crossing the area. If we have a surface emitting isotropically to the upper hemisphere, then the integral reduces to

$$f_\lambda(\vec{r}, t) = \pi I_\lambda(\vec{r}, t) \tag{2.1.10}$$

where π has the units of sr. We may integrate the monochromatic flux over all wavelengths to obtain the total flux (or total irradiance) emitted by a surface

$$f(\vec{r}, t) = \pi \int_0^\infty I_\lambda(\vec{r}, t) d\lambda \tag{2.1.11}$$

Within an atmosphere the total flux incident on an element of volume is obtained by integrating over the surrounding sphere

$$f(\vec{r}, t) = 4\pi \int_0^\infty I_\lambda(\vec{r}, t) d\lambda \tag{2.1.12}$$

Luminosity

The monochromatic luminosity L_λ, of an element of surface area emitting or transferring radiation, is the monochromatic flux times the surface area according to

$$L_\lambda = \int I_\lambda(\vec{r}, \hat{n}, t)\delta A cos\theta d\Omega \tag{2.1.13}$$

For an element of area that emits or transfers radiation homogeneously

$$L_\lambda = \delta A \int I_\lambda(\vec{r}, \hat{n}, t) cos\theta d\Omega \tag{2.1.14}$$

and the total luminosity L, for isotropic radiation is

$$L(\vec{r}, t) = f(\vec{r}, t)\delta A \tag{2.1.15}$$

In the case of an emitting spherical surface of radius r, the total surface luminosity is

$$L(r, t) = 4\pi r^2 f(r, t) \tag{2.1.16}$$

2.1.2 Blackbody radiation

A blackbody is defined to be a perfect absorber and emitter of radiation. For a perfect blackbody solid surface or a totally opaque atmospheric layer, the radiance is isotropic and emission is homogeneous over the entire surface area, characterized by a homogeneous surface temperature T(K) [8]. For a planet or star with an absorbing-emitting-scattering atmosphere the radiation emitted to space may not be ideal blackbody radiation.

Planck's law

The radiance of an ideal blackbody is given by the Planck function, in terms of the wavelength λ as

$$B_\lambda(T) = \frac{2hc^2/\lambda^5}{e^{hc/\lambda\kappa T} - 1} \tag{2.1.17}$$

where c is the speed of light in vacuum, h is Planck's constant and κ is Boltzmann's constant.

In terms of frequency ($\nu = c/\lambda$) it takes the form

$$B_\nu(T) = \frac{2h\nu^3/c^2}{e^{h\nu/\kappa T} - 1} \tag{2.1.18}$$

with the following asymptotic behavior (Fig. 2.3),

•If $\lambda \to \infty$ (or $\bar{\nu} \to 0$) known as Rayleigh-Jeans distributions

$$\begin{aligned} B_\lambda(T) &= \frac{2\kappa_B T c}{\lambda^4} \\ B_{\bar{\nu}}(T) &= \frac{2\kappa_B T \bar{\nu}^2}{c^2} \end{aligned} \tag{2.1.19}$$

This long wave limit has a direct application to passive microwave remote sensing [9].

•If $\lambda \to 0$ (or $\bar{\nu} \to \infty$), then

$$\begin{aligned} B_\lambda(T) &= \frac{2hc^2}{\lambda^5} exp(-\frac{hc}{\lambda\kappa_B T}) \\ B_{\bar{\nu}}(T) &= \frac{2h\bar{\nu}^3}{c^2} exp(-\frac{h\bar{\nu}}{\kappa_B T}) \end{aligned} \tag{2.1.20}$$

Stefan-Boltzmann law

The total flux (W m^{-2}) emitted by a blackbody is given by Eq. (2.1.10) by replacing the radiance by the Planck function

$$f(T) = \pi \int_0^\infty B_\lambda(T) d\lambda \tag{2.1.21}$$

On setting $hc/\lambda\kappa T = y$ and integrating we have

$$f(T) = \frac{2\pi(\kappa T)^4}{h^3 c^2} \int_0^\infty \frac{y^3 dy}{e^y - 1} \tag{2.1.22}$$

where the integral is equal to $\pi^4/15$, which gives the simple result

$$f(T) = \sigma T^4 \tag{2.1.23}$$

known as the Stefan-Boltzmann Law, where σ is the Stefan-Boltzmann constant

$$\sigma = \frac{2\pi^5 \kappa^4}{15 h^3 c^2} \tag{2.1.24}$$

which is equal to 5.67×10^{-8} J m^{-2} K^{-4} s^{-1}. For a star or a planet we can assign an effective temperature ,T_{eff} , so that the total luminosity of the body is given by

$$L = 4\pi r^2 \sigma T_{eff}^4, \tag{2.1.25}$$

where r is its radius.

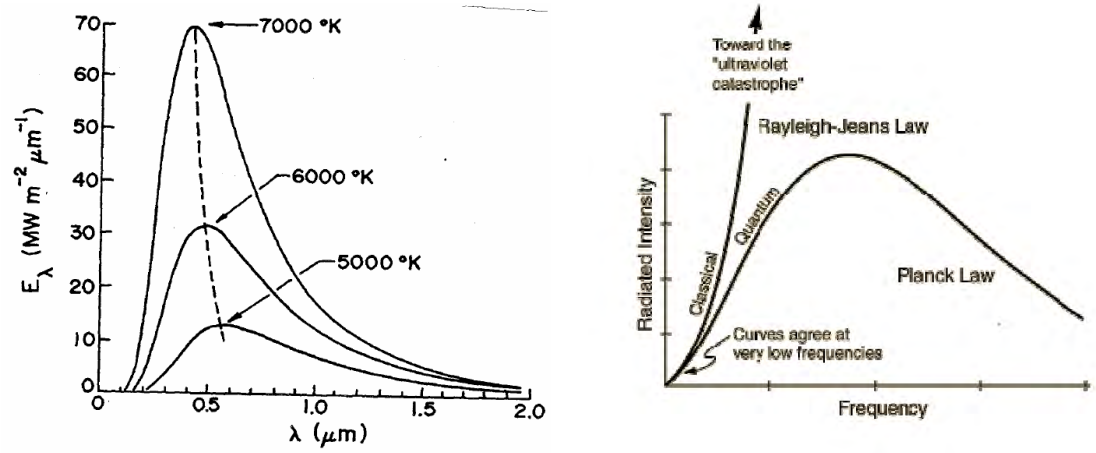

Figure 2.3: (Left)The variation of the Planck function with wavelength and temperature and (Right) Planck function and its asymptotic behavior.

Wien's displacement law

The variation of the Planck function with wavelength and temperature is shown in Fig. 2.3. The wavelength, λ_* in μm, corresponding to the maximum emission of radiation, is inversely proportional to the blackbody temperature according to Wien's law

$$\lambda_* = \frac{2898}{T(K)} \tag{2.1.26}$$

The wavelength λ_* is given by the condition that $\partial B_\lambda(T)/\partial\lambda$ =0. As the blackbody temperature increases, photons at higher energy become more numerous, since the photon energy $h\nu = hc/\lambda$.

The peak in Planck function moves to higher wavelengths as the temperature decreases, and we note from Fig. 2.3 that the Planck function at lower temperature is always below that at the higher temperature. We also note the rapid rise in the peak value of the Planck function with temperature.

Kirchhoff's law

The emissivity, ε_λ, of a medium is equal to the absorptivity, A_λ, of this medium under thermodynamic equilibrium:

$$\varepsilon_\lambda = A_\lambda \tag{2.1.27}$$

where ε_λ is defined as the ratio of the emitted intensity to the Planck function and A_λ is defined as the ratio of the absorbed intensity to the Planck function.

For blackbody, $\varepsilon_\lambda = A_\lambda = 1$, for a non-blackbody, $\varepsilon_\lambda = A_\lambda < 1$. For a gray body (i.e., no dependency on wavelength), $\varepsilon = A < 1$.

Kirchhoff's law applies to gases, liquids and solids if they are in thermodynamic equilibrium or local thermodynamic equilibrium. For atmospheric radiation transfer applications, one needs to distinguish between the emissivity of the surface (example various types of lands, ice etc.) and the emissivity of the atmospheric volume (consisting of gases, aerosols and/or clouds). Kirchhoff's law is applicable to gases provided that the frequency of molecular collisions is much larger than the frequency with which molecules absorb and emit radiation in the vicinity of the electromagnetic spectrum near the wavelength of interest.

When this condition is satisfied, the gas is said to be in local thermodynamic equilibrium (LTE). In the Earth's atmosphere, LTE prevails below altitudes of ∼60 km [8].

2.1.3 Radiative properties of Non-black materials

Unlike blackbodies, which absorb all incident radiation, non-blackbodies such as gaseous media (like the atmosphere) can also reflect and transmit radiation. However, their behavior can nonetheless be understood by applying the radiation laws derived for blackbodies.

For this purpose, it is is useful to define the monochromatic emissivity ε_λ, i.e., the ratio of the monochromatic intensity of the radiation emitted by the body to the corresponding blackbody radiation:

$$\varepsilon_\lambda = \frac{I_\lambda(emitted)}{B_\lambda(T)} \tag{2.1.28}$$

and the monochromatic absorptivity, reflectivity and transmissivity, the fractions of the incident monochromatic intensity that a body absorbs, reflects and transmits,i.e.,

$$\alpha_\lambda = \frac{I_\lambda(absorbed)}{I_\lambda(incident)}, R_\lambda = \frac{I_\lambda(reflected)}{I_\lambda(incident)} \; and \; T_\lambda = \frac{I_\lambda(transmitted)}{I_\lambda(incident)} \tag{2.1.29}$$

The atmosphere is not strictly in thermodynamic equilibrium, because its temperature and pressure are functions of position. Therefore, it is usually subdivided into small subsystems each of which is effectively isothermal and isobaric referred to as Local Thermodynamic Equilibrium (LTE).

2.2 Thermal infra-red transfer in the atmosphere

Absorption of terrestrial thermal infra-red radiation by molecules in the atmosphere depends on their concentration, type and whether they are heteronuclear (like CO_2, H_2O, CH_4) or homo nuclear (like N_2 and O_2), that is whether or not they have an electrical dipole that can interact with infra-red radiation. The atmosphere consists of mainly homo nuclear molecules and hence it is the trace molecules, which strongly absorb infra-red radiation emitted by the Earth's surface to space, that determine the strength of the greenhouse effect. The absorption of the heteronuclear nuclear molecules arises mainly through bound-bound transitions between quantized rotational levels that are affected by the vibration of the molecules.

We thus speak of vibrational-rotational lines that form molecular bands of spectral lines that absorb infra-red radiation, particularly between 5μm and 100μm, the spectral region where the Earth primarily emits blackbody radiation.

Absorption by rotational spectral lines through bound-bound transitions depends crucially on the broadening of the bound levels. There are primarily three line-broadening mechanisms; natural broadening that arises from the Heisenberg Uncertainty Principle, collisional (also known as pressure) broadening and Doppler broadening.

The most important line broadening in planetary atmospheres arises through collisions that depend on the atmospheric pressure. The broadening mechanisms allow photons that have energies greater or less than the difference in energy between the levels of the bound-bound transition to be absorbed. This enhances the ability of the molecule to absorb photons over a larger spectral interval with the result that the greenhouse effect becomes stronger as the pressure of the planetary atmosphere increases [7].

2.3 Line profiles of spectral lines

The rate of photon absorption by an atom (or molecule) resulting in the excitation of a bound electron from a lower to an upper energy level depends on the strength of the Einstein coefficient for absorption, a quantity intrinsic to the particular transition and that is usually measured in spectroscopy laboratories. The absorption also depends on the broadening of the bound energy levels, as this determines the available energy states that an electron can be excited to. Emission, on the other hand, not only depends on the available energy states of the upper level of transition but also on the population of atoms that have electrons in this excited state [10].

In thermodynamic equilibrium, the system is closed and all processes are in equilibrium; the population of the excited state is given by the Boltzmann distribution, which depends on atmospheric temperature.

The radiation field and the thermodynamic state of the atmosphere can be closely coupled through collisions that excite and de-excite atoms and so govern their population at each level. When collisions control the populations of the energy levels in a particular part

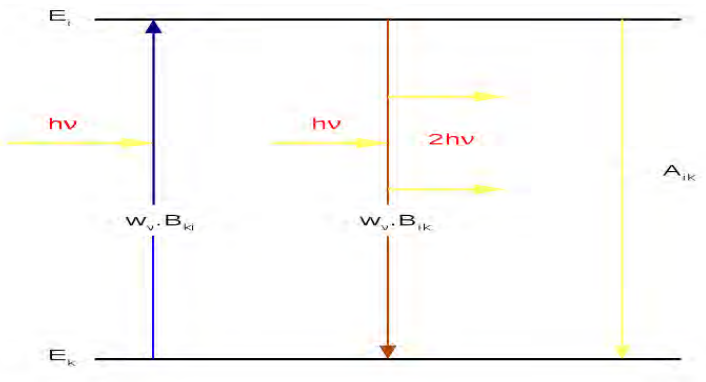

Figure 2.4: Absorption, induced emission and spontaneous emission of a photon of frequency ν between two discrete energy levels.

of an atmosphere, we have only LTE as the system is open to radiation loss. When collisions become infrequent then there is a de-coupling between the radiation field and the thermodynamic state of the atmosphere and emission is determined by the radiation field itself and we have no local thermodynamic equilibrium, or, non-LTE.

2.3.1 Mechanisms of molecular absorption

There are three main mechanisms by which molecules can absorb electromagnetic radiation. The first of these, requiring the largest amount of energy, involves the promotion of electrons to higher energy levels. These are termed ***electronic transitions***. Calculation of the energy levels for any but the simplest of molecules is an extremely difficult task, so we illustrate the idea with reference to hydrogen atom. In this case, the electronic energy levels are given by

$$E_n = -\frac{me^4}{32\pi^2\varepsilon_o^2\hbar^2}\frac{1}{n^2} \tag{2.3.1}$$

where m is the electron mass (strictly, the electron's reduced mass, which, in the hydrogen atom, i s 99.95% of the electron mass) and n is a quantum number that can take only positive integer values [10]. Substituting the values of the constants into the formula we find

$$E_n = -\frac{2.177 \times 10^{-18} J}{n^2} \tag{2.3.2}$$

although it is often more convenient to use the *electron volt* (eV) as the unit of energy, where $1eV \approx 1.602 \times 10^{-19}J$ so that the formula becomes

$$E_n = -\frac{13.59eV}{n^2} \tag{2.3.3}$$

In its ground state (the configuration with lowest energy), hydrogen has n=1. The smallest increase in energy therefore corresponds to the transition from n=1 to n=2, which requires an increase in energy of 10.2eV. This is typical of the energies required for electronic transitions, and from the equation $\Delta E = h\nu$ we see that the frequency of the electromagnetic radiation causing such transitions will therefore be of the order of 10^{15}Hz. The corresponding wavelength is thus a few tenths of micrometer, so that we expect to find the absorption lines due to electronic transitions in the ultraviolet and visible regions of the electromagnetic spectrum.

The second kind of molecular absorption that we consider is vibration. The molecular bond between atoms behaves more or less like a spring. To model this, we will consider a diatomic molecule consisting of two atoms with masses m_1 and m_2, connected by a spring with force constant k as shown in Fig. 2.5. Classical physics gives the natural angular frequency of the system as

$$\omega_o = \sqrt{\frac{k(m_1 + m_2)}{m_1 m_2}} \tag{2.3.4}$$

and quantum mechanics gives the energy levels as

$$E_\upsilon = (\upsilon + \frac{1}{2})\hbar\omega_o \tag{2.3.5}$$

where υ is a quantum number that can take any non-negative integer value. This quantum number can change only by ± 1, so in fact the only possible amount of energy that can be absorbed is $\Delta E = \hbar\omega_o$,

giving an absorption line at the resonant frequency $\nu = \omega_o/2\pi$. Because the force constant k is of the order of 1000 Nm^{-1}, the resonant frequency is typically between 10^{13} and 10^{14}Hz, corresponding to wavelengths generally in the thermal infrared region.

Figure 2.5: Classical model of molecular vibration and rotation

Within the approximation of a harmonic potential, any arbitrary vibration of a polyatomic molecule can be composed as a linear combination of normal vibrations with the total energy

$$E_{vib} = \sum_k \hbar\omega_k(\nu_k + \frac{d_k}{2}) \tag{2.3.6}$$

where d_k gives the degree of degeneracy of the k^{th} normal vibration. For a doubly degenerate vibrations d=2.

For higher vibrational energies the approximation of the harmonic potential is no longer valid and higher order terms in the potential in the expansion has to be taken into account. Now the total vibrational energy is no longer the sum of the energies of the normal vibrations, but coupling terms arise and instead of Eq. (2.3.6) we obtain

$$E_{vib}(\nu_1, \nu_2, ...\nu_{3N-6}) = \sum_k \hbar\omega_k(\nu_k + \frac{d_k}{2}) + \sum_{i,k} x_{ik}(\nu_i + \frac{d_k}{2})(\nu_k + \frac{d_k}{2}) + ... \tag{2.3.7}$$

This implies that the displacement of a nucleus during its vibration affects the restoring force for the other nuclei, and therefore their vibrational energy.

The last molecular absorption we shall discuss is rotation. We will consider a simple diatomic molecule consisting of two atoms with masses m_1 and m_2, separated by a fixed distance s. Classically this system can rotate about the center of mass of the two atoms. The moment of inertia of the system is given by

$$I = \frac{m_1 m_2}{m_1 + m_2} s^2 \tag{2.3.8}$$

and, according to quantum mechanics, the energy of such a state is given by

$$E_J = \frac{J(J+1)\hbar^2}{2I} \tag{2.3.9}$$

where J is a quantum number that can take any non negative integer value. When electromagnetic radiation is absorbed, J must increase by 1. Calculating ΔE from Eq. (2.3.7), for the transition from quantum number J to J+1, and substituting it into $\Delta E = h\nu$, we find that the frequency of a rotation absorption line is given by

$$\nu = \frac{(J+1)h}{4\pi^2 I} \tag{2.3.10}$$

We can consider the CO molecule as an example. It has $m_1 = 2.66 \times 10^{-26}$kg and $m_2 = 1.99 \times 10^{-26}$kg and $s = 1.13 \times 10^{-10}$m giving it a moment of inertia $I = 1.45 \times 10^{-46}$ kgm^2. We thus calculate that the $J = 0 \rightarrow 1$ transition will occur at a frequency of 116 GHz, which is the microwave region. In general, we expect to find the rotational absorption lines in the microwave or far-infrared regions of the electromagnetic spectrum with frequencies typically between 10^{10} and 10^{12}Hz [11].

Although we have now outlined the most important mechanisms governing molecular absorption lines, there are further complications to be considered. Combinations of mechanisms can operate at the same time. For example, the energy level of a molecule can be described by both a rotational quantum number J and a vibrational quantum number υ, and both of these may change in a transition. This gives rise to a more complicated vibrational-rotational spectrum in which a vibrational absorption line has fine structure superimposed on it as a result of different rotational transitions. Not all possible transitions can in fact be excited by electromagnetic radiation. For example the hydrogen molecule H_2 has a symmetric distribution of electric charge, which means that, classically speaking, an electric field can not exert force on it. We should therefore not expect molecular hydrogen to absorb electromagnetic radiation by vibrational or rotational transitions.

2.3.2 Spectral-line broadening

The absorption or emission of radiation on an atomic or molecular transition doesn't result in a strictly monochromatic spectral line, but rather in a frequency distribution

around the central frequency ν_o. This gives a line profile $\mathcal{L}(\nu - \nu_o)$ with a fullwidth at half-maximum, $\delta\nu$, which not only depends on the spectral resolution of the measuring instrument but also on basic physical properties, such as the life times of the atomic states involved in the transition, the velocity of distribution of the moving atoms and the pressure of the gaseous sample.

The line width in frequency units is defined as the interval $\delta\nu = \nu_2 - \nu_1$, between frequencies, $\nu_1 < \nu_o$ and $\nu_2 > \nu_o$ on both sides of the central frequency ν_o, where the intensity $I(\nu_1) = I(\nu_2) = \frac{1}{2}I(\nu_o)$ of the spectral line profile has dropped to half of its maximum value at the line center (full width at half maximum, FWHM). Often the line width is given in units of the circular frequency, $\omega = 2\pi\nu \Rightarrow \delta\omega = 2\pi\delta\nu$ or in units of the wavelength λ.

Since $\lambda = \frac{c}{\nu}$ we have

$$\delta\lambda = -(\frac{c}{\nu^2})\delta\nu = -(\frac{\lambda}{\nu})\delta\nu \tag{2.3.11}$$

The relative half widths are equal in all these notations, because from Eq. (2.3.11), it follows that

$$|\frac{\delta\lambda}{\lambda}| = |\frac{\delta\nu}{\nu}| = |\frac{\delta\omega}{\omega}| \tag{2.3.12}$$

There are several reasons for finite line widths of spectral lines. Some of these are:

•The energy levels of the atoms have an energy uncertainty $\delta E = \frac{h}{\tau}$ related to their finite life time τ. The frequency width of a spectral line corresponding to a transition between levels E_i and E_k is $\delta\nu_{ik} = \frac{(\delta E_i + \delta E_k)}{h}$ (natural line width).

•Atoms in a gas move with a mean velocity υ, depending on their mass and temperature of the gas. This leads to a Doppler shift of their emitted or absorbed radiation.

The statistical distribution of the velocities of many atoms in a gas results in a statistically distributed Doppler shifts, which give rise to a Gaussian line profile (Doppler broadening).

•Every atom in a gas interacts with other neighboring atoms. This results in a shift of the atomic energy levels. Since the interaction decreases with increasing distance between the interacting atoms, the level shifts and with it the line shifts increase with the density

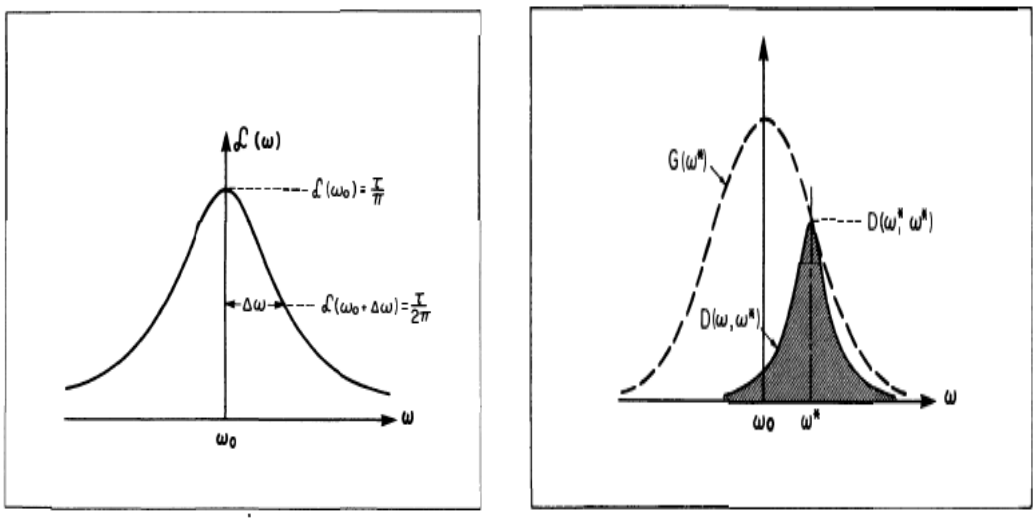

Figure 2.6: Lorentz dispersion line profile function (left) and Convolution of Gaussian and dispersive profiles (right) [44].

or pressure of the gas, resulting in a pressure broadening and shift of the spectral lines. According to the internal energy structure of atoms (or molecules), we might suspect that transitions between two quantum states would result in spectrally narrow emission or absorption lines. This is indeed the case in the limit of low temperature and density. However, even under these circumstances, there is a finite spread of frequencies associated with the the finite lifetime of the excited states. In general there are many causes of line-broadening, some real and some apparent (instrumental).

The most important forms of line broadening from our point of view, may be classified under the following headings:

Natural broadening, due to the finite life time of the energy states involved in the transition.

Doppler broadening, due to the Doppler shift associated with the thermal motion of the radiating (absorbing) species.

Collision broadening, due to elastic or inelastic encounters between the radiating (absorbing) species and neighboring atoms (molecules).

Instrumental broadening, which arises when the spectral line is observed through an instrument with inadequate spectral resolution.

In addition to these, applied **E** or **H** fields can lead to broadening; in particular if the radiating or absorbing species is immersed in a plasma, the electric micro fields of the electrons and ions can lead to *Stark broadening*.

(a).Natural and Collision Broadening:

Atomic transitions between discrete energy levels, E_k and E_i result in the absorption and emission of photons of energy exactly equal to the difference in energy between the two levels as shown in Fig. 2.4, where

$$E_i - E_k = h\nu_{ki} \tag{2.3.13}$$

According to Heisenberg uncertainty principle, an atom or molecule has a definite life time, Δt, at an energy level with uncertainty, ΔE, in its energy, given by

$$\Delta E \sim \frac{\hbar}{\Delta t} \tag{2.3.14}$$

where $\hbar = \frac{h}{2\pi}$, and h is the Planck constant. The life time of an atom in its ground state is large with the result that this natural energy level broadening is negligible. The first excited state has a smaller life time with the result that the energy level broadening is significant and measurable [10].

If we represent a molecule or atom by a simple harmonic oscillator with a resonant frequency ω_o, and imagine the oscillator to be given a sudden impulse, then the system would radiate an electromagnetic energy at an angular frequency ω_o, for a length of time determined either by the radiation damping constant or by collisional decay. We shall show that this limited period of emission results in a finite band width for the radiation field. In order to accomplish this we shall adopt a classical-quantum hybrid model. This *Lorentz approach* provides a considerable physical insight into both natural and collision broadening with a minimum of mathematical complexity.

We shall assume that the radiated component of the electric field from an excited molecule

or atom is

$$E(t) = \begin{cases} E_o e^{-i\omega_o t}, & 0 < t < T; \\ 0, & t \leq 0 \ or \ t \geq T. \end{cases} \tag{2.3.15}$$

where the truncation period T corresponds to the lifetime of the excited state. The corresponding Fourier component of the radiated field is

$$\begin{aligned} E(\omega, T) &= \frac{1}{2\pi} \int_{-\infty}^{+\infty} E(t) e^{i\omega t} dt = \frac{E_o}{2\pi} \int_0^T e^{i(\omega - \omega_o)t} dt \\ &= \frac{E_o}{\pi} [\frac{sin((\omega - \omega_o)T/2)}{(\omega - \omega_o)}] e^{i(\omega - \omega_o)T/2} \end{aligned} \tag{2.3.16}$$

If τ represents the mean lifetime for a statistical ensemble of such radiating systems, then we can write

$$\frac{dN(t)}{dt} = -\frac{N(t)}{\tau} \quad or \quad N(t) = N(0) e^{-t/\tau} \tag{2.3.17}$$

where N(t) is the number density of the excited species at time t. Under these circumstances the probability of any given excited state undergoing a decay in the time interval (T,T+dT) is given by

$$P(T)dT = -\frac{dN(T)}{N(0)} = e^{-T/\tau} \frac{dT}{\tau} \tag{2.3.18}$$

The observed radiation is a composite of the emission from all the excited species with this respective range of lifetimes. Under these circumstances the spectral irradiance is

$$I(\omega) = B \int_0^\infty |E(\omega, T)|^2 P(T) dT \tag{2.3.19}$$

where B is the appropriate proportionality constant. Substitution of Eqs. (2.3.16) and (2.3.18) into Eq. (2.3.19) yields

$$I(\omega) = \frac{aA}{b^2} \int_0^\infty sin^2(\frac{bT}{2}) e^{-aT} dT \tag{2.3.20}$$

where we have introduced a$\equiv \frac{1}{\tau}, b \equiv \omega - \omega_o$, and the new constant of proportionality A. The integral in Eq. (2.3.20) is evaluated in any mathematical handbook and leads to the relation

$$I(\omega) = \frac{A}{(\omega_o - \omega)^2 + (1/\tau)^2} \tag{2.3.21}$$

The constant of proportionality can be eliminated in terms of the total irradiance I_o by spectrally integrating Eq. (2.3.21) over all frequencies:

$$I_o \equiv \int_{-\infty}^{\infty} I(\omega)d\omega = \int_{-\infty}^{\infty} \frac{Ad\omega}{(\omega_o - \omega)^2 + (1/\tau)^2} = \frac{\pi A}{a} \tag{2.3.22}$$

Consequently we may write

$$I(\omega) = I_o \mathcal{L}(\omega) \tag{2.3.23}$$

where the line profile function

$$\mathcal{L}(\omega) = \frac{1}{\pi} . \frac{(1/\tau)}{(\omega_o - \omega)^2 + (1/\tau)^2} \tag{2.3.24}$$

is Lorentzian. We see that the spectral distribution of an emission line that is lifetime-limited is the same as that of a classical absorber provided $1/\tau = \gamma/2$. The distinctive Lorentzian shape is illustrated in Fig. 2.6, and we can see that the angular frequency half width at half maximum (HWHM), $\Delta\omega$, is given by

$$\mathcal{L}(\omega_o + \Delta\omega) = \frac{1}{2}\mathcal{L}(\omega_o), or\ \Delta\omega = \frac{1}{\tau} \tag{2.3.25}$$

In the case of natural broadening, τ_N is the radiative lifetime and typically has a value of about 10^{-8}s for atomic resonance lines. This leads to an angular frequency HWHM $\Delta\omega_N = 10^8$ rad/s or $\Delta\nu_N = \frac{10^8}{2\pi}$=16.7 MHz.

Furthermore, since $\lambda\nu$=c, it follows that the natural line width is

$$\Delta\lambda_N = \frac{\lambda^2}{c}\Delta\nu_N \tag{2.3.26}$$

When collisions are effective in reducing the life time of excited state or perturbing the energy separation between two quantum states of the emitting (absorbing) species, then additional broadening occurs. If the collisions are between like atoms or molecules, we refer to Holtsmark broadening; if between unlike species, we refer to Van der Waals broadening. If the lifetime of the excited state is reduced by collisions, the collision line profile takes the form

$$\mathcal{L}^c(\omega) = \frac{1}{\pi}\frac{1/\tau_c}{(\omega_0 - \omega)^2 + (1/\tau_c)^2} \tag{2.3.27}$$

where in this instance the collision lifetime τ_c is given by the expression

$$\frac{1}{\tau_c} = N\langle\sigma u\rangle_c \tag{2.3.28}$$

Here $\langle\sigma u\rangle_c$ represents the effective collision frequency per perturber and N the number density of perturbers. If the appropriate collision cross-section is only a weak function of velocity, then we can write

$$\langle\sigma u\rangle_c \approx \sigma_c[8\kappa T/\pi\mu]^{1/2} \tag{2.3.29}$$

where μ is the reduced mass of the collision partners.

(b).Doppler Broadening:

If the radiating atom or molecule has a velocity component u_x along the line of sight, then the observed frequency ω is Doppler shifted relative to the rest frame frequency ω_o:

$$\omega = \omega_o(1 \pm \frac{u_x}{c}) \tag{2.3.30}$$

where c is the velocity of light. The positive sign applies if the emitter is moving towards the observer (Fig. 2.7) and the negative sign is required when the emitter is receding from the observer.

If the emitting species has a Maxwellian velocity distribution, then the probability that a radiating atom or molecule will have an x- component of velocity in the interval $(u_x, u_x + du_x)$ is given by

$$f(u_x)du_x = [m/2\pi\kappa T]^{1/2}e^{-mu_x^2/2\kappa T}du_x \tag{2.3.31}$$

where m is the mass of the emitter and T is its translational temperature. Combining Eq. (2.3.30) with Eq. (2.3.31), we see that the probability that a photon with rest-angular frequency ω_o, will be observed with an angular frequency in the interval$(\omega, \omega + d\omega)$, is

$$\mathcal{L}_G(\omega) = \frac{1}{\beta\pi^{1/2}}e^{-(\omega-\omega_o)^2}/\beta^2 \tag{2.3.32}$$

where we have introduced

$$\beta \equiv [2\kappa T\omega_o^2/mc^2]^{1/2} \tag{2.3.33}$$

We see that the thermal motion (assumed Maxwellian) of the radiating species leads to a Gaussian line profile function (Eq. (2.3.32); see Fig. 2.7). As we might expect, $\int \mathcal{L}(\omega)d\omega$=1. The angular-frequency HWHM, $\Delta\omega$ for the Doppler-broadened spectral line is given by the relation

$$\mathcal{L}_G(\omega_o + \Delta\omega) = \frac{1}{2}\mathcal{L}_G(\omega_o) \; or \; \Delta\omega = \beta[ln2]^{1/2} \tag{2.3.34}$$

A comparison of the Lorentz and Gaussian line profile Functions reveals that the spectral distribution associated with natural or collision broadening is quite different from that arising from thermal motion. The wing content of the Lorentz profile is much greater than that of Gaussian profile if they have comparable spectral widths. Reference to Eq. (2.3.33) and Eq. (2.3.34) also indicates that the width of a Doppler broadened line is proportional to the square root of the temperature of the radiating species. It should be noted that although we have evaluated the emission line profile associated with the thermal motion of the atoms or molecules, similar reasoning for the absorption of radiation would lead to identical Gaussian line profile function.

(c).Combined Natural, Collision and Doppler Profiles:

The rest-frame line profile of a radiating or absorbing species is most often Lorentzian (natural or collisional); however, invariably there is also relative motion between the emitter and the observer or between the source and the absorber. Where this motion arises from the thermal energy of the atoms or molecules, we have seen that a Gaussian line profile results. Clearly, in most situations of interest, actual line profile will involve a convolution of these two types of broadening mechanisms. Although we shall consider emission, the analysis could just as easily be applied to the case of absorption, yielding the same profile function.

Thus the actual profile can be written in the form of the convolution

$$\mathcal{L}(\omega) = \int_{-\infty}^{\infty} G(\omega^*)D(\omega, \omega^*)d\omega^* \tag{2.3.35}$$

where $D(\omega, \omega^*)$ represents the Lorentzian (dispersive) probability of emission at ω for an emitter having a line center frequency ω^*. $G(\omega^*)d\omega^*$ represents the Gaussian probability of an emitter having a line center frequency in the interval $(\omega^*, \omega^* + d\omega^*)$ due to its thermal motion. Thus in this instance we recognize that when there is relative motion between an emitter and an observer, the entire homogeneous line profile is Doppler shifted-which is the same as saying that the rest-frame line center frequency ω_o is Doppler shifted to ω^*:

$$\omega^* = \omega_o(1 \pm \frac{u_x}{c}) \tag{2.3.36}$$

As before, $G(\omega^*)$ is derived from the appropriate Maxwellian velocity distribution and describes the probability of any emitter having a given velocity u_x relative to the observer. This is illustrated in Fig. 2.6, where $G(\omega^*)$ is seen to be the envelope of the $D(\omega, \omega^*)$ values.

From our previous discussion [Eqs. (2.3.24) and (2.3.32)] it is apparent that we can write

$$G(\omega^*) = \frac{1}{\beta\pi^{1/2}} e^{-(\omega_o - \omega^*)^2}/\beta^2 \tag{2.3.37}$$

and

$$D(\omega, \omega^*) = \frac{1}{\pi} \frac{1/\tau}{(\omega^* - \omega)^2 + (1/\tau)^2} \tag{2.3.38}$$

where β represents the Gaussian HWHM divided by $[ln2]^{1/2}$ and was defined by Eq. (2.3.33), and $1/\tau$ represents the Lorentzian HWHM. Consequently,

$$\mathcal{L}(\omega) = \frac{1}{\beta\tau\pi\sqrt{\pi}} \int_{-\infty}^{\infty} \frac{e^{-(\omega_o - \omega^*)^2}/\beta^2}{(\omega^* - \omega)^2 + (1/\tau)^2} \tag{2.3.39}$$

If we introduce

$$y \equiv \frac{\omega^* - \omega_o}{\beta}, u \equiv \frac{\omega - \omega_o}{\beta}, a \equiv \frac{1}{\beta\tau} \tag{2.3.40}$$

then Eq. (2.3.39) becomes

$$\mathcal{L}(u) = \frac{a}{\beta\pi\sqrt{\pi}} \int_{-\infty}^{\infty} \frac{e^{-y^2} dy}{(u - y)^2 + a^2} \tag{2.3.41}$$

the *Voigt line function*. In general Eq. (2.3.41) has to be evaluated numerically, although at core frequencies (u≈0), $\mathcal{L}(u)$ is close to being Gaussian, while in the wings of the profile

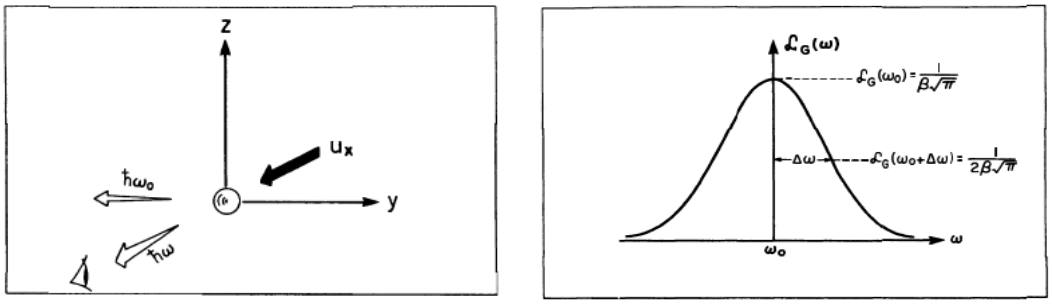

Figure 2.7: Radiation emited in the direction of motion is Doppler shifted so that the observed frequency is $\omega = \omega_o(1+u_x/c)$ (left) and Doppler-broadened Gaussian line profile function (right).

(u$\gg$1), $\mathcal{L}(u)$ is Lorentzian.

If a spectral profile is being resolved by some kind of spectrometer, then some allowance may have to be made for the finite resolving power of the instrument. Indeed, it is often the case that the width of the instrumental profile is comparable to that of the spectral line under examination. Sometimes it is possible to assume that the instrumental profile is approximately described by a Lorentzian or Gaussian distribution. Under either of these circumstances, the following theorems can be very useful for evaluating the instrumental broadening.

1.The convolution of two Lorentzian distributions whose widths are characterized by γ_1 and γ_2, respectively, is also a Lorentzian with a total width $\gamma = \gamma_1 + \gamma_2$.

2.The convolution of two Gaussian profiles characterized by widths β_1 and β_2 is also Gaussian with a total width $\beta = (\beta_1^2 + \beta_2^2)^{1/2}$ [44].

2.4 The radiative transfer equation

The equation of radiation transfer describes the modification of the radiation field as it traverses an atmosphere. It has terms related to absorption, emission and scattering of photons by the atmospheric molecules, but can include surface effects. Planetary atmospheres can, as a first approximation, be considered as plane-parallel or simple layers. It is better to simplify and solve the transfer equation to deal with specific problems rather than attempt to formulate a very general solution in three dimensions. We thus focus on the classical solutions for specific cases that were developed by the early workers in the field [12]. These solutions serve as a basis for the development of more complicated methods and for an initial understanding of the key radiation processes in planetary atmospheres.

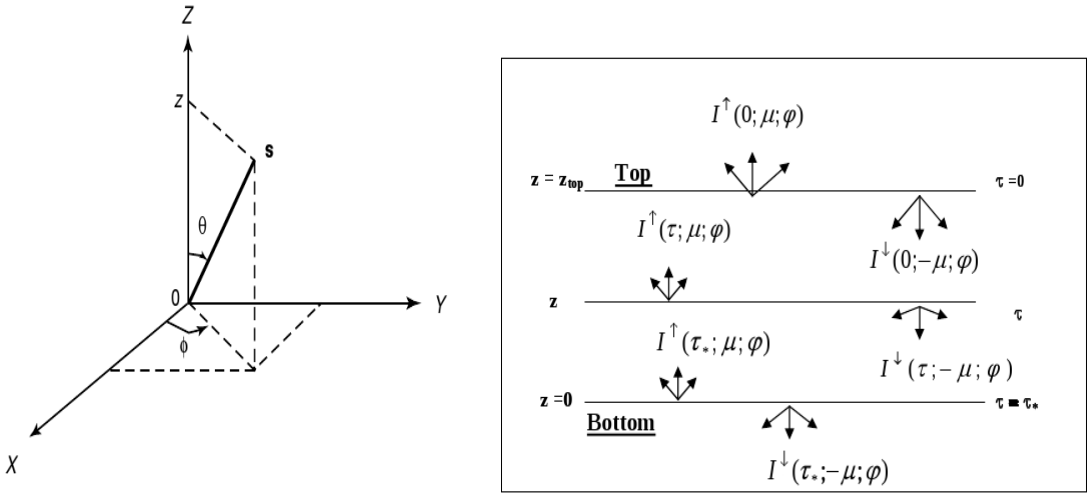

Figure 2.8: (Left) Geometry for plane-parallel atmospheres where θ and ϕ denote the zenith and azimuthal angles, respectively, and **s** represents the position vector. (Right) Schematic representation of the plane-parallel atmosphere.

For the sake of simplicity in deriving the equation of IR radiative transfer for atmospheric conditions, we are making some assumptions.

•The atmosphere is in LTE. This is true up to the height of 60-70 km. Above this level correction must be applied to the Planck function to obtain the correct source function [12].

•The atmosphere is plane parallel and horizontally homogeneous and the refraction is negligible. To consider a spherically stratified refractive geometry, correction must be applied to the relative optical path.

•Light scattering in the IR spectral region is also negligible. (This is true for the gas components but we do not have sufficient information about the aerosol particles).

Consider an absorbing and emitting medium. A pencil of radiation traversing this medium will be weakened by the interaction with matter through absorption. At the same time, this radiation may be strengthened by thermal emission from the medium. This pencil of radiation is usually represented by its intensity (or radiance), I_ν , in the field of radiative transfer. The general equation for radiative transfer in an absorbing and emitting medium can be written in terms of the differential change in the intensity, according to *Chandrasekhar* [13] in the form

$$-\frac{1}{k_\nu \rho_a}\frac{dI_\nu}{ds} = I_\nu - J_\nu. \tag{2.4.1}$$

where k_ν denotes the absorption coefficient, ρ_a is the density of absorbing gases, s is the slant path, I_ν is the monochromatic radiance and J_ν is the source function. For applications concerning the radiation budget of the planet, it suffices to consider the intensity as being independent of time. Moreover, it is commonly assumed that, in localized portions, the atmosphere is in thermodynamic equilibrium, as well as being plane-parallel.

The first assumption allows us to use the Planck intensity for the source function by virtue of Kirchhoffs law. The plane-parallel assumption implies that variations in the intensity and atmospheric parameters (temperature and gaseous profiles) are permitted only in the vertical direction (e.g., height or pressure). Under this assumption, absorption and emission processes would be symmetrical with respect to the azimuthal angle. It follows that the intensity is a function of the vertical position and zenith angle.

Under these conditions, the basic equation that governs thermal IR radiation in the height coordinate may be written in the form

$$-\mu \frac{dI_\nu(z,\mu)}{k_\nu \rho_a dz} = I_\nu(z,\mu) - B_\nu(z), \tag{2.4.2}$$

where the Planck intensity $B_\nu(z) = B_\nu(T(z))$ and $\mu = cos(\theta)$ and θ is the zenith angle. Because of the height dependence of both the gaseous density and absorption coefficient, it is convenient to define the normal optical depth, or simply *optical depth*, in the form

$$\tau = \int_z^{z_\infty} k_\nu(z')\rho_a(z')dz' = \int_0^p k_\nu(p')q(p')\frac{dp'}{g} \tag{2.4.3}$$

where z_∞ denotes the height at the top of the atmosphere (TOA), $q = \rho_a/\rho$, the gaseous mixing ratio, and ρ is the air density. The differential optical depth can be readily obtained from Eq. (2.4.3) with the form $d\tau = k_\nu(z)\rho_a(z)dz = k_\nu(p)q(p)dp/g$. In terms of the τ coordinate Eq. (2.4.2) may be rewritten as follows

$$\mu \frac{dI_\nu(\tau,\mu)}{d\tau} = I_\nu(\tau,\mu) - B_\nu(\tau) \tag{2.4.4}$$

For the upward intensity, the zenith angle $0 \leq \theta \leq \pi/2$; that is, $0 \leq \mu \leq 1$. However, for the downward intensity, $\pi/2 \leq \theta \leq \pi$. In this case, we may set $\mu = -\mu$ for convenience in radiative transfer analyses.

Eq. (2.4.4) represents a first-order differential equation. In order to solve both upward and downward components for an atmosphere with a total optical depth of τ , two boundary conditions are required. Under the plane-parallel assumption, these conditions are isotropic emissions from both the surface and TOA. In general, the Earth's surface may be considered as a blackbody in the infrared, so that $I_\nu(\tau,\mu) = B_\nu(T(\tau_*))$. In addition, we may allow for a possible source of downward emission at TOA and write $I_\nu(0,-\mu) = B_\nu$ (TOA). Normally, however, $B_\nu(TOA) \approx 0$ [14]. Subject to the preceding boundary conditions, the formal solutions for upward and downward intensities are given by

$$I_\nu^{\uparrow}(\tau,\mu) = B_\nu(\tau_*)e^{-(\tau_*-\tau)/\mu} + \int_\tau^{\tau_*} B_\nu(\tau')e^{-(\tau'-\tau)/\mu}\frac{d\tau'}{\mu}, \tag{2.4.5}$$

$$I_\nu^{\downarrow}(\tau,-\mu)=\int_0^{\tau}B_\nu(\tau')e^{-(\tau-\tau')/\mu}\frac{d\tau'}{\mu} \tag{2.4.6}$$

We shall now define the monochromatic transmittance (also referred to as the transmission function) so that the exponential attenuation may be expressed by

$$T_\nu(\tau/\mu)=e^{-\tau/\mu} \tag{2.4.7}$$

The differential form is

$$\frac{dT_\nu(\tau/\mu)}{d\tau}=-\frac{1}{\mu}e^{-\tau/\mu} \tag{2.4.8}$$

The formal solutions for the intensities can then be expressed by

$$I_\nu^{\uparrow}(\tau,\mu)=B_\nu(\tau_*)T_\nu[(\tau_*-\tau)/\mu]+\int_\tau^{\tau_*}B_\nu(\tau')\frac{d}{d\tau'}T_\nu[(\tau'-\tau)/\mu]d\tau' \tag{2.4.9}$$

$$I_\nu^{\downarrow}(\tau,-\mu)=\int_0^{\tau}B_\nu(\tau')\frac{d}{d\tau'}T_\nu[(\tau-\tau')/\mu]d\tau' \tag{2.4.10}$$

Eq. (2.4.9) can be applied in remote sounding using emitted infra-red radiation [9].

Chapter 3

Atmospheric trends and impacts of methane

Methane (CH_4) is the most abundant organic trace gas in the atmosphere. Concentrations of CH_4 have more than doubled since pre-industrial times. Currently CH_4 has a globally averaged mixing ratio of about 1880 ppbv [15]. The effects of CH_4 on climate and atmospheric chemistry raise concern over its high growth rate. Following water vapor and carbon dioxide (CO_2), methane is the most abundant greenhouse gas in the troposphere. On a per molecule basis, additional methane is actually much more effective as a greenhouse gas than additional CO_2. Methane is also the most abundant reactive trace gas in the troposphere and its reactivity is important to both tropospheric and stratospheric chemistry. The oxidation of CH_4 by hydroxyl (OH) in the troposphere leads to the formation of formaldehyde (CH_2O), carbon monoxide (CO), and, with sufficient nitrogen oxides (NO_x), to ozone (O_3). Along with CO, methane helps control the amount of OH in the troposphere. Methane also affects the concentrations of water vapor and ozone in the stratosphere and plays a key role in the conversion of reactive chlorine to less reactive HCl in the stratosphere.

The observed concentrations of atmospheric methane result from two factors - processes that release methane into the atmosphere and processes that remove it. When these processes are out of balance methane concentrations rise or fall or undergo cyclical variations. On the time scale of a year, methane concentrations undergo seasonal variations that are

large at high latitudes and smaller at tropical and equatorial latitudes. The entire global burden of methane undergoes seasonal variations. On longer time scales during recent years, the trends of methane are characterized by persistently increasing concentrations.

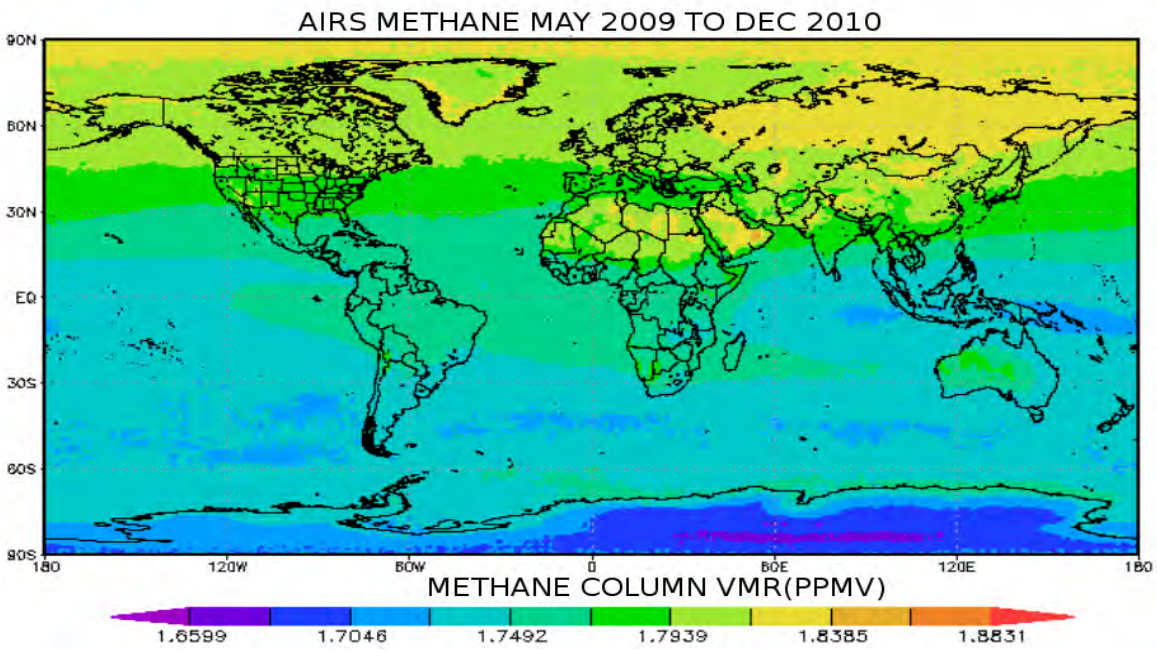

Figure 3.1: Global burden CH_4 mixing ratio.(http://disc.sci.gsfc.nasa.gov/giovanni).

3.1 Methane Sources

Methane differs from carbon dioxide in that it is released in to the atmosphere by a number of sources, both natural and anthropogenic. Anthropogenic emissions arise from biogenic sources related to agriculture and waste disposal, including enteric fermentation, animal and human wastes, rice paddies, biomass burning and land fills. Methane is also emitted by the extraction of fossil fuels such as natural gas, coal mining and petroleum. Methane is emitted naturally by wetlands, termites, other wild ruminants, oceans and hydrates. Based on recent estimates current human-related biogenic and fossil fuel-related sources for methane are approximately 275 and 100 Tg CH_4 yr^{-1}, while the total natural sources are around 160 Tg CH_4 yr^{-1} [16].

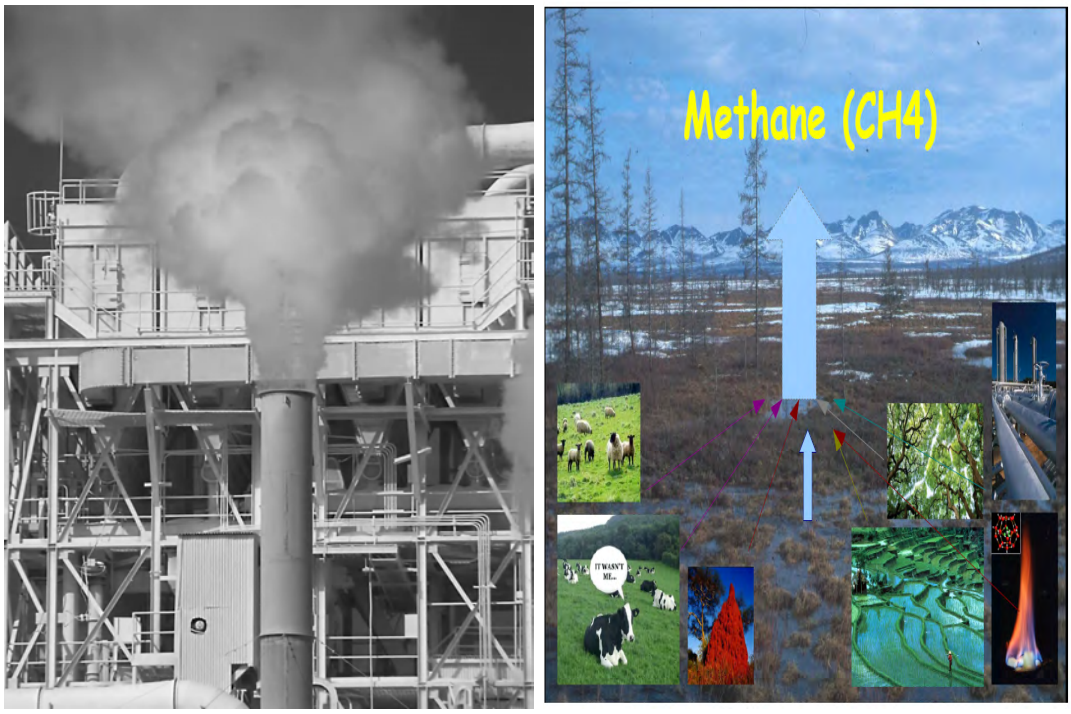

Figure 3.2: Global methane emission into the atmosphere;Human activities are to blame for around 60% global methane emission in to the atmosphere each year. **source**:[17].

Due to the variety of methane sources, emissions are affected by the numerous factors, including energy use, human population distributions, agricultural practices and climate. Here, we briefly describe the main factors influencing the magnitude of emissions from each major source.

3.1.1 Biogenic sources

Methane emissions from biogenic sources result from anaerobic decomposition of organic material by methanotrophic bacteria-in the flooded soils, in land fills, or other waste disposal sites and in the digestive tracks of domestic ruminants such as cattle or sheep wild ruminants such as buffalo or termites and even humans.

It has been determined that methane production is temperature-dependent with maximum production peaking over 30^{o}C [15]. This temperature dependence is an important

factor with implications of further changes for emissions from flooded soils, such as wet lands or rise paddies. It represents an important positive feedback on climate change as the atmosphere warms, emissions from these sources will increase, raising the concentration of CH_4 in the atmosphere and enhancing the warming.

In rise fields, emissions are also dependent on the conditions and agricultural practices employed during cultivation, such as climate, soil characteristics and cultivation practices including water management, fertilizers, other additives and different variety of rise plants [18]. Emissions are also determined by the number of crops per year and the total area under cultivation, which is a function of the demand for rise and the amount of rise produced per hectare known as 'yield'.

Practices such as occasional draining of the fields, the addition of oxidants or other mineral fertilizers and selection of low CH_4 cultivars have been found to reduce emissions by approximately 40-55% , 20-70% and up to 60% respectively [15]. Alternatively the addition of organic fertilizers has the potential to increase emissions by over 50% relative to non organic fertilizers [15].

Direct emissions from ruminants including cattle, sheep, buffalo, goats and other domestic animals are affected by diet [19]. Methane emissions are a by-product of incomplete digestion. In general higher quality diets will allow animals to digest their food more completely improving protein uptake, while reducing CH_4 emissions. This is particularly true of ruminant diets in developing countries, where improving the relatively poor food quality could lead to emissions reductions per kg of milk produced of up to 75% [20]. The addition of production enhancing supplements to cattle diet has also been suggested as a means to improve digestion and reduce emissions by up to 40% [19]. Animal manure is an additional source of methane. If animal waste is allowed to remain in the field, the manure dries quickly and methane emissions are minimal. However, if the waste is pooled and stored, methane emissions can rise by a factor of 10 [21].

Methane is also emitted by the decay of biogenic waste in the anaerobic environments provided by land fills and waste water pools. Emissions from land fills are affected by numerous environmental and technical variables including temperature, soil moisture and CH_4 concentration within the land fill, the amount, organic composition age of waste, the thickness of the overlying layer etc. [22]. Emissions from land fills, waste water and manure collection lagoons can be reduced by trapping the methane before it is released to the atmosphere, and either by flaring it or using it as an energy source. Depending on the capture efficiency, this method can reduce emission by over 90% [21].

Biomass burning releases numerous pollutants in to the atmosphere. When combustion is complete, most of the emissions consists of carbon. However, if the fires smolder and combustion is incomplete, large amounts of methane and other higher order hydrocarbons can be produced. Methane emissions from biomass burning depend on the stage of combustion reached, as well as on the carbon content of the biomass and the amount of biomass burned [23].

3.1.2 Non-biogenic sources

The main source of fossil fuel-related methane emissions are the leaks that occur during natural gas processing, transmission and distribution, since natural gas is over 90% methane. The magnitude of this source directly depends on the loss rate, which have been estimated to average between 1 to 2% of natural gas production [24]. Uncertainty remains substantial, however, as these values are based mainly on the analysis of gas systems in developed countries where transportation is likely to be more tightly controlled than in less developed nations. Regional leakage percentages have been estimated to range from 1 to 15% of total natural gas production, depending on the quality of the pipe lines, the extraction process, leakage control, the method used to estimate gas losses and other factors. Methane is also emitted from coal mines, where gas that has been trapped between layers of coal during its formation is released when the coal is mined.

Table 3.1: Estimated Sources of Methane in Tg(CH_4 yr^{-1} (based on IPCC,1995))

Source	Emissions(Tg(CH_4) yr^{-1})	Range of estimate
Wet lands	115	55-150
Termites	20	10-50
Oceans	10	5-50
Other	15	10-40
Total	160	110-210
Ruminants	85	65-100
Rise Cultivation	60	20-100
Total Agricultural	**145**	**85-200**
Natural gas	40	25-50
Coal mining	30	15-45
Petroleum industry	15	5-30
Coal combustion	15	1-30
Biomass burning	40	20-80
Waste disposal	90	55-180
Total Non agricultural Anthropogenic	215	145-380
Total	535	410-660

Global and even regional estimates of CH_4 emissions from coal and mines depend on many assumptions regarding the type of coal, the depth of the mine, mining practices, the methane content of the coal seam, whether methane is released or flared [24]. Methane emissions from coal mining and natural gas use may be more effectively reduced by altering mining practices and improving gas leakage control than by avoiding coal or gas use. If methane emitted from these sources can be used as an energy source, providing additional benefits.

3.2 Methane sinks

In contrast to the numerous sources of methane, there is only one major and two minor sinks for tropospheric methane. Reaction with hydroxyl radical (OH) is responsible for the removal of approximately 500 Tg CH_4 yr^{-1} (almost 90% of the total sink), making the concentration of OH, the most important determinant of the rate at which methane is

destroyed. The remainder of methane is removed through dry soil deposition, 30 Tg CH_4 yr^{-1} (5%) or transport to the stratosphere, 40 Tg CH_4 yr^{-1} (7%) [26]. OH is formed from the photo dissociation of tropospheric ozone and water vapor. It is the primary oxidant for most tropospheric pollutants, including, carbon monoxide, NO_x, species and organic compounds [25].

As the most abundant organic species in the atmosphere, methane plays an influential role in determining the tropospheric oxidizing capacity, initiating an important series of chemical reactions. The amount of methane removed is constrained by OH levels and the rate constant of the reaction. OH concentrations are affected not only by direct emissions of methane but by its oxidation products, especially carbon monoxide. Methane has an atmospheric life time of 8.9±0.6 yrs based on analysis of methyl chloroform and good knowledge of the loss rate with OH. Although most trace gases have a turnover time which describes the length of time they are present in the atmosphere, methane is removed by OH on an adjustment time scale that exceeds the atmospheric life time by approximately three years [27]. The feedback factor that describes this relationship, which is the ratio of the adjustment time of methane to its atmospheric life time, varies from 1.2 to 1.7 depending on which model is used in the evaluation. Comparison of 2D and 3D models suggest that the factor doesn't strongly depend on the background atmospheric OH levels [26].

This discrepancy between adjustment time and chemical life time is due to the fact that the hydroxyl radical is removed not only by interactions with CH_4, but also with its product, CO. Methane, carbon monoxide and hydroxyl are involved in the chemical feedback cycle where by even a small rise in the background level of methane-due to growing emissions, will reduce hydroxyl and produce CO.

Table 3.2: Estimated Sinks of Methane in Tg(CH_4 yr^{-1} (based on IPCC,1995))

Sink	Uptake(Tg(CH_4) yr^{-1})	Range of estimate
Tropospheric OH	445	360-530
Removal to stratosphere	40	32-48
Soil uptakes	30	15-45
Total	515	430-600

The CO produced by CH_4 oxidation will in turn be oxidized by OH causing a further drop in hydroxyl levels. This extra decrease in OH results in an increase in the life time of methane, there by enhancing the original perturbation. The result is a positive feedback, whereby increasing methane emissions can lead to an overall decrease in the oxidizing capacity of the troposphere, a slowdown in the removal of methane, and a consequent build up of methane concentrations.

3.3 The methane cycle and continuity

We will now use the idea of chemical kinetics and photochemistry to look at the reactions of methane in the atmosphere. Methane the major hydrocarbon in the atmosphere, is produced in marshes and paddy fields through the microbial degradation of organic matter that may be described by the following reaction:

$$CO_2 + 4H_2 \rightarrow CH_4 + 2H_2O. \tag{3.3.1}$$

The hydrogen for this reaction is usually derived from degradation of alcohols by non-methanogenic bacteria in the same environment. The intestines of termites and cows also provide food materials and a suitable environment within which microorganisms can produce methane, which is oxidized through intermediates, such as formaldehyde. Fig. 3.3 shows the atmospheric reactions of methane in a schematic sense. The notion of continuity helps in understanding the transfer of material along the various reaction pathways. It is particularly helpful when we have a complex set of reactions.

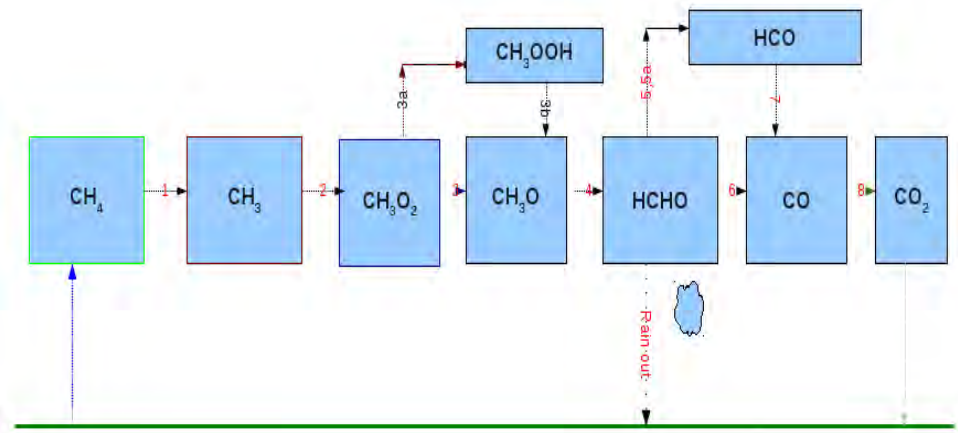

Figure 3.3: A reaction scheme for the oxidation of methane.

The reaction sequence for the oxidation of atmospheric methane represented by the numbers is explained below:

(1).$CH_4 + OH \rightarrow CH_3 + H_2O$

(2).$CH_3 + O_2 + M \rightarrow CH_3O_2 + H_2O + M$

(3).$CH_3O_2 + NO \rightarrow CH_3O + NO_2$

(3a).$CH_3O_2 + HO_2 \rightarrow CH_3OOH + O_2$

(3b).$CH_3OOH + h\nu \rightarrow CH_3O + OH$

(4).$CH_3O + O_2 \rightarrow HCHO + HO_2$

(5).$HCHO + OH \rightarrow HCO + H_2O$

(5a).$HCHO + h\nu \rightarrow HCO + H$

(6).$HCHO + h\nu \rightarrow CO + H_2$

(7).$HCO + O_2 \rightarrow CO + HO_2$

(8).$CO + OH \rightarrow CO_2 + H$

The carbon-containing species formed as HO reacts with CH_4 are indicated in Fig. 3.3. Each of transformation reactions has been reasonably well characterized in previous studies and evaluated in a recent review by Ravishankara [7]. It can be seen in Fig. 3.3 that the transformation of CH_4 into CO and ultimately into CO_2, occurs following a series of

intermediate reactions. Transient reactive species, including the HO-, HO_2,- and CH_3O_2,- radicals, are involved in the transformation, and these radicals lead to molecular products including methyl hydro peroxide (CH_3O_2H), methanol (CH_3OH), methyl peroxynitrate ($CH_3O_2NO_2$), and formaldehyde (CH_2O). The interaction of these molecular products and radicals influence the level of ozone in the atmosphere. Not shown in the Fig. 3.3 are the reactions of the transient peroxy radicals with NO in which NO_2 and ultimately O_3 are formed in the chain reaction sequence (R_1) through (R_5); O_3 is destroyed in (R_6) and (R_7):

$$HO_2 + NO \rightarrow HO + NO_2 \qquad (R_1)$$

$$CH_3O_2 + NO \rightarrow CH_3O + NO_2 \qquad (R_2)$$

$$CH_3O + O_2 \rightarrow CH_2O + HO_2 \qquad (R_3)$$

$$NO_2 + h\nu \rightarrow O(^3P) + O_2 \qquad (R_4)$$

$$O(^3P) + O_2 + (O_2/N_2) \rightarrow O_3 + (O_2/N_2) \qquad (R_5)$$

$$HO + O_3 \rightarrow HO_2 + O_2 \qquad (R_6)$$

$$HO_2 + O_3 \rightarrow HO + 2O_2 \qquad (R_7)$$

Whether ozone is made or destroyed in the troposphere depends largely on the magnitude of [NO_x] ([NO]+ [NO_2]) which is present. [NO_x] is highly variable in the troposphere, reflecting variations in the magnitudes of the anthropogenic and natural inputs of NO_x. Whether the local [NO_x] results in O_3 formation or destruction is a very important question, since the concentration of ozone is critical in determining the rate of the methane loss.

It is the consensus of scientists today that the major loss of methane in the atmosphere (90-97%) comes from its reaction with the HO-radical, and this reaction is thought to occur largely within the lower 6 km of the troposphere. There is general agreement that the elementary reaction (1) describes this process well.

Methane is emitted from the surface of the Earth at a mean rate of 2×10^{11} molecules $cm^{-2}s^{-s}$ [7]. As methane concentration in the atmosphere remain relatively constant above each cm^2 of the Earth's surface, methane must be destroyed at the same rate, i.e., 2×10^{11} molecules $cm^{-2}s^{-1}$. The same could be said of the destruction and production of the methyl radical if the reactions illustrated above were the only ones that took place in the atmosphere. Further along in the reaction scheme we see that formaldehyde is removed by four possible processes, this is a little more complicated, but obviously continuity requires that the sum of the fluxes through these four path ways be equal to the production rate. This is necessary for the system to remain in steady state. We can look back through the reaction in Fig. 3.3 and equate the destruction of formaldehyde to the production of methane at the surface of the Earth or its destruction in the atmosphere. So we can write

$$\frac{-d[CH_4]}{dt} = \frac{-d[HCHO]}{dt} \tag{3.3.2}$$

where rain-out is not very significant. This equation can be re-written as

$$K_1[OH][CH_4] = K_5[HCHO][OH] + J_{5a}[HCHO] + J_6[HCHO] \tag{3.3.3}$$

Assuming the concentration of CH_4 is $\sim$ 1.72 ppm or 4.47×10^{13} molecules cm^{-3}, and that of OH radicals to be 10^6 molecules cm^{-3}. The rate constant K_1 is 8×10^{15} molecules $cm^{-3}s^{-1}$ and the destruction rate of methane can be estimated as 3.58×10^5 molecules $cm^{-3}s^{-1}$.

Furthermore Eq. (3.3.3) can be rearranged to give

$$[HCHO] = \frac{K_1[OH][CH_4]}{K_5[OH] + J_{5a} + J_6} \tag{3.3.4}$$

So that the concentration of formaldehyde can be estimated as 4.3×10^9 molecules cm^{-3} (where K_5=$1.3\times10^{-11}cm^{-3}s^{-1}$ and J_{5a} + J_6 =$4.5\times10^{-5}s^{-s}$). This estimate of concentration is close to the mean concentration of 6.17×10^9 molecules cm^{-3} observed in the unpolluted lower atmosphere [7].

Let us now apply the notion of continuity to the formation of carbon monoxide by oxidation of methane. Carbon monoxide in the atmosphere arises from many sources, but it is easy to asses the size of the methane source. Despite the complicated path of oxidation from methane, if we neglect, the small loss due to rain-out of formaldehyde (and perhaps to a lesser extent rain-out of methyl hydro peroxide, CH_3OOH), carbon monoxide should be formed at the same rate as methane is released in the atmosphere, i.e., 2×10^{11} molecules $cm^{-2}s^{-1}$ or about 700 Tg CO yr^{-1}, this is a little larger than the amount produced by human activities (450 Tg CO yr^{-1}). Carbon monoxide it self will react with hydroxyl radicals in a process that represents an important sink for the radical.

$$OH + CO \rightarrow CO_2 + H \tag{3.3.5}$$

3.4 Effects of increasing methane emissions

Molecular hydrogen (H_2), like carbon monoxide and methane is oxidized by atmospheric OH:

$$H_2 + OH \rightarrow H_2OH \tag{3.4.1}$$

and its atmospheric mixing ratio is thus dependent on the efficiency of methane and CO oxidation by OH. As methane emission increases the OH that is available to oxidize it is reduced resulting in a nonlinear rise in methane surface mixing ratio with increasing methane surface emission. Fig. 3.4 shows the non-linear rise in the tropospheric methane mixing ratio with methane emission measured in units of a model present rate (PR) of 1PR=2.5×10^{11} molecules $cm^{-2}s^{-1}$ equivalent to 1080 Tg yr^{-1} [7].

The global mean surface temperature rise is about 1 K for a doubling in the methane emission rate which results in a methane mixing ratio that is almost 5 times the present mixing ratio.

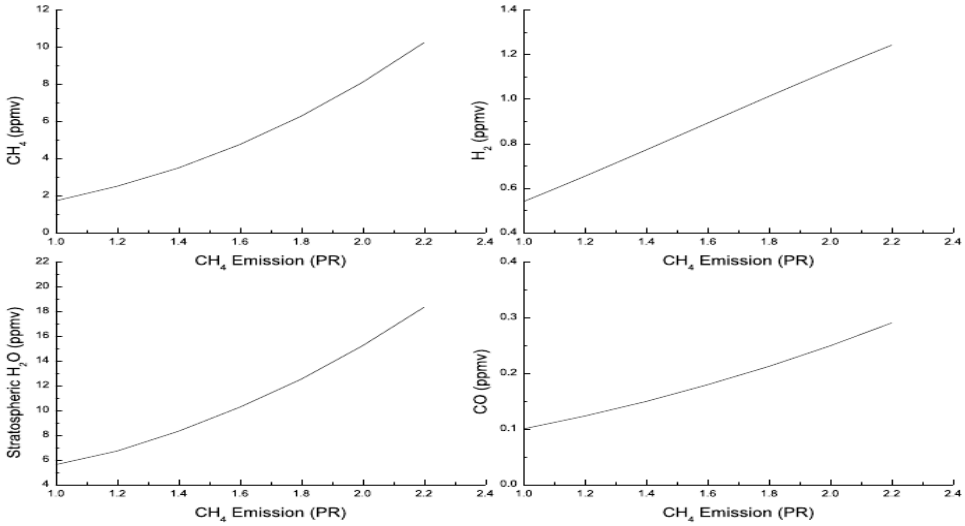

Figure 3.4: The variation of CH_4,H_2 and CO surface mixing ratios with CH_4 surface emission (1 PR $=2.5 \times 10^{11}$ molecules $cm^{-2}s^{-1}$). Also shown is the rise of global mean stratospheric H_2O mixing ratio [7],[28].

A doubling of the methane mixing ratio results in about 0.4 K rise in the mean global surface temperature. As tropospheric methane levels increase, there is an increase in tropospheric CO and H_2 , due to a reduction in OH by methane. On the other hand, increased oxidation of methane in the stratosphere results in higher watervapor mixing ratios there [7].

Chapter 4

FTIR instrumentation and retrieval techniques

Radiation measurements are important for understanding the climate system and monitoring its behavior. The most important measurements are made from instruments in space, orbiting the Earth on platforms that offer global coverage of the atmosphere and surface beneath. Ground-based remote sensing instruments also provide regional coverage of the atmosphere.

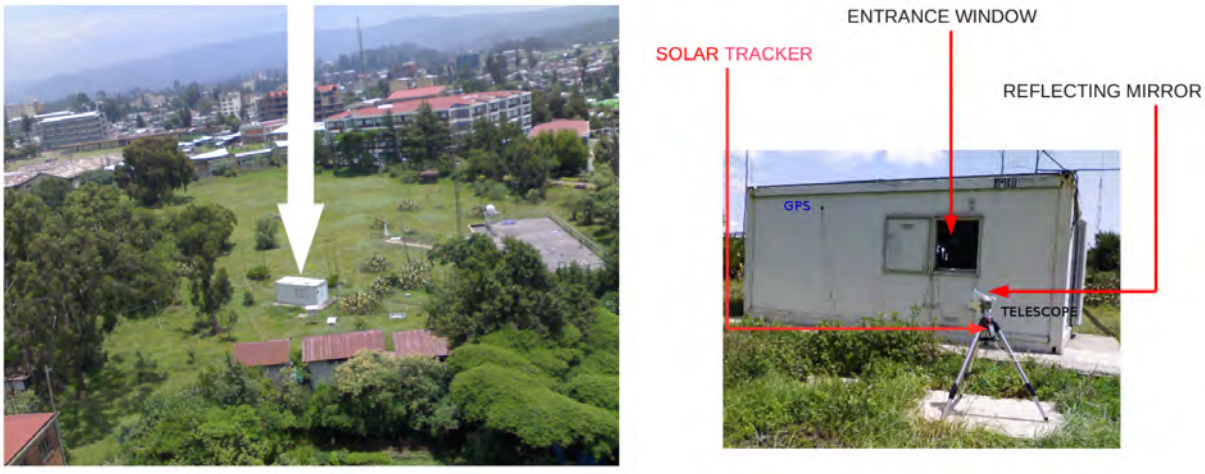

Figure 4.1: High resolution FTIR spectrometer site:Addis Ababa University Science Faculty [9.01N, 38.78E, 2450 masl].

In the preceding chapters we described how infrared absorption spectra arise for a gas of a single molecule at a given temperature and pressure; furthermore, we outlined the

equations of radiative transfer, which allow us to model the transmission of solar radiation from the top of the atmosphere to the observation point at the surface, taking into account the variable temperature, pressure, and absorber amount along the transmission path. The Fourier Transform Spectrometer (FTS), which has the ability to record solar absorption spectra with a very high resolution and over a broad wavenumber range and the theoretical background of measurement techniques are described next.

4.1 The ideal FTIR Spectrometer

FT-IR stands for Fourier Transform Infra Red, the preferred method of infrared spectroscopy. In infrared spectroscopy, IR radiation is passed through a sample. Some of the infrared radiation is absorbed by the sample and some of it is passed through (transmitted). The resulting spectrum represents the molecular absorption and transmission, creating a molecular fingerprint of the sample. Like a fingerprint no two unique molecular structures produce the same infrared spectrum. This makes infrared spectroscopy useful for several types of analysis.

FTIR instruments usually detect partially absorbed radiation emitted by the sun or reflected by the moon. This leads to a considerably faster radiative transfer calculation because atmospheric self emission can be neglected. In atmospheric science, FTIR instruments are usually applied in the infra-red region from wavenumber 700 cm $^{-1}$ to 9000 cm $^{-1}$. The instruments measure solar radiation which is partially absorbed by the constituents of the atmosphere.

The pattern of absorption versus wavenumber is used to obtain information about the altitude distribution of a certain trace gas. Due to the high frequencies, the mesosphere is not accessible with FTIR spectroscopy. FTIR spectroscopy is also dependent on Sun-light because it measures the absorption thereof and clear skies due to scattering in clouds.

The usefulness of a particular remote measurement can be described by a wide range of parameters including the spatial resolution, precision and accuracy of the retrieved product.

The FTS is based upon a Michelson interferometer, after its original designer Michelson. It is a device which uses a beam splitter to divide incoming radiation into two beams; it then introduces a phase delay between the beams, and finally, recombines them before detection. The phase delay is introduced in one arm of the interferometer by means of a moving mirror. If the source radiation is monochromatic (a delta-function in spectral space) and the moving mirror is scanned over a distance, the signal at the detector will vary sinusoidally as a function of mirror distance because the recombining beams experience successive cycles of constructive and destructive interference.

In the case of polychromatic input radiation the interference pattern at the detector will appear complicated, but will in fact be a straightforward superposition of many sinusoidal interference patterns of varying frequency and amplitude, depending on the spectrum of the source. In Fourier transform spectroscopy, the interference signal recorded at the detector is called an *interferogram*. Its Fourier transform (carried out by an external computer) yields the *spectrum* of the source in our case solar infrared radiation that has interacted with various trace gases present in the atmosphere.

The FTS divides the input beam into only two beams the minimum required for interference. This arrangement gives the FTS the ultimate in throughput and efficiency, and consequently, according to Bell [1], the concept of the two-beam interferometer is ideal and cannot be improved. The measurements reported in this thesis have been carried out using the Bruker IFS 120M Fourier transform spectrometer. It offers high resolution and very good sensitivity.

Its modular construction allows the system to be easily configured for specialized applications. The specially designed permanently aligned interferometer provides high sensitivity and stability. The computer controlled selection of optical components makes the experimental set up and spectral change easy and fast. The spectrometer has a maximum resolution of 0.009 cm^{-1} [29]. The instrument is equipped with two liquid nitrogen cooled mercury cadmium teluride (HgCdTe) and indium antimonide (InSb) detectors. The high vacuum optics bench can be evacuated to 0 hPa for distortion free baselines.

4.1.1 Mathematical basis of FTIR spectrometer

The schematic illustration of the Bruker 120M high resolution Fourier transform infrared spectrometer is shown in Fig. 4.2. The core part of the Fourier transform spectrometer is the Michelson interferometer. The Michelson interferometer is a device that divides a beam of radiation in to two parts, and recombines the two beams after a path difference has been introduced.

The interferogram, i.e., the intensity variation of the beam as a function of optical path difference (also called optical retardation) emerging from the interferometer can be measured by using a detector. The principle of a high resolution Fourier transform spectrometer its signal flow and signal processing steps are explained in the following section.

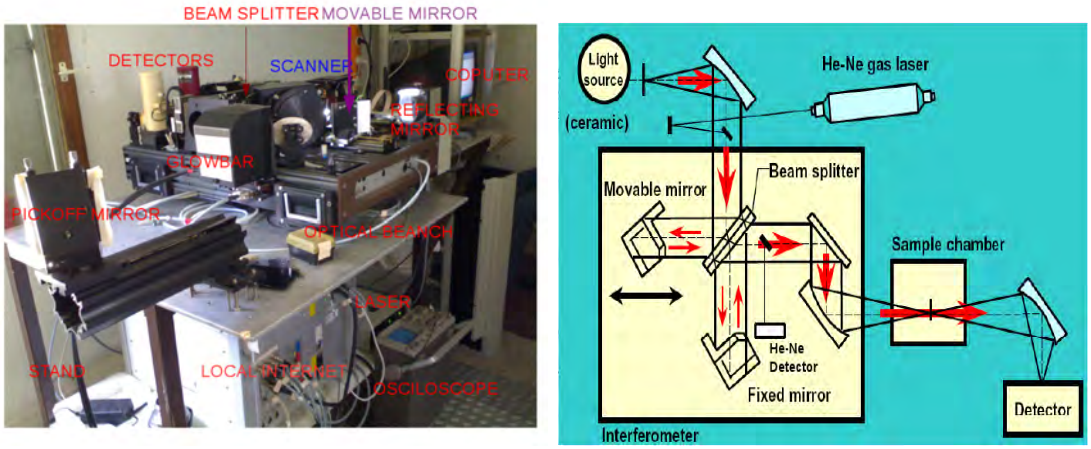

Figure 4.2: The FTIR Spectrometer.

4.1.2 Interference of light

A monochromatic electromagnetic wave with an electric field strength **E** is given by

$$\mathbf{E} = Ae^{i(\mathbf{k}.\mathbf{r}-\omega t)} \tag{4.1.1}$$

where A is the amplitude of the wave, **k** is the wave vector, **r** is the position vector, ω is the angular frequency and t is the time. In this expression

$$k = |\mathbf{k}| = \frac{2\pi}{\lambda} = 2\pi\bar{\nu} \tag{4.1.2}$$

where λ is the wavelength of the electromagnetic wave. Both k and $\bar{\nu}$ are called the wavenumber. It is convenient to express the wavenumber in the unit cm^{-1} instead of m^{-1}. Usually we are not able to measure **E** as a function of time, because the angular frequency, ω is too high. We measure the intensity, i.e., the power of the electromagnetic wave per area instead. The intensity, I is proportional to the square of the amplitude:

$$I \propto A^2 \tag{4.1.3}$$

We examine the interference of two electromagnetic waves $E_1 = A_1e^{i(k_x.x-\omega t)}$ and $E_2 = A_2e^{i(k_x.x-\omega t+\delta)}$ propagating in the same direction x.

The waves, their amplitudes and the resultant amplitude are illustrated in Fig. 4.3. The phase difference of the two waves is δ. The square of the amplitude of the resulting wave is

$$A^2 = A_1^2 + A_2^2 + 2A_1A_2cos\delta \tag{4.1.4}$$

If I_1 and I_2 are the intensities of the two interfering waves, the intensity of the interfered wave is

$$I = I_1 + I_2 + 2\sqrt{I_1I_2}cos\delta \tag{4.1.5}$$

If the two interfering waves have equal intensity that is, $I_1 = I_2 = I_o$, then the intensity of the resulting wave is simply

$$I = 2I_o(1 + cos\delta) \tag{4.1.6}$$

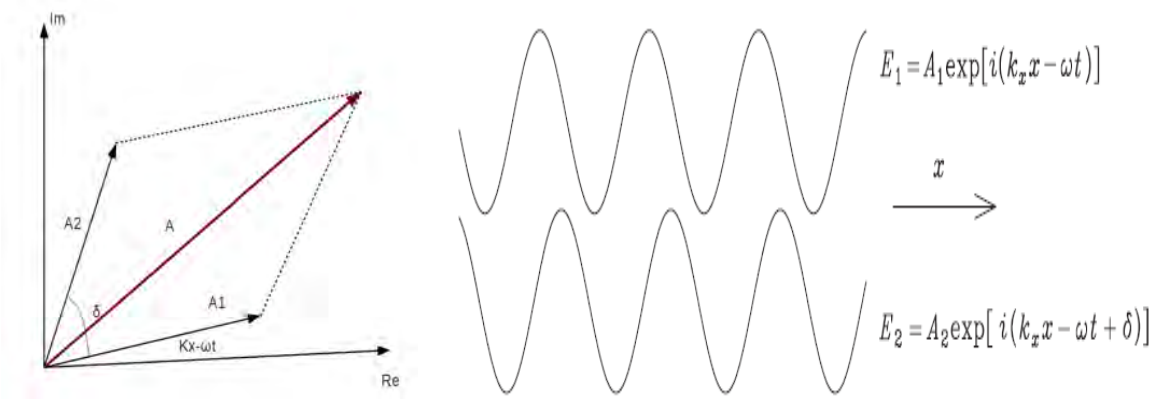

Figure 4.3: Interference of two waves E_1 and E_2. A is the resultant amplitude.

4.1.3 Michelson interferometer

The Michelson interferometer is a very simple but its principles of function can be applied to other interferometers used in Fourier transform spectroscopy, FTS. The basic optical lay out of the Michelson interferometer is illustrated in Fig. 4.4. The incident beam is

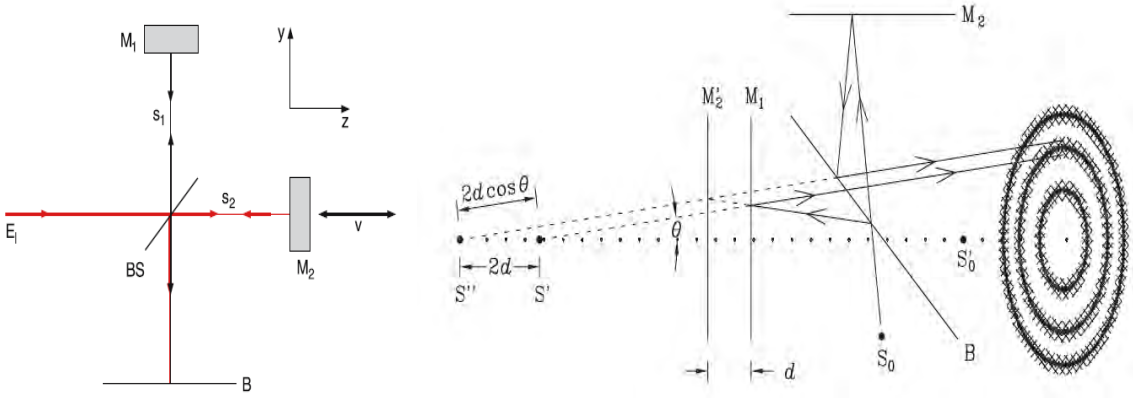

Figure 4.4: Optical lay out of Michelson interferometer (left) and the interference pattern formed by it (right).

divided by the beam splitter BS in to two parts: the reflected beam travels to a fixed mirror M_1 and back, and the transmitted beam travels to the moving mirror M_2 and back. When the two beams return to the beam splitter they interfere. Fig. 4.4 shows the rays traveling at the angel θ with respect to the optical axis of the interferometer. The optical path difference of the rays coming from the two coherent images is x =2nd cosθ, where n

is the refractive index of the medium. If the beam splitter is perfect, it divides the beam in to two equal parts with equal intensity I_o . The out put intensity of the interferometer is then, according to Eq. (4.1.6),

$$I = 2I_o(1 + cos\delta) \tag{4.1.7}$$

where the phase difference of the two rays is now

$$\delta = \frac{2\pi x}{\lambda} = \frac{2\pi}{\lambda} 2ndcos\theta \tag{4.1.8}$$

When an interference fringe pattern is obtained, intensity maxima are obtained with the condition

$$\delta = 2l\pi, l = 0, \pm 1, \pm 2, \pm 3, ... \tag{4.1.9}$$

$$2ndcos\theta = l\lambda, l = 0, \pm 1, \pm 2, \pm 3, ...$$

If θ=0 (the rays propagate in the direction of the optical axis), n=1 (the medium is vacuum) and S_o is a monochromatic point source, then the optical path difference of the two rays is $x = 2d$ and the intensity is

$$F = 2I_o[1 + cos(2\pi\bar{\nu} + 2d)] \tag{4.1.10}$$

Now assume that the spectrum of the light source S_o is continuous and consists of a wide band of wave numbers so that the spectrum of the beams in both branches of the spectrometer is $E(\bar{\nu})$ as shown in Fig. 4.5. We shall assume that the source is still a point source. At a given optical path difference (OPD) x, the interference signal from the infinitesimal spectral element $\bar{\nu}$ and $\bar{\nu} + d\bar{\nu}$ is according to Eq. (4.1.10):

$$dF(x, \bar{\nu}) = 2E(\bar{\nu})[1 + cos(2\pi\bar{\nu}x)]d\bar{\nu} \tag{4.1.11}$$

Consequently, the total signal from the whole spectral band is

$$F(x) = 2\int_0^\infty E(\bar{\nu})[1 + cos(2\pi\bar{\nu}x)]d\bar{\nu} \tag{4.1.12}$$

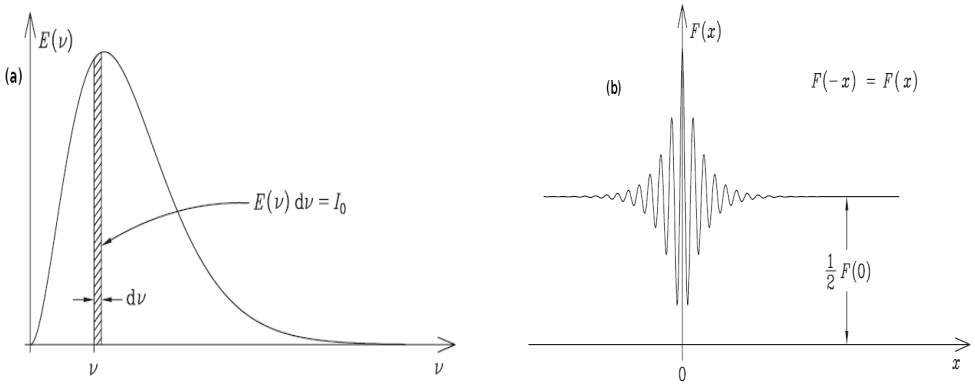

Figure 4.5: A wide-band continuous spectrum $E(\bar{\nu})$ and an infinitesimal monochromatic section of the width d$\bar{\nu}$ (a) and an interference record F(x) (b).

F(x) is called an interference record. An interference record is the total interference signal of the whole spectral band measured as a function of the OPD, x. A typical interference record is shown in Fig. 4.5. If we subtract the constant term

$$\frac{1}{2}F(0) = 2\int_0^\infty E(\bar{\nu})d\bar{\nu} \tag{4.1.13}$$

from the interference record F(x), we obtain

$$I(x) = F(x) - \frac{1}{2}F(0) = 2\int_0^\infty E(\bar{\nu})cos(2\pi\bar{\nu}x)d\bar{\nu} \tag{4.1.14}$$

$I(x)$ is called an interferogram [30].

If we define $E(-\bar{\nu}) = E(\bar{\nu})$, the computation is simplified and we obtain

$$I(x) = \int_{-\infty}^\infty E(\bar{\nu})cos(2\pi\bar{\nu}x)d\bar{\nu} = \int_{-\infty}^\infty E(\bar{\nu})e^{i2\pi\bar{\nu}x}d\bar{\nu} = \mathcal{F}[E(\bar{\nu})] \tag{4.1.15}$$

where $\mathcal{F}$ is the Fourier transform. Hence $I(x)$ and $E(\bar{\nu})$ form a Fourier transform pair, and can be written as

$$I(x) = \int_{-\infty}^\infty E(\bar{\nu})e^{i2\pi\bar{\nu}x}d\bar{\nu} = \mathcal{F}[E(\bar{\nu})] \tag{4.1.16}$$

$$E(\bar{\nu}) = \int_{-\infty}^\infty I(x)e^{-i2\pi\bar{\nu}x}dx = \mathcal{F}^{-1}[I(x)] \tag{4.1.17}$$

By denoting $E(\bar{\nu})$ the spectrum in one branch of the spectrometer, in which case the whole spectrum of source is $2E(\bar{\nu})$ we avoided extra coefficients in front of the integrals.

We can also see that

$$\mathcal{F}[\mathcal{F}^{-1}[I(x)]] = \mathcal{F}^{-1}[\mathcal{F}[I(x)]] = I(x) \tag{4.1.18}$$

Since the signal of the interferometer as a function the optical path difference and the spectrum as a function of wavenumber form a Fourier transform pair, we can apply all the properties of Fourier transforms in the calculation of the spectrum.

In FTS, the out put of measurement is generally a signal in x-domain and the most interesting information is obtained from the spectrum in $\bar{\nu}$-domain, which is calculated from the signal by inverse Fourier transform.

4.1.4 Sampling and truncation in FTS

In practice we can't compute the spectrum by Eq. (4.1.17) because the interferogram $I(x)$ is sampled only at a set of discrete points with a sampling interval Δx;

$$x_j = j\Delta x, j = -N, -N+1, -N+2, ..., -1, 0, 1, ..., N-1 \tag{4.1.19}$$

The data are collected only in the finite region from x=-L to x=L, where L=NΔx. We shall denote the interferogram samples by $I(x_j) = I_j$. We shall have to apply the discrete Fourier spectrum where the integral is replaced by a sum, that is, $\int_{-\infty}^{\infty} dx \rightarrow \Delta x \sum_{N}^{N-1}$. The spectrum is then given by

$$E_L^{\Delta x}(\bar{\nu}) = \Delta x \sum_{j=-N}^{N-1} I_j e^{-i2\pi\bar{\nu}j\Delta x} \tag{4.1.20}$$

A truncated, continuous interferogram $I_L(x)$ can be written as

$$I_L(x) = \Pi_{2L}(x) I(x) \tag{4.1.21}$$

where Π_{2L} is the boxcar function given by

$$\Pi_{2L}(x) = \begin{cases} 1, & \text{if } |x| \leq L; \\ 0, & \text{if } |x| > L. \end{cases} \tag{4.1.22}$$

The spectrum computed from the truncated interferogram is

$$\begin{aligned} E_L(\bar{\nu}) &= \mathcal{F}^{-1}[\Pi_{2L}(x)I(x)] = \mathcal{F}^{-1}[\Pi_{2L}(x)] * \mathcal{F}^{-1}[I(x)] = W_L(\bar{\nu}) * E(\bar{\nu}) \\ &= \int_{-\infty}^{\infty} W_L(u)E(\bar{\nu}-u)du \end{aligned} \tag{4.1.23}$$

where

$$W_L(\bar{\nu}) = \mathcal{F}^{-1}[\Pi_{2L}(x)] = \int_{-\infty}^{\infty} \Pi_{2L}(x)e^{-i2\pi\bar{\nu}x}dx = 2Lsinc(2\pi\bar{\nu}L) \tag{4.1.24}$$

The spectrum computed from a sampled, infinitely long (not truncated) interferogram is

$$E^{\Delta x}(\bar{\nu}) = \Delta x \sum_{j=-\infty}^{\infty} I_j e^{-i2\pi\bar{\nu}j\Delta x} \tag{4.1.25}$$

Remembering the properties of the discrete Fourier transform we can see that the discrete sampling of an interferogram with the sampling interval Δx gives a periodic spectrum $E^{\Delta x}(\bar{\nu})$ with the period $\frac{1}{\Delta x}$ that is, $E^{\Delta x}(\bar{\nu} - \frac{k}{\Delta x}) = E^{\Delta x}(\bar{\nu})$ with all integers k. The spectrum computed from the sampled, not truncated interferogram is

$$E^{\Delta x}(\bar{\nu}) = \sum_{k=-\infty}^{\infty} E(\bar{\nu} - \frac{k}{\Delta x}). \tag{4.1.26}$$

Combining the effects of truncation and discrete sampling, we obtain the spectrum $E_L^{\Delta x}(\bar{\nu})$ of a sampled, truncated interferogram.

$$\begin{aligned} E_L^{\Delta x}(\bar{\nu}) &= \sum_{k=-\infty}^{\infty} E_L(\bar{\nu} - \frac{k}{\Delta x}) \\ &= \sum_{k=-\infty}^{\infty} \delta(\bar{\nu} - \frac{k}{\Delta x}) * E_L(\bar{\nu}) \\ &= \sum_{k=-\infty}^{\infty} \delta(\bar{\nu} - \frac{k}{\Delta x}) * 2Lsinc(2\pi\bar{\nu}L) * E_L(\bar{\nu}) \\ &= [\sum_{k=-\infty}^{\infty} 2Lsinc((2\pi(\bar{\nu} - \frac{k}{\Delta x})L)] * E(\bar{\nu}) \\ &= W_L^{\Delta x}(\bar{\nu}) * E(\bar{\nu}) \end{aligned} \tag{4.1.27}$$

where

$$W_L^{\Delta x}(\bar{\nu}) = \sum_{k=-\infty}^{\infty} 2Lsinc[(2\pi(\bar{\nu} - \frac{k}{\Delta x})L] \tag{4.1.28}$$

is the instrumental profile due to truncation of the interferogram and the discrete sampling. It is also be called the instrumental function of a Fourier transform spectrometer.

4.2 Mathematical manipulations of the spectrum

The interferogram and the spectrum are Fourier transform pair. For monochromatic line, the interferogram is a cosine function; for two monochromatic lines, the interferogram shows a beat pattern, for a Lorentzian shaped single line, it is a sinusoidal interferogram with an exponentially damped envelope; and for a broad band spectrum of a polychromatic source, the result is a general interferogram which is characterized by its high center burst and two decaying side wings.

When the emission source has a broader range, the interferogram wings decay faster, because more frequency components in the source give more chance of cancellation. In any case the interferogram is the cosine Fourier transform of the source function. The computer software in the FTS converts the interferogram in to spectrum. The FT conversion also includes such necessary mathematical manipulations as apodization, phase correction, etc.

4.2.1 Interferogram sampling

The sampling of the interferogram is triggered by zero crossings of the interferogram (interference fringes), of the built-in helium-neon(HeNe) laser in the Fourier transform spectrometer. An FTS, can be configured to either double-sided or single sided interferogram [31]. This means both low resolution measurements with their improved signal-to-noise ratios and high resolution measurements are readily accommodated. Every point on an interferogram contains information about all frequencies present in the spectrum.

Because this frequency information is dependent on the distance that the mirror has moved from the interferogram center burst (the point of zero path difference-ZPD), sampling on either side of the center burst provides the same frequency information.

At lower resolutions collecting equal amounts of data before and after the center burst, i.e., a double sided data collection samples each frequency element twice and yields a nice signal-to-noise ratio. High resolution measurements require more retardation, i.e., greater mirror travel. But mechanical resolutions allow only a relatively small portion of the interferogram to be sampled before the interferogram center burst. To circumvent this limitation a single sided interferogram can be collected to achieve the desired resolution.

4.2.2 Apodization

The process of apodization is the removal of the side lobes of the lines in a spectrum by multiplying the interferogram with a suitable function prior to the Fourier transformation. A suitable function must cause the intensity of the interferogram to fall smoothly to zero at both ends [32]. Because it is impossible to collect an interferogram to infinite OPD, i.e., the interferogram has to be truncated so some error arises in the resulting spectrum. This is equivalent to multiplying the ideal interferogram by a boxcar function, so the spectrum recovered is broadened with side lobes. A practical interferogram always has a finite retardation. The product of an ideal interferogram (collected to infinite OPD), and a boxcar function is equivalent to the convolution of the true spectrum with a sinc function (with side lobes).

Apodization functions are used to correct the spectral line shape, i.e., to suppress the side lobes. The apodization is realized by multiplying the interferogram by a decaying function, i.e., the apodization function. When the interferogram is multiplied by an apodization function, the transform of the interferogram, i.e., the spectrum, is free from side lobes. The apodization function not only controls the instrument line shape (ILS) caused by the truncation of the interferogram but also smooths out the amplitude of high spatial frequencies in the interferogram. A function that has a value of unity at ZPD and decreases with increasing retardation will serve as an apodization function.

The drawback of using the apodization function is the worsening of the spectral resolution because the extremes of the interferogram wings are reduced by the apodization function. Therefore, it is necessary to make a compromise between the reduction in spectral distortion (the side lobes) and the worsening of the resolution [32].

4.2.3 Phase correction

The non zero phase phenomenon comes from the fact that the input of the sampled interferogram to the Fourier transform software is not a mirror image about zero retardation (zero optical path difference-ZOPD). It comes from the mismatching of sampling point zero retardation and optical properties such as the change of the beam slitter refractive index with wavenumber etc.

The filtering process can also bring about phase errors. In other words the phase error is caused by optical, electrical, or sampling effects such as phase lag caused by electronic filters to remove high frequency noise; even when the interferogram is symmetrical about zero optical path difference, the first data point could actually be sampled before the zero retardation point.

The result of Fourier transform of an arbitrary function is a complex function which has both real and imaginary part. The symmetric component of the interferogram contributes to the real cosine part and the asymmetric component of the interferogram brings about the imaginary sine part. In FT spectroscopy an ideal interferometer produces a symmetric interferogram about the zero path difference and only the cosine part is present in the transformed result. However, the imperfection of a real world interferometer always brings about a non zero imaginary part in the transformed results which means that the real component is distorted [32]. It is therefore necessary to correct the data for such distortion. The phase angle can be computed from a region of the interferogram measured symmetrically on either side of the zero retardation point or center burst.

4.2.4 Fourier transform

This is the final and major step in the realization of the spectrum recovery. The fast Fourier transform (FFT) algorithms make this step easier. The quality of detected spectrum is affected by many factors such as intensity of the signal source, the efficiency of the beam splitter (reflectance and transmittance) and other optics and performance of the electronics (detectors, amplifiers) ,etc.

4.3 Advantages of Fourier transform spectrometer

Compared with dispersive spectrometers using slits or dispersive elements, a Fourier transform spectrometer has some unique advantages.

1.Throughput (Jacquinot) advantage; The circular aperture of a Fourier transform spectrometer has a larger area than that of slit. The beam splitter is used instead of a dispersive element such as a diffraction grating. Therefore the signal intensity is high and more energy gets to the detector than is possible with a dispersive spectrometer. This additional energy on the detector increases the spectrum's potential signal-to-noise ratio.

2. Multiplex (Fellget) advantage; Signals of all frequencies enter the FTS and arrive at the detector at the same time and with the same signal-to-noise ratio (SNR). The measurement is faster. The time saved can be used to do more scans to reduce the detector-limited noise. (The SNR is increased by a factor of $\sqrt{N}$ after taking N measurements). A Fourier transform spectrometer doesn't separate light into individual frequencies before measurement. This means each point in the interferogram contains information from in the input light. In other words, if 100 data points along the interferogram are collected, each wavelength in the input light is sampled 100 times. By contrast a dispersive that measures 100 individual points across a spectrum samples each wavelength only once.

The throughput and the multiplex advantages allow high resolving power [32].

Together the throughput and multiplex advantages allow an FTS to obtain high quality infra-red spectrum in a fraction of time needed to get the same spectrum on a dispersive instrument.

3. Precision (Connes) advantage; The zero crossings of the interference fringes of the internal helium-neon (HeNe) laser are used to control the scanner movement and the signal sampling. Therefore, the FTS has a built-in wavenumber calibration standard of high precision. In reality however, if the reference laser is even slightly misaligned, a small wavenumber shift will be introduced. Calibration of FTS spectra against other standards of higher accuracy is necessary.

4. Computation and software advantage; The high resolution spectrum is obtained through powerful signal processing techniques such as apodization, phase correction, and Fourier transformation. In addition the FTS has the advantage of spectral resolution. To increase the resolution of a dispersive spectrometer, the slit through which light must pass needs to be narrowed, thereby decreasing the energy throughput. As the resolution increases, the advantage of a FTS over a dispersive instrument increases [32]. Also the resolution is constant for the whole spectral range for a Fourier transform spectrometer.

4.4 Linefit

Linefit is a software that was developed by Hase [29] to calculate and retrieve the instrumental line shape (ILS) using gas cell measurements. The description of retrieval procedure is that the user has to choose between either simple parameter set with a number of parameters 2 + 2w, or extended parameter set with a number of parameters 40 + 2w, w denotes as spectral windows. Simple set and extended set are coupled by adjustable regularization constraint. The actual ILS of our IFS120M instrument is determined from low pressure gas cell measurement which is filled with HBr and radiation source of glow bar about at 1273K.

The ILS of an instrument is affected by modulation loss due to self-apodization of the interferogram and a finite field of view.

For the spectra analyzed in this work, the data set includes more than 80 high resolution mid-IR solar absorption spectra ($\delta\bar{\nu} \approx 0.009\text{cm}^{-1}$) obtained with the Brucker IFS120M spectrometer at AAU Science Faculty between 2009 and 2010 for calibration. Each of these spectra includes the 400-4000 cm^{-1} region necessary for the retrieval of CH_4 as well as the retrieval of the ILS. Infrared information spectrum measured with FTS in Addis is displayed in Fig. 4.6.

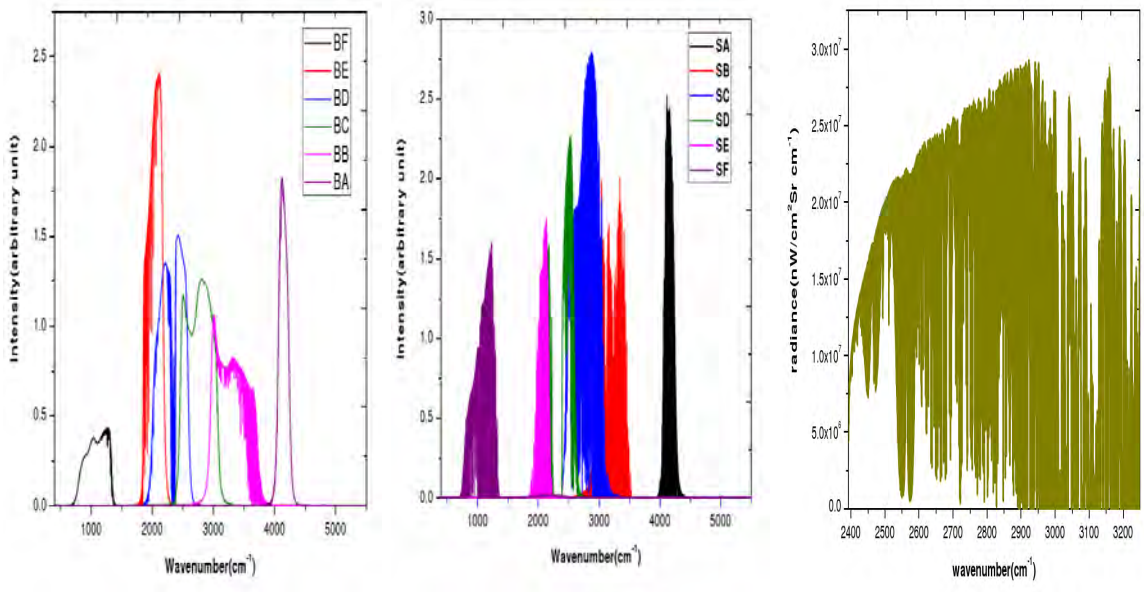

Figure 4.6: Composite spectra for different band pass filters taken at Addis in 2010. From left to right, Blackbody, Sample Spectrum, Calibrated spectrum.

Fig. 4.7 shows the retrieved ILS of IFS120M for the HBr cell measurement taken on different dates. As it is seen from the figure the ILS are similar except for the date of March 10 2010 where there is slight distortion in the ILS due to miss alignment of the FTS. The comparison of the true and ideal ILS's is done using the modulation efficiency and phase error. The real ILS differs from the ideal ILS which is determined by the applied apodization function and the self-apodization due to the non- perfect alignment.

The observed line shape can be used to retrieve atmospheric trace gas profiles because of the height dependent pressure broadening. The tropospheric trace gas total column retrieval is relatively insensitive (< 1%) to realistic distortions of the ILS from ideal. But for stratospheric gases, the real distortion of the ILS may modify retrieved total columns by amounts of up to 3% [29].

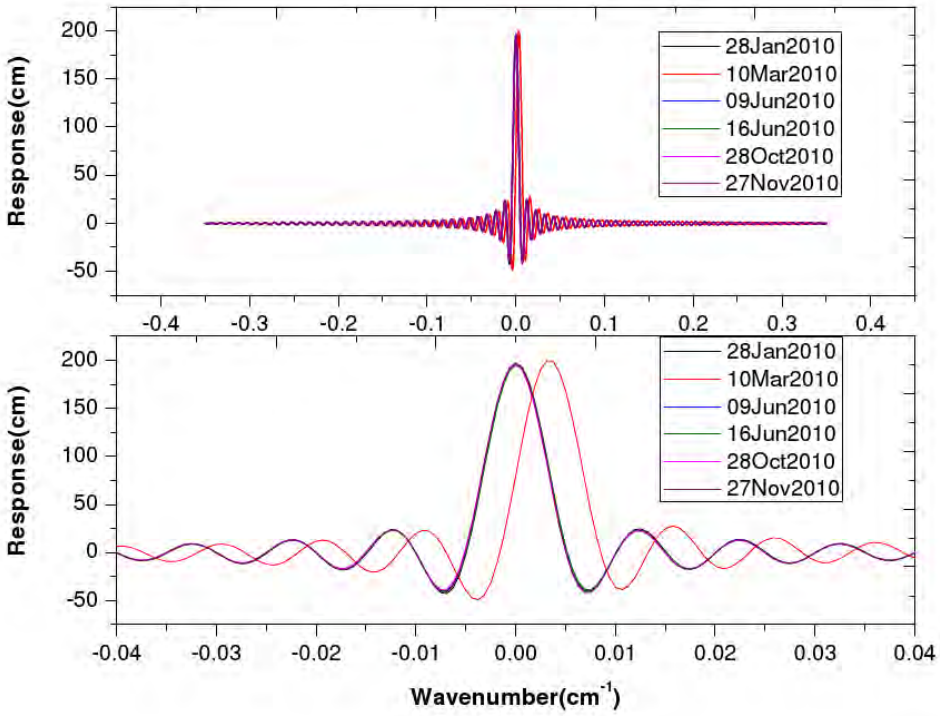

Figure 4.7: Retrieved ILS of the IFS120M in Addis Ababa for different measurement dates (plots are the same except the lower one is scaled for clarity).

Comparing the height of the peak for the six different measurement dates one can see that each period has different height, also looking to the false side lobes beside the base of the peak for each period; we can see that they are asymmetric except for March where the ILS is slightly distorted. Because changing the modulation efficiency loss will broadens or weaken ILS and varying phase error makes it either asymmetric or symmetric.

Next we look at the evolution of ILS during measurement dates. The variations in modulation efficiency and phase error of IFS120M instrument during the measurement times are displayed in Fig. 4.8.

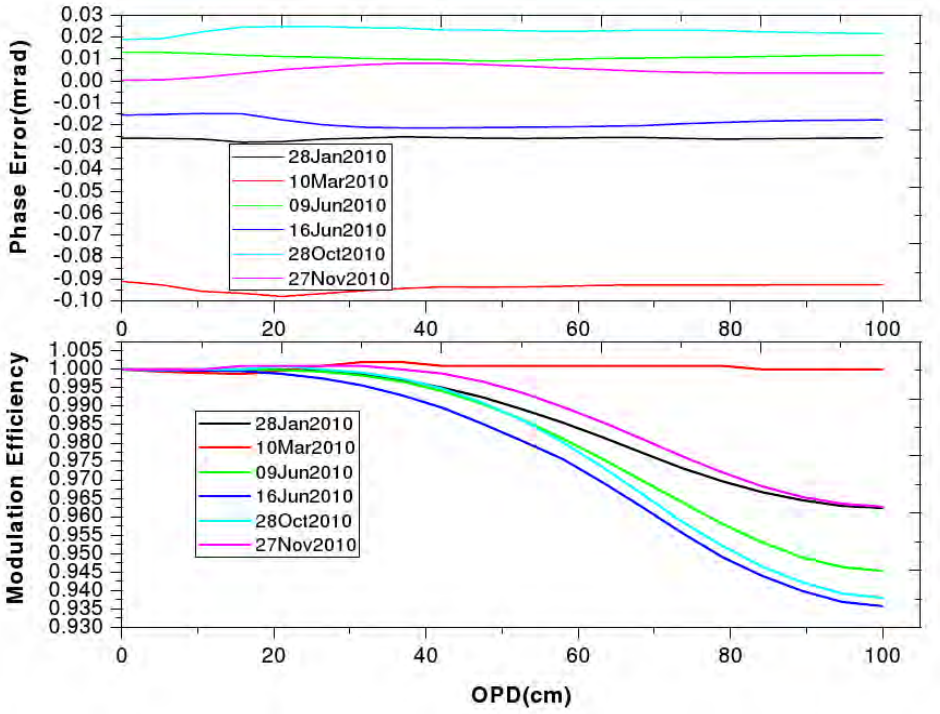

Figure 4.8: Phase error and modulation efficiency versus OPD of the Bruker IFS 120 M used during the measurements in Addis in the mentioned dates.

The retrieval of modulation efficiency is done by assuming a linear decline with the optical path difference. The resulting linear modulation efficiency loss is of the order of 0.5% on March 10 2010, while the modulation efficiency loss for the rest of measurement dates is below this value at maximum path difference.

This value is comparatively much less than the results reported in [29] showing permanent alignment of the spectrometer. The other parameter which characterizes the instrumental line shape is the phase error. Fig. 4.8 shows the variation of phase error with OPD corresponding to the time period considered for modulation efficiency. The phase error changes sign between forward and backward scans during the measurement [29]. The effect of phase error as described earlier is that it causes asymmetry in ILS.

Taking the phase error into account in the calculated spectra to fit the measured spectra helps to correct the effect of zero off-set. An ideal spectrum should show zero transmission in the center of absorbed spectral line. Uncorrected phase error will cause the center of

such a line to show non-zero transmission.

According to Griffith,et al [33], phase error affects the retrieved total columns in two

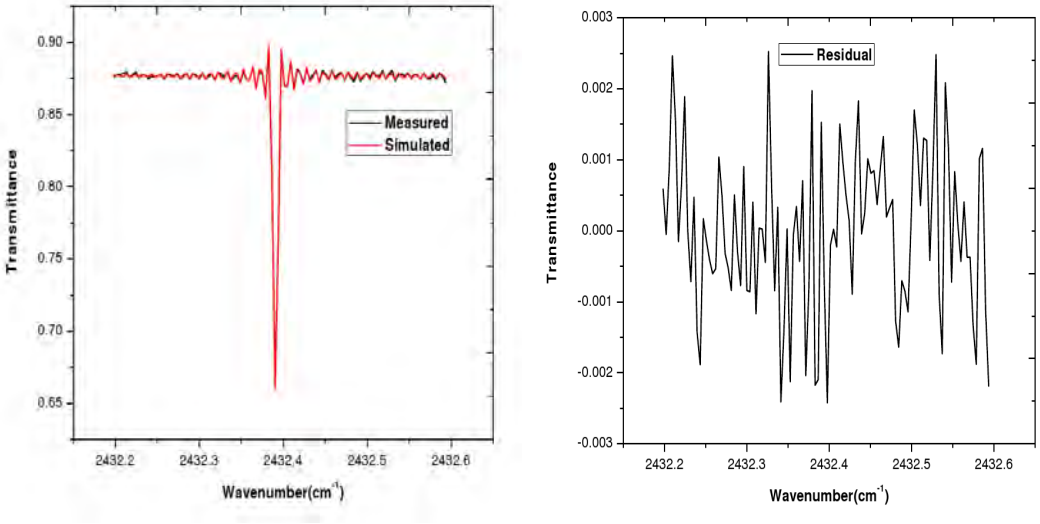

Figure 4.9: The measured and simulated transmittance spectral fit from HBr cell measurement (left) and the corresponding residual spectra between the measured and calculated spectra (right) for the date of 16 June, 2010.

separate ways; first, through the change in line shape of the actual absorption line and second, through a change in the effective continuum level at the center of the absorption line nearby whose wings overlap the narrow line of interest. In the later case the phase error distorts the strong band and affects the local zero and continuum levels in the observed spectrum. Fig. 4.8 represents the evolution of ILS during the measurement periods in Addis Ababa using IFS120M instrument.

Finally we present the spectral fits of the measurement on one of the above measurement dates 16 Jun 2010. Fig. 4.9 shows the HBr spectral fit for the indicated wavenumber region. The left panel is a plot of the measured and calculated transmission spectra and the right panel is the residual between the two spectra.

Chapter 5

Analysis of ground-based solar absorption FTIR spectra

A common problem in atmospheric remote sensing is to estimate the vertical profiles of atmospheric parameters from spectroscopic measurements. From a computational point of view, the basic problem is the inversion of observed spectra to obtain profiles of constituent concentrations. The discretization of the radiative transfer equation leads to data model y=F(x) where the mapping F:$\mathbb{R}^n \rightarrow \mathbb{R}^m$ represents the forward model, $\mathbf{y} \in \mathbb{R}^m$ is the exact data vector, $\mathbf{x} \in \mathbb{R}^n$ is the state vector containing the discrete representation of the atmospheric profile to be retrieved (e.g., molecular density profiles at different altitudes), and $\mathbb{R}^n$ is the n-dimensional real Euclidean space. The goal of FTIR experiment is to measure vertical profiles and column amount of methane. To obtain these target quantities from measurement an inverse problem has to be solved. There exists various methods to solve such kind of problems. In most cases it is set up as a least square problem, where the different solution formula are quite similar.

In this work different applications of both the optimal estimation (OE) and Tikhonov-Philips (TP) formalism are used as appropriate. The impact of constraints is shown under considerations of diagnostic tools such as retrieval error, vertical resolution and degrees of freedom.

5.1 Problem Description and Definitions

The retrieval problem in atmospheric remote sounding is to extract vertical profiles of atmospheric state parameters from sequence of absorption spectra of different heights. An exact physical description of the problem requires continuous functions. The vertical profiles to be retrieved are continuous functions with height while the spectrum is continuous function with frequency. Measurements are always discrete in nature. In this sense most of inverse problems are ill-posed [34].

To overcome this, the continuous functions of the vertical profiles are discretely sampled and arranged in a state vector $\mathbf{x} \in \mathbb{R}^n$ of unknown quantities where by we will apply in the following the terminology used by Rodgers [34]. This vector contains the finite number of unknown quantities which shall be determined in the retrieval. The width of the grid on which the atmospheric state parameters are represented depends both on practical considerations and on required altitude resolution.

The m-dimensional measurement vector $\mathbf{y}$ contains all measured radiances to be considered for inversion. The measurement is superimposed by instrumental random noise. The correlation between the state vector $\mathbf{x}$, the measurement vector $\mathbf{y}$, the m-dimensional noise vector ϵ and the radiative transfer model $\mathbf{F}$ is given by

$$\mathbf{y} = \mathbf{F}(\mathbf{x}) + \epsilon \tag{5.1.1}$$

While the forward model maps from state space (vertical profiles) into measurement space (absorption spectra) we are interested in the inverse mapping, i.e., an appropriate determination of the state vector $\mathbf{x}$ from measurements. In our case the inverse problem is formally over-determined i.e.,the number of measurements is higher than the number of state parameters(m>n). So the inverse problem can be formulated as least square problem.

$$\|\mathbf{y} - \mathbf{F}(\mathbf{x})\|^2_{S_\epsilon^{-1}} = [(\mathbf{y} - \mathbf{F}(\mathbf{x})]^T S_\epsilon^{-1}(\mathbf{y} - \mathbf{F}(\mathbf{x})) \tag{5.1.2}$$

where S_ϵ is the covariance matrix of the measurement.

The non linearity of $\mathbf{F}(\mathbf{x})$ often requires Eq. (5.1.2) to be solved by Newtonian iteration [35].

$$\mathbf{x}_{i+1} = \mathbf{x}_i + (\mathbf{K}_i^T S_\epsilon^{-1} \mathbf{K}_i)^{-1} \mathbf{K}_i^T S_\epsilon^{-1} (\mathbf{y} - \mathbf{F}(\mathbf{x}_i)) \tag{5.1.3}$$

where $\mathbf{K}$ is the Jacobian of $\mathbf{F}$ with respect to $\mathbf{x}$ and the subscript i denotes the iteration index. This solution uses information only from the measurement. Additional information about the solution can be included by including a constraining term. This can be a climatology derived from set of independent measurements of the atmospheric constituents to be retrieved.

$$\|\mathbf{y} - \mathbf{F}(\mathbf{x})\|^2_{s_\epsilon^{-1}} + \mathcal{R}(\mathbf{x}, \mathbf{x}_a, \mathbf{R}) = [(\mathbf{y} - \mathbf{F}(\mathbf{x})]^T S_\epsilon^{-1} (\mathbf{y} - \mathbf{F}(\mathbf{x})) + (\mathbf{x} - \mathbf{x}_a)^T \mathbf{R} (\mathbf{x} - \mathbf{x}_a) \tag{5.1.4}$$

where $\mathcal{R}$ is the constraining function [36], $\mathbf{x}_a$ is an a priori known state vector and $\mathbf{R}$ is a regularization matrix. The resulting iterative solution is then given by

$$\mathbf{x}_{i+1} = \mathbf{x}_i + (\mathbf{K}_i^T S_\epsilon^{-1} \mathbf{K}_i + \mathbf{R})^{-1} [\mathbf{K}_i^T S_\epsilon^{-1} (\mathbf{y} - \mathbf{F}(\mathbf{x}_i)) - \mathbf{R}(\mathbf{x}_i - \mathbf{x}_a)] \tag{5.1.5}$$

Based on the choice of the regularization matrix, different kinds of constraints can be included in the least squares problem.

5.2 Retrieval Strategy

The iterative solution given by Eq. (5.1.5) can be seen as a weighted mean of the information contained in the measurement and the information added by the constraint. Determination of the appropriate weight of the constraint is a critical part of the design of any retrieval strategy. Different kinds of constraints can be implemented to solve inverse problems such as optimal estimation (OE), Tikhonov regularization. In case of optimal estimation the difference between the a priori profile $\mathbf{x}_a$, and the solution is kept small. The regularization matrix is $\mathbf{R} = S_a^{-1}$, the inverse of the a priori matrix, and the iterative solution is

$$\mathbf{x}_{i+1} = \mathbf{x}_i + (\mathbf{K}_i^T S_\epsilon^{-1} \mathbf{K}_i + S_a^{-1})^{-1} [\mathbf{K}_i^T S_\epsilon^{-1} (\mathbf{y} - \mathbf{F}(\mathbf{x}_i)) - S_a^{-1} (\mathbf{x}_i - \mathbf{x}_a)] \tag{5.2.1}$$

Has the inverse of the covariance matrix for the measured profile $\mathbf{K}^T S_\epsilon^{-1}\mathbf{K}$ larger entries than the inverse of a priori covariance matrix S_a^{-1}, the retrieval is dominated by the measurement with its noise. The same considerations can be applied vice versa.

If the a priori information comes from an independent measurement or if $\mathbf{x}$ is part of a climatological ensemble, following Gaussian statistics which is represented by $\mathbf{x}_a$ and S_a, the optimal estimation is the most probable solution [34]. However, if there is no independent measurement, which provides $\mathbf{x}_a$ and if $\mathbf{x}$ is not part of the statistical ensemble which is represented by $\mathbf{x}_a$ and S_a, the result is to some degree biased towards the a priori profile. A solution constrained in its shape only rather than in its absolute value may be more desirable in order not to miss unexpected atmospheric phenomena. For this purpose Tikhonov regularization is a powerful tool.

In case of Tikhonov regularization the matrix becomes $\mathbf{R} = \alpha\mathbf{L}^T\mathbf{L}$, where α is a regularization parameter and $\mathbf{L}$ is a regularization matrix. This kind of regularization is also known as Twomey or Philips [36] regularization and the iterative solution is given by

$$\mathbf{x}_{i+1} = \mathbf{x}_i + (\mathbf{K}_i^T S_\epsilon^{-1}\mathbf{K}_i + \alpha\mathbf{L}^T\mathbf{L})^{-1}[\mathbf{K}_i^T S_\epsilon^{-1}(\mathbf{y} - \mathbf{F}(\mathbf{x}_i)) - \alpha\mathbf{L}^T\mathbf{L}(\mathbf{x}_i - \mathbf{x}_a)] \tag{5.2.2}$$

The parameter α determines the weight of the regularization and it is also important to choose α appropriate to the problem. One way to fix this parameter is the L-curve method [37]. There are several possibilities to set up regularization matrix $\mathbf{L}$, the simplest one being the identity matrix, $\mathbf{I} = \mathbf{L}$. This results in a retrieval equivalent to the optimal estimation with a diagonal a priori covariance matrix $S_a = \frac{1}{\alpha}\mathbf{I}$. In order to obtain a smooth solution the discrete first derivative operator is useful as a smoothing matrix, $\mathbf{L} = \mathbf{L}_1$.

The discrete first derivative operator can be derived as follows: the first derivative can be approximated as

$$\mathbf{x}_k' \approx \frac{\mathbf{x}_k - \mathbf{x}_{k-1}}{z_k - z_{k-1}} \tag{5.2.3}$$

where $\mathbf{x}_k$ is the state parameter at height z_k.

By approximation of the first derivative by a differential quotient and in case of equivalent altitude grid the operator is defined as

$$\begin{pmatrix} \mathbf{x}^{2\prime} \\ \vdots \\ \mathbf{x}^{n\prime} \end{pmatrix} \approx \begin{pmatrix} -1 & 1 & 0 & \cdots & 0 \\ 0 & -1 & 1 & \ddots & \vdots \\ \vdots & \ddots & \ddots & \ddots & 0 \\ 0 & \cdots & 0 & -1 & 1 \end{pmatrix} \begin{pmatrix} \mathbf{x}^{1} \\ \vdots \\ \mathbf{x}^{n} \end{pmatrix} = \mathbf{L}_1 \mathbf{x} \tag{5.2.4}$$

This and higher order kind of operator act just in smoothing not biasing the solution. In the case that two different types of state parameters being jointly fitted, which require different approaches of regularizations, it is necessary to have one formalism which supports both types of constraints. In order to gain understanding of the smoothing effect of the off-diagonal elements of S_a, we to express $\alpha \mathbf{L}_1^T \mathbf{L}_1$ by a matrix of the format of an inverse covariance matrix as

$$S_a^{-1} = \alpha \mathbf{L}_1^T \mathbf{L}_1 \tag{5.2.5}$$

This means that an a priori covariance matrix can be set up that acts approximately in the same way as the discrete first derivative operator $\mathbf{L}_1$. This equivalence is only approximate since truncation of the expansion causes a regular matrix S_a^{-1} being transformed to a singular matrix of the form $\mathbf{L}_1^T \mathbf{L}_1$. Therefore optimal estimation formalism can be used either in the original sense of weighting the measured and the a priori profile or in the sense of smoothing the solution without considerably shifting it towards the a priori profile. Because of the approximate equivalence of OE and TP regularization methods, we henceforth use the optimal estimation terminology.

5.3 Diagnostics

Following Rodgers [34] a number of diagnostic tools are available and will be used for assessment of the retrieval. These include: covariance matrix of the retrieved solution,

averaging kernel matrix and degrees of freedom. The covariance matrix of the solution includes the estimated error of the state parameters and their inter-level correlations:

$$\hat{\mathbf{S}} = (\mathbf{K}^T S_\epsilon^{-1} \mathbf{K} + S_a^{-1})^{-1} \tag{5.3.1}$$

Another important quantity to assess the retrieval is the *vertical resolution*. The vertical resolution depends on the sensitivity of the retrieval to changes in the true profile:

$$\mathbf{A} = \frac{\partial \hat{\mathbf{x}}}{\partial \mathbf{x}} = \mathbf{D}_y \mathbf{K} \tag{5.3.2}$$

where $\hat{\mathbf{x}}$ is the estimated profile in the linear case and $\mathbf{D}_y$ describes the sensitivity of the retrieval concerning changes in the measurement:

$$\mathbf{D}_y = \frac{\partial \hat{\mathbf{x}}}{\partial \mathbf{y}} \tag{5.3.3}$$

The matrix $\mathbf{A}$ is usually called the averaging kernel matrix. There are several ways to define the vertical resolution of the retrieval as a function of $\mathbf{A}$ [38] .We define the vertical resolution as the width at the half maximum of the column of the the averaging kernel matrix. The averaging kernel matrix for the the optimal estimation is calculated as

$$\mathbf{A} = (\mathbf{K}^T S_\epsilon^{-1} \mathbf{K} + S_a^{-1})^{-1} \mathbf{K}^T S_\epsilon \mathbf{K} \tag{5.3.4}$$

If there is no constraining term in the least square problem Eq. (5.1.2), the averaging kernel matrix is the identity matrix $\mathbf{I}$. In this case the altitude resolution is determined by the grid used for representation of $\mathbf{x}$. The estimated solution for optimal estimation can also be expressed in terms of the averaging kernel.

In the linear case the gained equation allows to separate the true parameters and the a priori parameter. The estimated solution is

$$\begin{aligned} \hat{\mathbf{x}} &= \mathbf{x}_a + \mathbf{A}(\mathbf{x} - \mathbf{x}_a) + \mathbf{D}_y \epsilon \\ \hat{\mathbf{x}} &= \mathbf{A}\mathbf{x} + (\mathbf{I} - \mathbf{A})\mathbf{x}_a + \mathbf{D}_y \epsilon \end{aligned} \tag{5.3.5}$$

where the averaging kernel $\mathbf{A}$ is the weight of the true state, the matrix $(\mathbf{I} - \mathbf{A})$ is the weight of the true a priori state and $\mathbf{D}_y$ the weight of the noise. In case of no constraints

($\mathbf{I} = \mathbf{A}$), the a priori part of Eq. (5.3.5) disappears and the result depends only on the true state and the noise.

Because the matrices of the weights $\mathbf{A}$,$(\mathbf{I}-\mathbf{A})$ and $\mathbf{D}_y$ are usually non diagonal, it is not trivial to quantify the different parts of the retrieval formula Eq. (5.3.5). A transformation in space where the matrices described above become diagonal is proposed by Rodgers [34]. For this purpose the Jacobian $\mathbf{K}$ has to be transformed and a singular value decomposition (SVD) is performed [39]:

$$\tilde{\mathbf{K}} = S_\epsilon^{-\frac{1}{2}} \mathbf{K} S_a^{\frac{1}{2}} = \cup \wedge \vee^T \tag{5.3.6}$$

where $\cup$ and $\vee$ are orthogonal matrices and $\wedge$ is a diagonal matrix with the singular values λ_i of $\tilde{\mathbf{K}}$ as its diagonal elements. Moreover $\cup$ is mxn matrix, $\vee$ and $\wedge$ are nxn matrices. The state vector and the noise vector are transformed as follows

$$\begin{aligned} \mathbf{x}' &= \vee^T S_a^{-\frac{1}{2}} \mathbf{x} \\ \epsilon' &= \cup^T S_\epsilon^{-\frac{1}{2}} \epsilon \end{aligned} \tag{5.3.7}$$

with the singular value decomposition of $\tilde{\mathbf{K}}$ (Eqs. (5.3.6) and (5.3.7)) we get for the transformed estimated state parameters

$$\hat{\mathbf{x}}' = [\mathbf{I} + \wedge^2]^{-1} \wedge^2 \mathbf{x}' + [\mathbf{I} + \wedge^2]^{-1} \mathbf{x}'_a + [\mathbf{I} + \wedge^2]^{-1} \wedge \epsilon' \tag{5.3.8}$$

The matrices in the different addends are diagonal now. So Eq. (5.3.8) can be written component wise as

$$\hat{\mathbf{x}}'_i = \frac{\lambda_i^2}{1+\lambda_i^2} \mathbf{x}'_i + \frac{1}{1+\lambda_i^2} \mathbf{x}'_{ai} + \frac{\lambda_i}{1+\lambda_i^2} \epsilon'_i \tag{5.3.9}$$

We can see from Eq. (5.3.9) that the transformed state parameter $\hat{\mathbf{x}}'_i$ is dominated by the true profile if the corresponding singular value is much larger than 1 ($\lambda_i \gg 1$). For cases $\lambda_i \ll 1$, the corresponding state parameter is determined by the priori knowledge. For singular values $\lambda_i \approx 1$, the estimated state parameter is influenced by the true state, the a priori state and the noise with the same weight.

Eq. (5.3.9) leads to the definition of the degrees of freedom for signal [34].

$$d_s = \sum_i \frac{\lambda_i^2}{1+\lambda_i^2} \tag{5.3.10}$$

The singular values with $\lambda_i \ll 1$ do not contribute to the degrees of freedom because they will be determined by the a priori knowledge. Therefore the number of degrees of freedom is not fixed with the dimension of the state apace n but rather with the quantity computed within Eq. (5.3.10). The diagnostic tools where the singular value decomposition of the transformed Jacobian is used is for the special application to the optimal estimation formalism.

5.4 Error Estimation

Any error modifies the spectrum, thereby disturbs the retrieved quantities. This section provides a brief description of the error estimation, which includes measurement, smoothing and interfering species error.

The error estimation assumes that, we are in an incrementally linear regime, and that we could estimate our FTIR retriever result with a linear equation which uses a complete knowledge of the true state and radiance error vector.

$$\mathbf{x}_{est} = \mathbf{x}_a + \mathbf{G}\epsilon + \mathbf{A}(\mathbf{x}_{true} - \mathbf{x}_a) + \mathbf{G}\mathbf{K}_b(\mathbf{b}_{true} - \mathbf{b}_{est}) \tag{5.4.1}$$

Where $\mathbf{A}$ is the averaging kernel, $\mathbf{x}_a$ is the a priori constraint vector, $\mathbf{x}_{true}$ is the true state, $\mathbf{G}$ is the gain matrix, ϵ is the measurement error, $\mathbf{K}_b$ is the Jacobian matrix of the interfering species and $\mathbf{b}$ is the state of the interfering species. $\mathbf{A}$ and $\mathbf{G}$ are calculated from the Jacobian of the retrieved species, the constraint matrix and the estimated radiance errors.

The estimated error covariance is defined as

$$\mathbf{S}_{err} = \langle(\mathbf{x}_{est} - \mathbf{x}_{true})(\mathbf{x}_{est} - \mathbf{x}_{true})^T\rangle \tag{5.4.2}$$

This error covariance can be calculated using Eq. (5.4.1)

$$\mathbf{S}_{err} = \underbrace{(1-\mathbf{A})\mathbf{S}_a(1-\mathbf{A})^T}_{smoothing} + \underbrace{\mathbf{G}\mathbf{S}_m\mathbf{G}^T}_{measurement} + \underbrace{\mathbf{G}\mathbf{K}_b\mathbf{S}_b(\mathbf{G}\mathbf{K})^T}_{systematic} \tag{5.4.3}$$

where $\mathbf{S}_a$ is the a priori covariance of the retrieved state, i.e, $\langle(\mathbf{x}_{ini}-\mathbf{x}_{true})(\mathbf{x}_{ini}-\mathbf{x}_{true})^T\rangle$, $\mathbf{S}_m$ is the measurement error covariance and $\mathbf{S}_b$ is the error covariance of the interfering species. The square root diagonal of Eq. (5.4.3) gives "error bars" commonly reported and the various terms are helpful to determine the sizes of the various error components.

Chapter 6

Results and discussion

Analysis of the results obtained after employing a scheme in chapter five is discussed in detail. We present the detail results in this chapter.

6.1 CH_4 spectral signature in the mid-infrared

6.1.1 spectral regions

For the retrieval 5 optimum spectral regions (micro windows) have been selected using Automatic Line Finding Program (ALFIP) between 2804.670cm^{-1} and 2854.155 cm^{-1}. The main criterion for selection is high sensitivity to methane and low interference by other gases. However, the contribution of other gases still needs to be considered even after careful micro window selection. These interfering gases are H_2O, N_2O and O_3.
The retrieval procedure follows a scheme described by Eq. (5.1.5) where $\mathbf{x}$ is the retrieval vector, $\mathbf{K}$, the partial derivatives of the spectra with respect to the retrieval vector (Jacobian) ,$\mathbf{S}_\epsilon$, the covariance matrix due to measurement noise, $\mathbf{R}$, the regularization or constraint matrix, $\mathbf{y}$, measurement vector, $\mathbf{F}$, the forward model, $\mathbf{x}_a$, the a priori profile and i the iteration index. The retrieval is performed on a fine vertical grids from 2.45 to 85 km and is stabilized by a first order Tikhonov constraint, R=$\alpha L_1^T L_1$, where α is the strength of the constraint and L_1 is the first order derivative [40], which smooths the solution without biasing it towards the a priori profile.

Table 6.1: List of micro windows used for methane inversion. For each of them the interfering species adjusted during the retrieval procedure are included.

No	**Micro window bounds** (cm^{-1})	**Target gas**	**Interfering species**
1.	2804.670000 - 2805.430000	CH_4	N_2O,H_2O,O_3
2.	2876.790000 - 2877.370000	CH_4	N_2O,H_2O,O_3
3.	2888.315000 - 2888.765000	CH_4	N_2O,H_2O,O_3
4.	2825.510000 - 2825.870000	CH_4	N_2O,H_2O,O_3
5.	2853.545000 - 2854.155000	CH_4	N_2O,H_2O,O_3

The regularization strength α, is determined by finding a trade-off between the number of degrees of freedom (measure of amount of information in methane retrieval), which is given by the trace of the averaging kernel [34] and the noise induced error [40]. A regularization strength α, of 2.5×10^4 was found optimum.

The code to simulate the observed spectrum calculates the radiative transfer equation iteratively through 41-layer atmosphere. Following this calculation the radiance is convolved with the FTIR instrument line shape and then apodized with boxcar medium apodization. The absorption parameters used in the calculations were pre-calculated using a line-by-line code and the HITRAN 2006 [41] molecular spectroscopic database which are calculated for each of 41 atmospheric layers.

Each retrieval step minimizes a cost function (Eq. 5.1.2) using a Tikhonov-Philips (TP) non linear least square algorithm [PROFFIT (V9.5)] where the cost function chosen considers both spectroscopic fit over the spectral windows used and our a priori knowledge of the atmosphere. The spectral windows are selected to maximize the information content of a retrieval given an expected a priori covariance.

The methane a priori profiles are created from tropical climatology and combined into a single profile using interpolation.

Three of the spectral regions (micro windows) used in this study to retrieve the target gas (CH_4) together with the fitted species are displayed in Fig. 6.1.

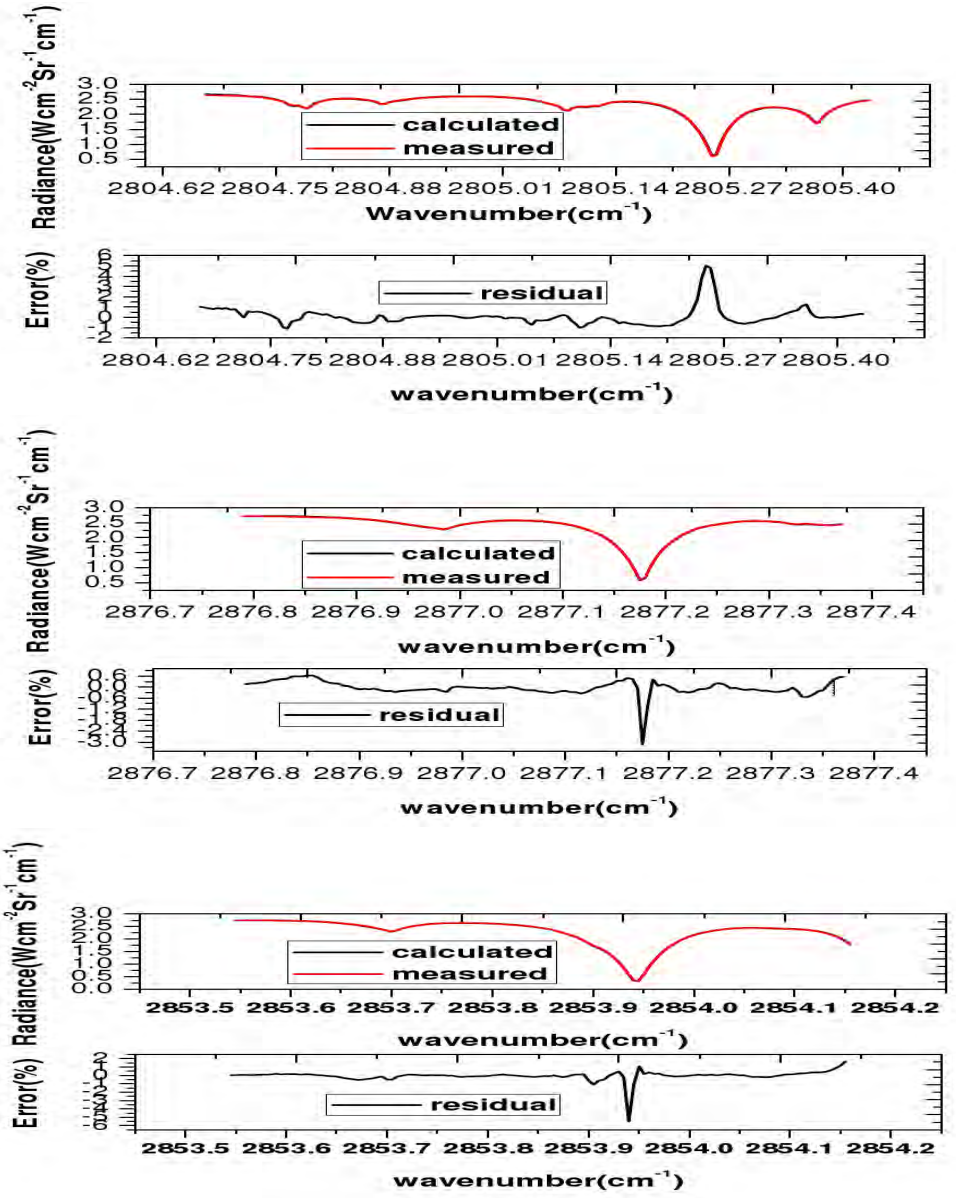

Figure 6.1: Multiple micro-window fit of CH_4 and interfering species. Measured (red) calculated (black) spectra are shown (upper plots) together with residuals (lower plots).

All settings (micro-windows, constraint, initial guess and a priori profile) are chosen in such a way that all the structures visible in the retrieved distributions originate from the measurements and are not artifacts due to any constraints. The retrieved result of the experiment is displayed in Table 6.2.

Table 6.2: Methane retrieval results and uncertainties for some selected altitudes.

altitude(km)	2.45	2.94	3.556	4.208	4.896	5.62	30.69	69.77	85.00
a priori(ppmv)	1.768	1.768	1.767	1.767	1.767	1.768	1.303	0.118	0.049
retrieved(ppmv)	1.784	1.784	1.783	1.782	1.781	1.781	1.402	0.129	0.054
uncertainty(%)	0.695	0.689	0.671	0.638	0.590	0.531	1.355	0.147	0.061

6.1.2 Single profile retrieval of methane and diagnostics

The retrieval procedure described in the previous chapter has been applied to real FTIR measurements. Fig. 6.2 shows a single profile retrieval of CH_4 for FTIR on 28-11-2009 at 9.01^{o}N, 38.76^{o}E which is right over Addis Ababa.

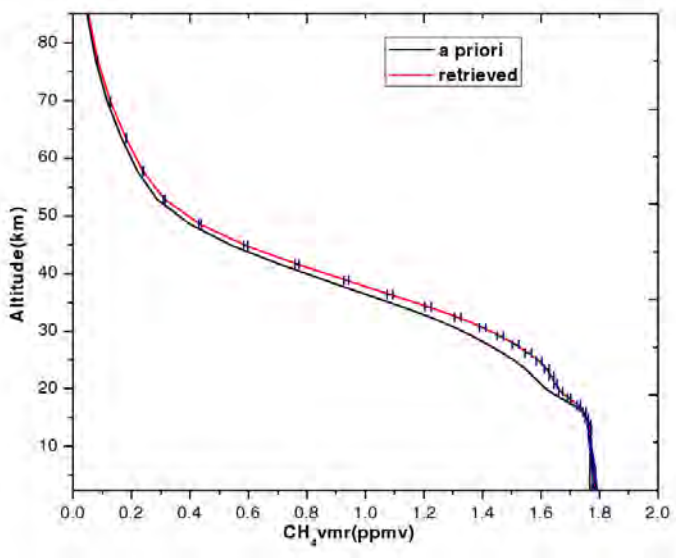

Figure 6.2: Vertical profile of methane (CH_4) retrieval result (FTIR, 28-11-09, 9.01^{o}N, 38.76^{o}E with error bars).

From the profile we observe a maximum value of 1.784 ppmv at the observation point with a minor shift from the a priori which is of reasonable size. We also see that the volume mixing ratio of methane rapidly decreases with altitude just above 28 km. The uncertainty of the retrieval is shown on the same figure as error bar (navy) with magnitude of 0.00695 ppmv at the observation point and 0.0006094 ppmv at 85 km.

It is useful to consider the smoothed profiles and analyze a priori what kind of raw features of the real atmosphere are expected to be observable in the retrieved profiles.

The averaging kernels are commonly used for this purpose as they give an impression of the vertical resolution of the retrieved profiles.

Fig. 6.3 shows the averaging kernels for the retrieved mixing ratios. The amplitude of the averaging kernels indicate the sensitivity of the retrieval and the full widths at half maximum (FWHM) indicates the vertical resolution of the corresponding layer. At

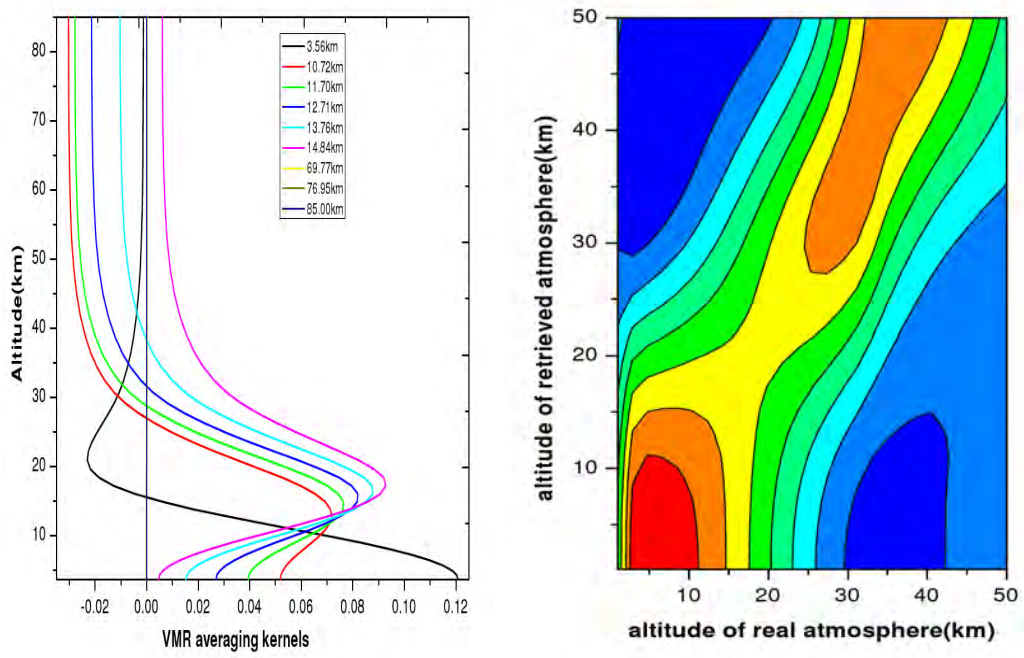

Figure 6.3: Averaging kernels for retrieved mixing ratios for some selected altitudes (left), correlations between real atmosphere and retrieved atmosphere (right).

altitudes close to the surface the FWHM is calculated as double the distance between the altitude of the kernel's maximum and the altitude above where it reaches its half value. Methane is well suited for analysis of atmosphere below 20 km with a typical FWHM as small as 11 km. The averaging kernels provide a wealth of information on the performance of the retrieval. The averaging kernels can be collected in the rows of a matrix called the averaging kernel matrix $\mathbf{A}$. Using $\mathbf{A}$ the retrieval is modeled by

$\hat{\mathbf{x}} = \mathbf{x}_a + \mathbf{A}(\mathbf{x}_T - \mathbf{x}_a)$. Hence the averaging kernel provides essential information about mapping of the true atmospheric state $\mathbf{x}_T$ to the retrieved atmospheric state $\hat{\mathbf{x}}$ (Fig. 6.3 right). The trace of the averaging kernel matrix provides another useful measure.

It gives the number of independent pieces of information retrieved from the measurement. For the spectra used to retrieve methane, the trace of the averaging kernel matrix is in the order of 2 to 2.4 indicating the possibility of retrieving up to 2.4 independent pieces of information.

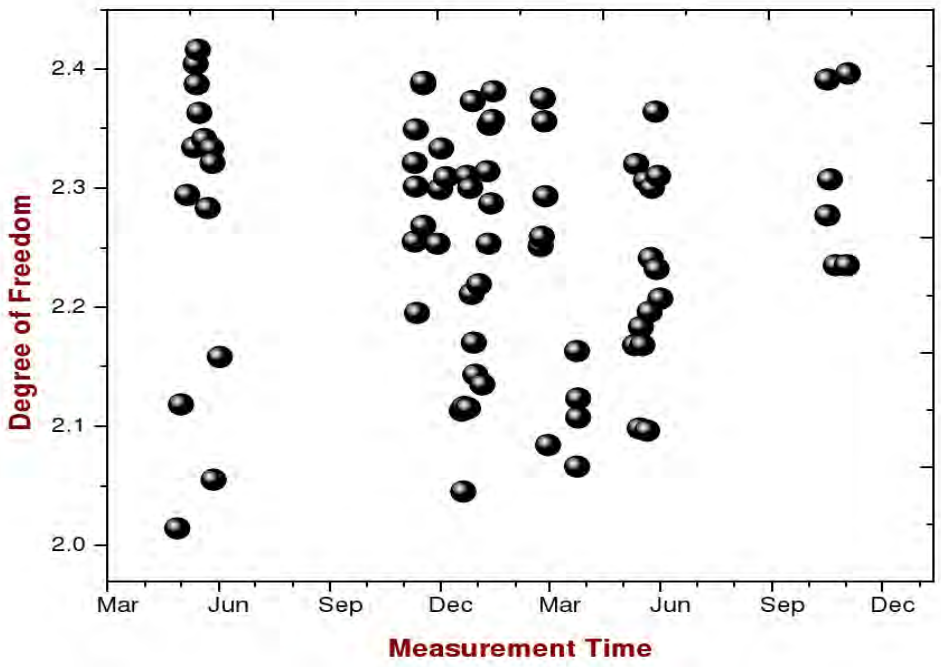

Figure 6.4: Degrees of freedom (DOF) retrieved during the measurement times.

In other words the methane averaging kernel **A**, shows sensitivity to the true profile from the lower troposphere up to the tropopause. The averaging kernels show that the FTIR is also sensitive to lower stratosphere with some piece of information. The FWHM (vertical resolution) is estimated at about 11 km. The averaging kernels also show that there is basically no information in the retrieval above 35 km.

The capability of the retrieved profile to describe the real profile can be better assessed by using some a priori information. The kernels of Fig. 6.3 are the response of the retrieved profiles on altering of the mixing ratio at the nominal height of the real profile by one arbitrary unit. If we try to estimate which altitude range of the real atmosphere is typically represented in the mixing ratio retrieved at a certain altitude level, it is necessary

to consider not only the averaging kernels but also the typical variability and the inter level correlations in the real atmosphere.

Correlating the real to their corresponding retrieved profiles allows us then to identify the altitude ranges in the real profile which are, from statistical point of view, mainly represented at a certain altitude level of the retrieved profile. For the typical kernels depicted in Fig. 6.3, CH_4 is well suited for analyzing the atmosphere below 20 km where the maximum correlation corresponds to the nominal altitude.

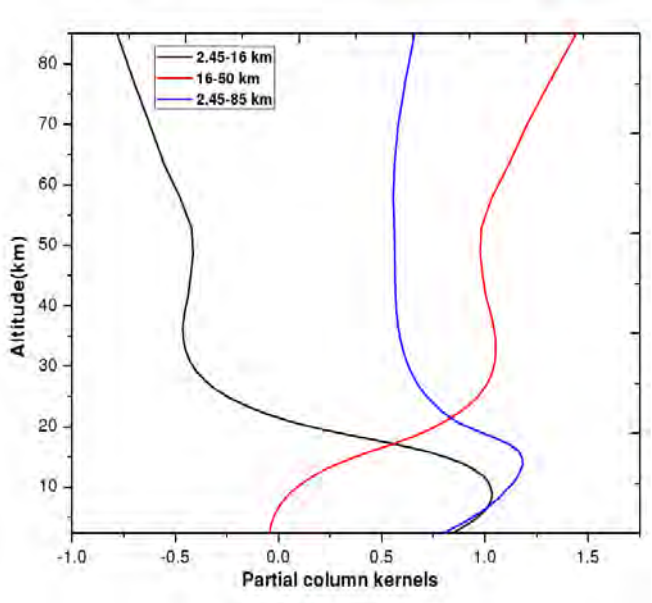

Figure 6.5: Sensitivity curves for CH_4 retrieval.

The sensitivity curve shows where the measurements contribute for at least 50% to the signal at each height. It covers from 2.45 to about 16 km for Addis Ababa.

6.2 Methane TCA time series analysis

Daily mean values of methane total column amount (TCA) for the period of May 2009 to Nov 2010 are given in Fig. 6.7. Minimal 2.47×10^{19} molecules cm^{-2} and maximal 3.8×10^{19} molecules cm^{-2} values of CH_4 TCA were observed in May 2010 and June 2009

respectively. We suppose that hot and dry winter of 2010 for Addis was the main reason of low methane total column amount (TCA) values.

Difference between maximal and minimal values Fig. 6.6 observed for each year was used as a measure of CH_4 TCA variability study. The difference value is compared on similar date data basis. To the decrease of methane TCA in the atmosphere can be attributed decrease of the source air mass flow from different sectors throughout the measurement period.

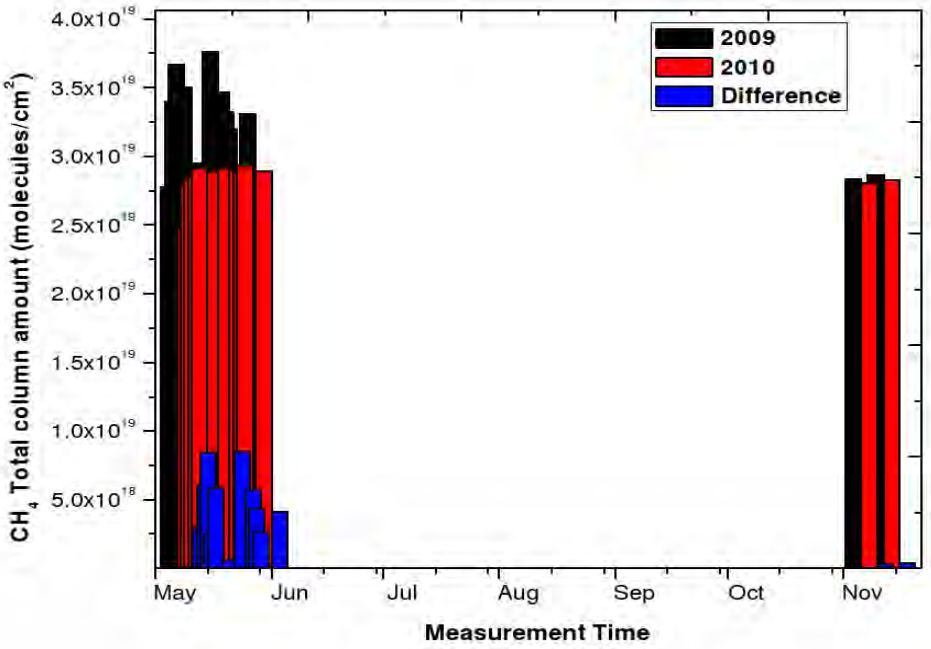

Figure 6.6: Histogram of the difference between maximum and minimum values of CH_4 observation.

The amplitude of the mean annual cycle of CH_4 TCA is about 26%. The inter seasonal cycles for 2010 are reasonably similar than 2009 differences. Such differences are caused by the variability of methane sources and sinks.

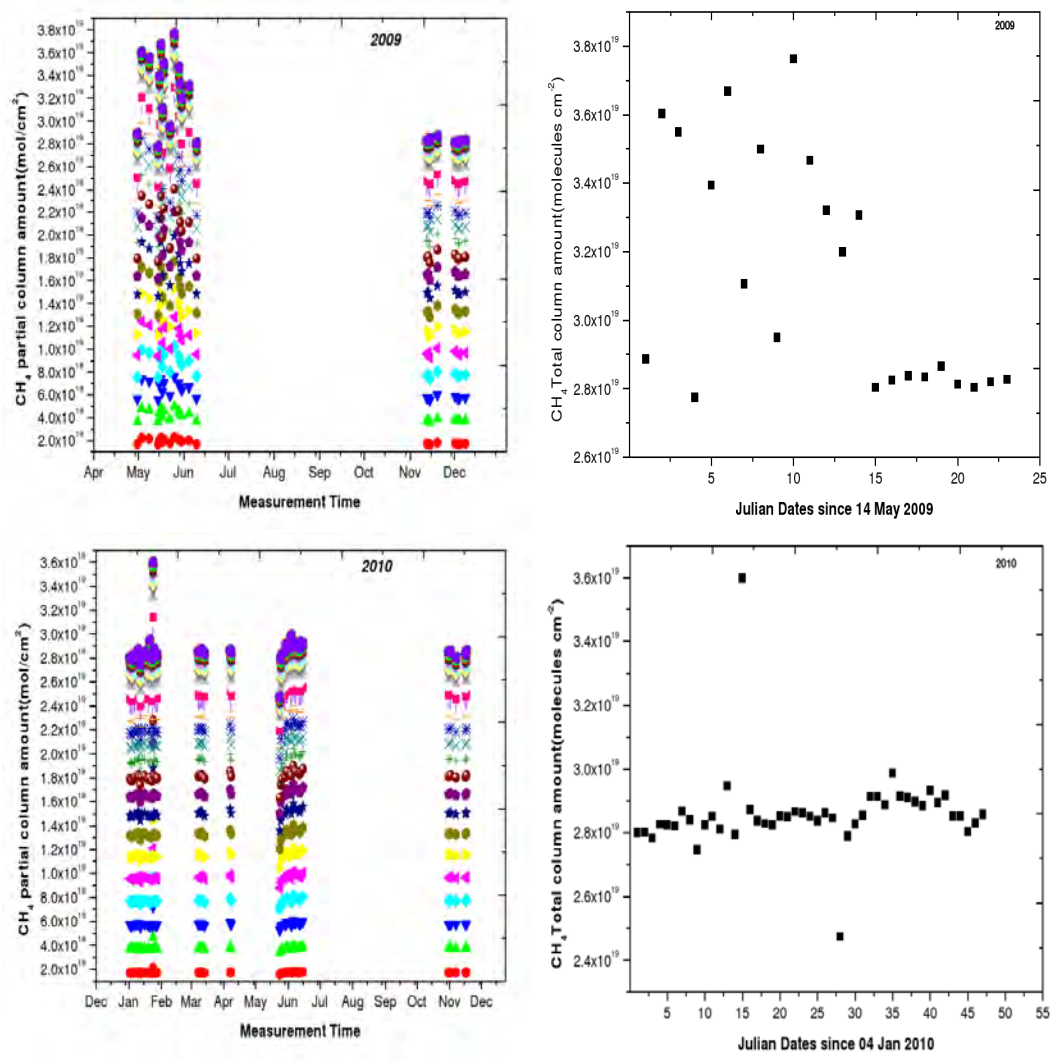

Figure 6.7: Partial (left) and total (right) column amounts of methane retrieval.

Air mass backward trajectory analysis was used to identify the source regions and to associate them with various levels of CH_4 pollution encountered for Addis. Measurement times of May, June 2009 and May 2010 with irregular disturbances of CH_4 TCA were chosen. For trajectory analysis we employed HYSPLIT-4 isentropic trajectory model of NOAA Air Resource Laboratory [http://www.arl.noaa.gov]. The HYSPLIT(Hybrid Single-Particle Lagrangian Integrated Trajectory) model is a newest and complete system for computing simple air parcel trajectories to complex dispersion and deposition simulations.

ARL's HYSPLIT model is a tool that helps explain how, where and when chemicals and materials are atmospherically transported, dispersed and deposited. Having this understanding is essential for responding appropriately and preventing disaster. For instance, accurate predictions of the path of a chemical release helps emergency managers evacuate the right people. Predictions of volcanic ash plume locations allow aircraft to avoid dangerous areas. Understanding the sources of hazardous air pollutants allows air quality managers to develop targeted policies and plans to mitigate the problem.

Five days backward trajectories were calculated for some elevations from the measurement site. Analysis of CH_4 TCA together with backward trajectories at different elevations show results for all trajectories are similar in general.

The backward trajectories displayed in Fig. 6.8 and 6.9 are good indicators of large scale flow. From the figures we suggest that air mass appears to be highly polluted by CH_4 when air originates from East and North Eastern regions of the country. While the air mass appears to be less polluted by methane when air originates from the South and North regions of the country.

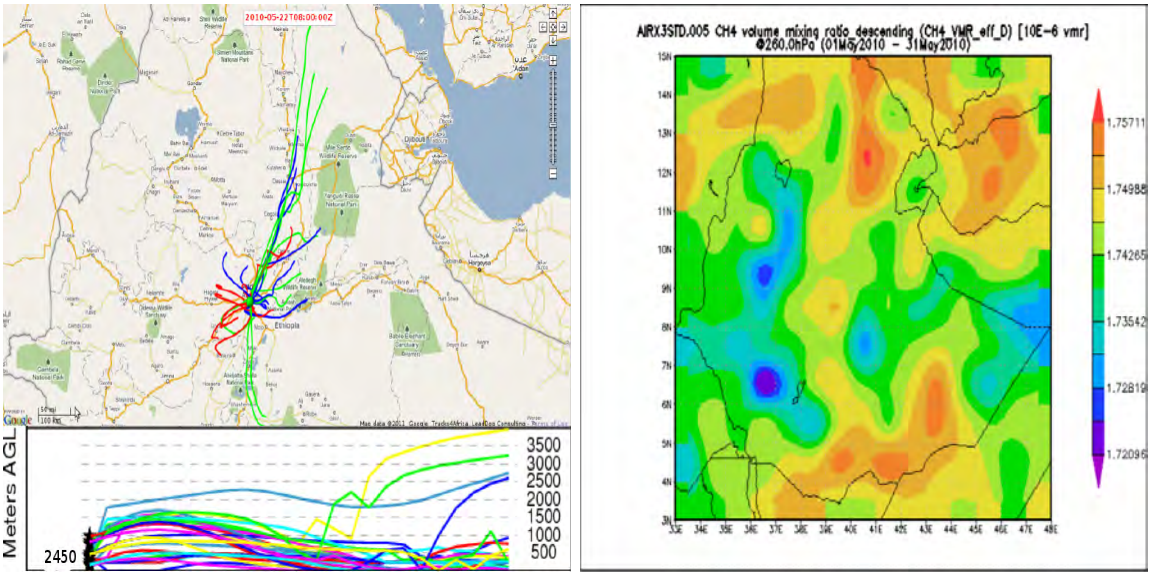

Figure 6.8: Backward trajectories for air mass flow sectors (left) and origin of air mass (right) during which minimum TCA of CH_4 is observed over Addis Ababa, May 26 2010.

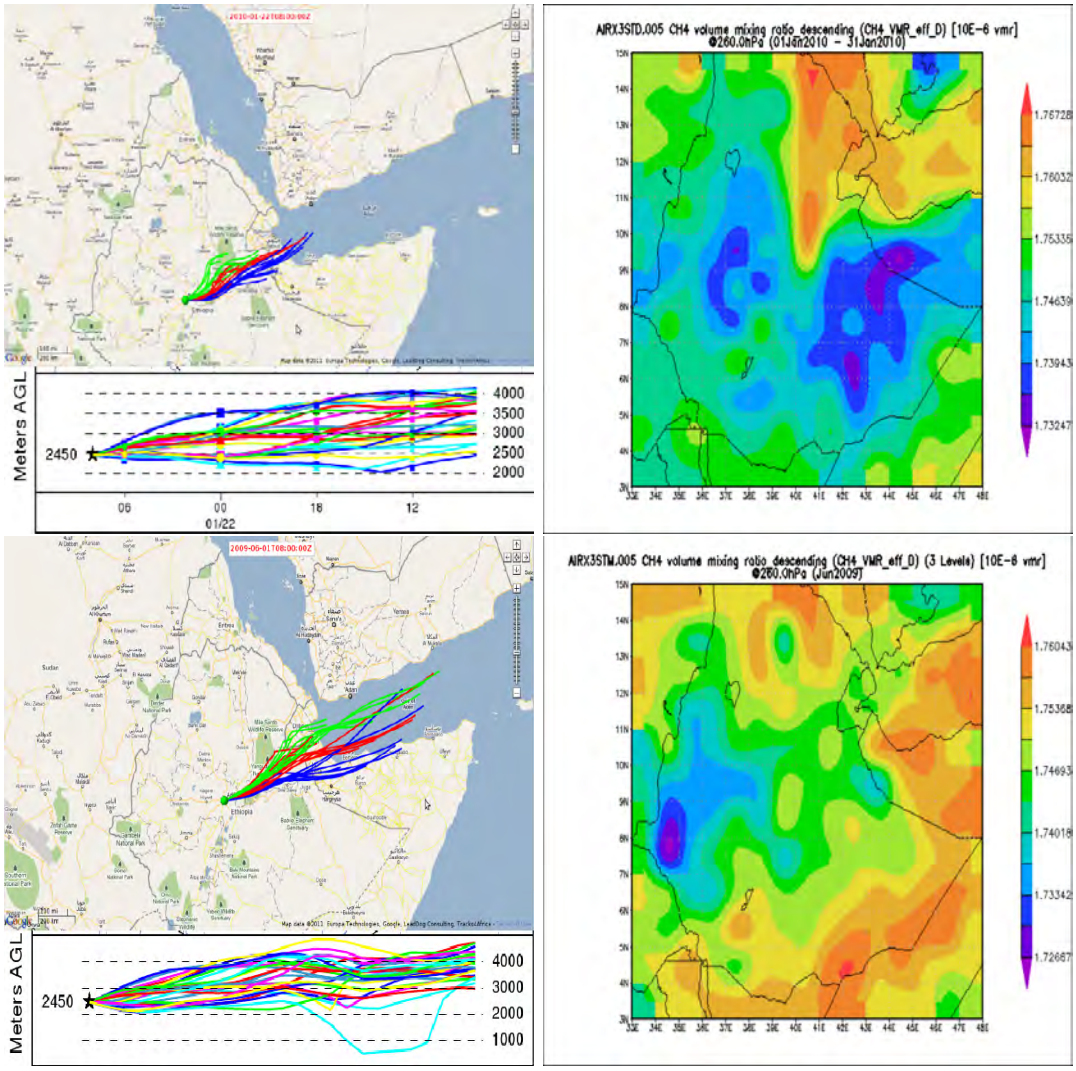

Figure 6.9: Backward trajectories for important air mass flow sectors and origin of air mass for Addis Ababa during which high CH_4 concentration is observed, January 26 2010 (top) and June 8 2009 (bottom).

Origin of the air mass for different sectors described above is also analyzed. Analyses and visualizations used in this study were produced with the Giovanni on line data system, developed and maintained by the NASA GES DISC (Godard Earth Sciences Data and Information Services Center) Interactive On line Visualization And Analysis Infrastructure. From the results obtained we suggest the air mass flow from the sectors is highly contaminated by methane during the months of May, June 2009 and January 2010. This is specially true when the air mass originates from the Gulf of Aden and Red sea areas,

where these regions are expected to be high methane sources. This results in the high concentration of methane observation over Addis during these two observation times.

6.2.1 Tropospheric CH_4 Time series

Fig. 6.10 shows the time series of the FTIR observed tropospheric column amount of methane from May 2009 until Nov 2010 over Addis Ababa.

Methane, which is long-lived and abundant at the lower altitudes shows annual cycles with gradually increasing and decreasing column amounts and low variability during summer. In winter small column amounts and large variabilities are observed. These observations indicate the pronounced upwelling and stable troposphere in summer and the more disturbed troposphere in winter. This is also linked to large emissions during summer from natural sources, biomass burning and ruminants.

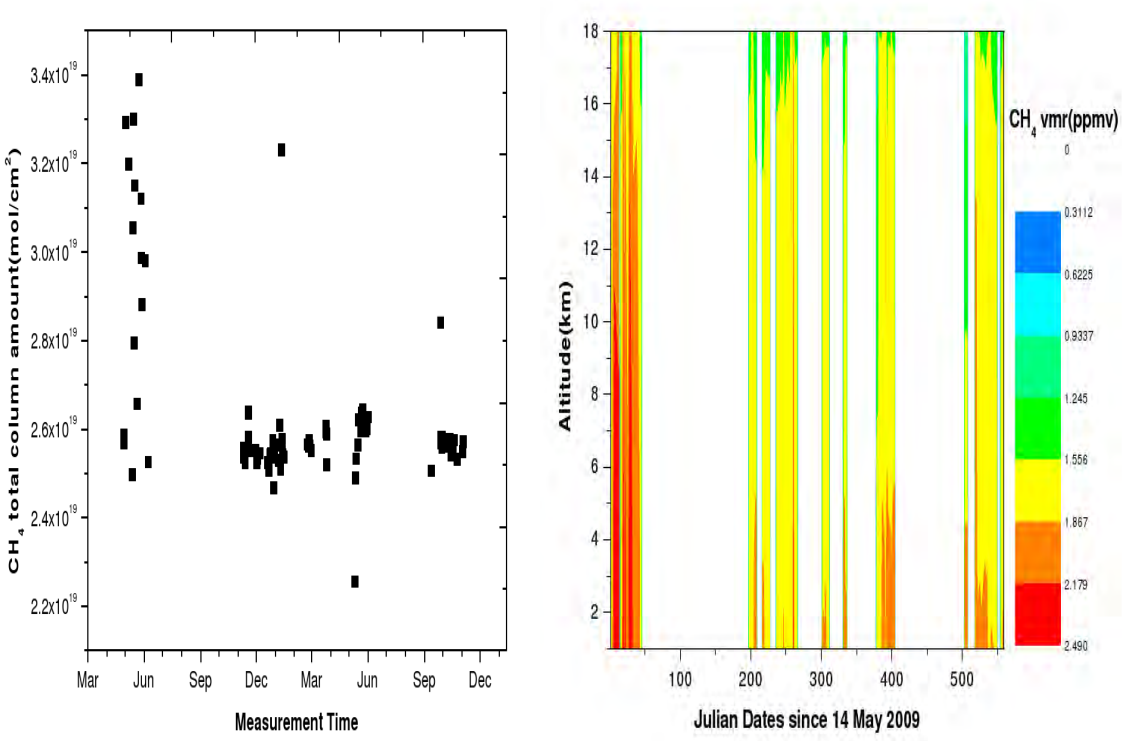

Figure 6.10: Tropospheric time series of CH_4 column amount (left) and vertical profile (right).

From Fig. 6.10 we observe that the tropospheric CA of CH_4 during the measurement times ranges from 2.2×10^{19}molecules cm^{-2} to 3.4×10^{19}molecules cm^{-2}. Low methane tropospheric column amount is expected in our region because of the distance from main methane sources (industrialized regions of the northern hemisphere). However, the high level of tropospheric CH_4 column amount is due to methane emissions from wet lands mostly during warm seasons and biomass burning.

6.2.2 CH_4 vertical profile time series

Even though we were unable to see the complete seasonal cycles (due to missing data), we tried to present time series of CH_4 for 82 measurement days since the start of FTIR operation in Addis. The time series of vertical profile of CH_4 from May 2009 to Nov 2010 is displayed in Fig. 6.11. Methane is the prominent greenhouse gas next to CO_2 and the most abundant organic compound in the atmosphere.

Owing to its long life time ($\approx$10 yrs), CH_4 is removed from the atmosphere primarily through oxidation by tropospheric OH and subsequent deposition of its products at the Earth's surface, and in the case of its constituent hydrogen (both atomic and molecular forms) by escape to space at the top of the atmosphere (TOA)[7]. Its photochemistry is important as it affects stratospheric water vapor levels, molecular hydrogen, CO and ozone levels. CH_4 oxidation is initiated by its reaction with OH and follows a sequence of reactions that lead to the production of formaldehyde, CH_2O, that is photolyzed to CO and molecular hydrogen (Fig. 3.3).

Reaction of CH_3O_2 with NO produces NO_2 that photolyses to produce atomic oxygen as a net effect and thus an important source of ozone in the lower stratosphere [42].

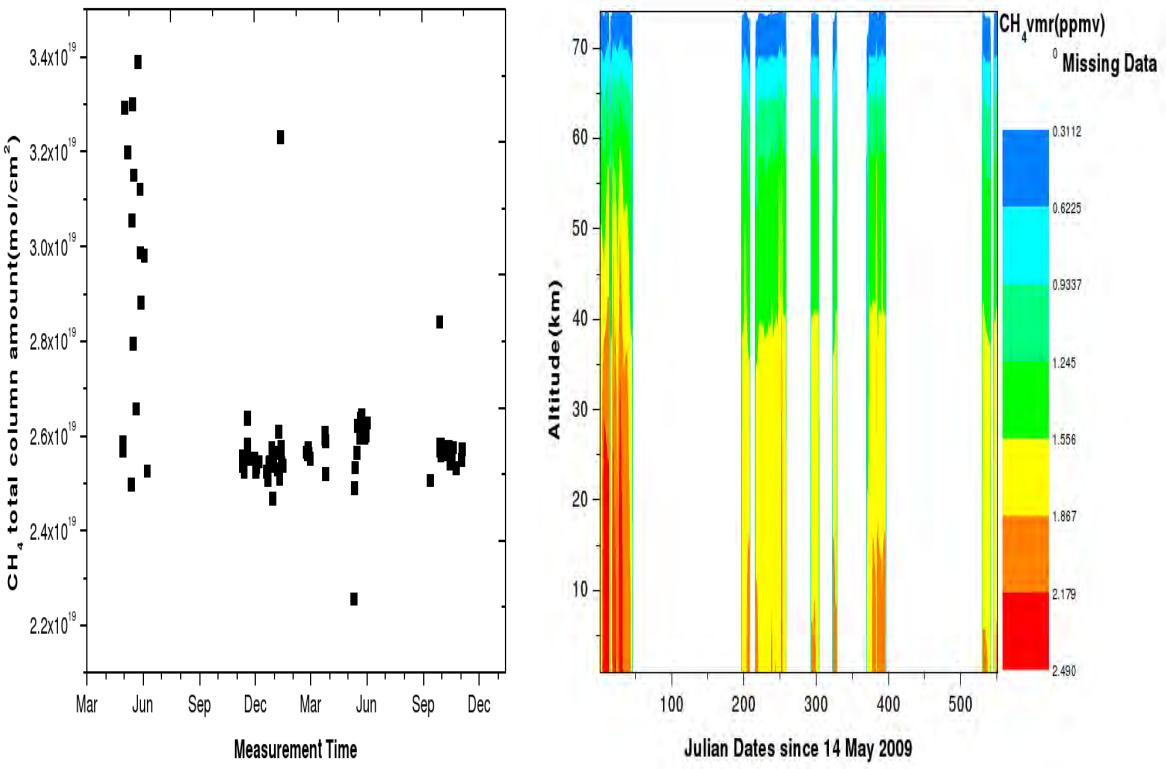

Figure 6.11: Time series of CH_4 total column (left) and vertical profile (right).

The time series of the vertical profile for methane for the above mentioned measurement periods is shown in Fig. 6.11. As indicated in this figure the mixing ratio reaches up to 2.49 ppmv, (this is slightly lower than the value reported in [43]) at the observation point and rapidly decreases within the stratosphere.

As we mentioned before oxidation by tropospheric hydroxide radical (OH) is the main atmospheric sink of CH_4. Methane is destroyed in the lower atmosphere by oxidation. It then undergoes a second major decrease above 80 km due to photolysis and reaction with $O(^1D)$. The conversion of methane into ozone in the lower stratosphere is also one of the sink mechanisms of this gas. The important roles of lower stratospheric and tropospheric methane in influencing the Earth's radiation budget and its reaction involved in ozone chemistry [42] have drawn attention to the sinks and sources of CH_4.

6.3 Error Analysis

A retrieval does not preserve details of true atmospheric state due to errors. Any error modifies the spectrum and there by disturbs the retrieved quantities.

The error analysis of this work is based on OE [34] according to which the error in the retrieved profiles is separated into three components: errors due to uncertainties in the input parameters applied in the inversion procedure, errors due to measurement noise, and errors due to the inherent finite vertical resolution of the observing system (instrument), subsequently called the smoothing error.

Model input parameters

Input parameters are solar elevation angle, temperature profile, instrumental line shape (ILS), and spectroscopic line parameters. Discrepancies between the angle under which the solar radiation enters the instrument and the actual solar elevation angle, which is applied in the retrieval may occur when the instrument aperture is not centered on the solar disk. For the error estimations, an uncertainty of 0.5^o was assumed in the radiative transfer code.

For solar zenith angle (SZA) or line of sight (LOS) greater than 80^o the error in the mixing ratio can exceed 8% for tropospheric gases, where as it is less than 2% for stratospheric gases at all altitudes. The LOS error which significantly affects the retrieval in the low latitudes is less than 0.1% [29]. Temperature uncertainties of 0.7K near the surface and in the upper troposphere are assumed. They arise from the limited accuracy and mismatch in time and space for the air masses detected by the FTIR. Both column amount and shape of the profile are influenced by temperature uncertainty, such that the change in temperature profile affects the pressure which in turn affects the number density of the molecules. The modulation efficiency and phase error are assumed to be determined by the cell measurements at an accuracy of 0.01% and 0.01 mrad respectively.

Spectroscopic line parameters, that lead to systematic deviation of the actual profile, are taken with an assumed accuracy of 1%.

Measurement noise

Noise in the measured spectrum has an important impact on the quality of the measurement as well as retrieval. The spectral noise is due to the uncertainty of the depth of the absorption line with respect to its surrounding continuum, which is proportional to the uncertainty in line strength. The uncertainty in line strength in turn is proportional to the uncertainty of scaling factor, for scaled retrieval of the profile.

For strong absorbers like CH_4, N_2O, HCl, O_3 the error due to noise has a value less than 1.5%, for weak absorbers like $ClONO_2$, NO_2 this uncertainty is slightly above 12% [29]. The random (statistical) and systematic errors of the retrieval are shown in Fig. 6.12.

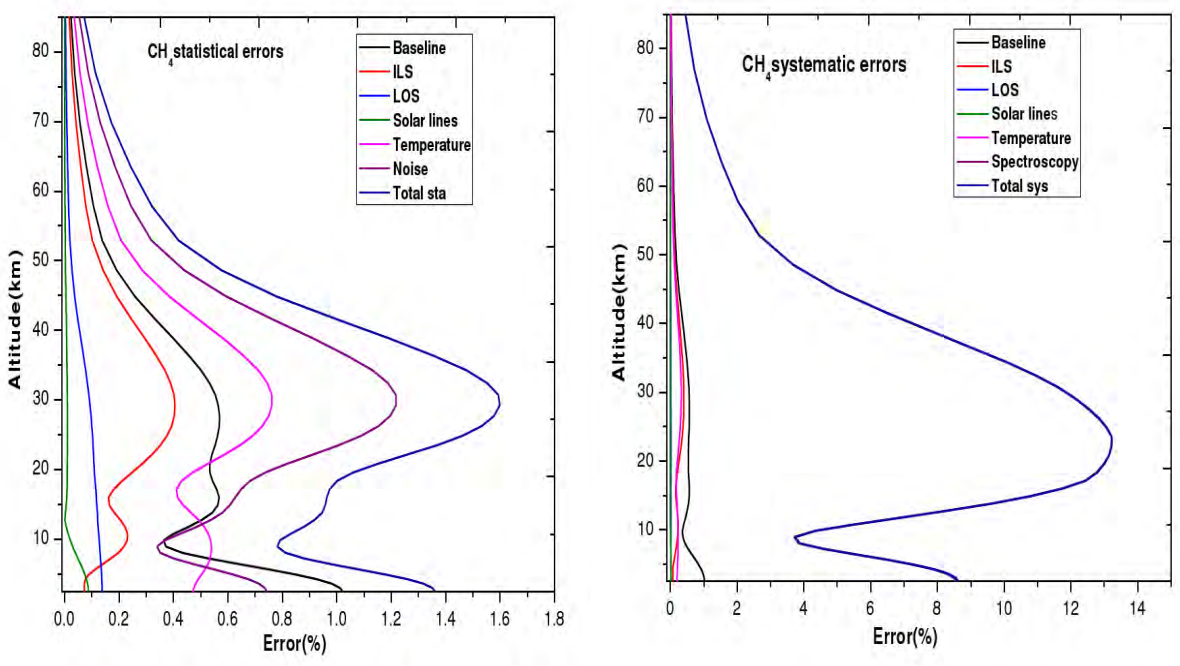

Figure 6.12: Statistical and systematic error budgets for the retrieval of CH_4.

The error quantities to be dealt here are spectral baseline (offset,channeling), ILS (linear modulation and constant phase error), LOS, error due to temperature, spectroscopic data and noise.

Table 6.3: Statistical error budget(in %) for methane retrieval at some selected altitudes.

Altitude(km)	BaseLine	ILS	LOS	SolarLines	Tmp	Noise	TotalSta
2.45	1.3	0.7	0.1	0.1	0.5	0.70	1.50
2.94	1.3	0.1	0.1	0.1	0.5	0.70	1.50
3.56	1.2	0.07	0.1	0.1	0.45	0.67	1.49
6.38	0.7	0.17	0.1	0.06	0.51	0.40	0.99
7.18	0.6	0.22	0.1	0.05	0.52	0.33	0.87
8.01	0.5	0.23	0.1	0.04	0.54	0.29	0.8
8.88	0.4	0.29	0.1	0.02	0.55	0.3	0.8
9.78	0.4	0.3	0.1	0.02	0.56	0.35	0.85
18.31	0.5	0.22	0.09	0.01	0.47	0.54	0.92
30.69	0.6	0.49	0.07	0.01	0.80	1.16	1.64
69.77	0.07	0.07	0.01	0.00	0.1	0.13	0.18
85.00	0.03	0.02	0.003	0.001	0.04	0.05	0.08

Table 6.4: Systematic error budget(in %) for methane retrieval at some selected altitudes.

Altitude(km)	BaseLine	ILS	LOS	SolarLines	Tmp	Spect	TotalSyst
2.45	1.3	0.07	0.01	0.03	0.2	9.45	9.51
2.94	1.3	0.07	0.01	0.03	0.2	9.40	9.50
3.56	1.25	0.07	0.01	0.03	1.94	9.38	9.47
6.38	0.72	0.17	0.01	0.12	0.22	5.8	5.83
7.18	0.6	0.22	0.01	0.21	0.22	4.62	4.67
8.01	0.5	0.26	0.12	0.01	0.23	3.76	3.81
8.88	0.4	0.29	0.01	0.01	0.24	3.68	3.72
9.78	0.43	0.3	0.01	0.001	0.24	4.53	4.6
18.31	0.53	0.22	0.1	0.03	0.2	13.15	13.17
30.69	0.63	0.49	0.01	0.00	0.36	10.48	10.51
69.77	0.69	0.05	0.00	0.00	0.04	0.96	0.97
85.00	0.03	0.02	0.0	0.0	0.02	0.39	0.40

From the figures we see that the error contributions from ILS, LOS and solar lines are relatively very small when compared to the others. Summaries of the error contributions are given in Tables 6.3 and 6.4.

Generally the statistical and systematic errors of the parameters used in the retrieval procedure is less than 15% out of which about 13.2% is spectroscopic from systematic contribution. Whereas the total random error contribution is less than 2% (i.e.,1.5%).

For single profile, uncertainties in ILS, and line parameters are responsible for systematic errors. Below $\sim$ 20 km for the tropospheric source gas (CH_4), the systematic line parameter errors closely exceed the estimated precision. This confirms that the uncertainties in the line parameters dominate the error for tropospheric gases. The results reported for both systematic and statistical error contributions confirm the result is accurate.

6.4 Methane Total Column Amount Validation

The retrieved total column amount(TCA) obtained from our ground-based FTIR Spectrometer measurements have been compared with the retrieved total column amounts obtained from the Atmospheric Infra-Red Sounder (AIRS) satellite.

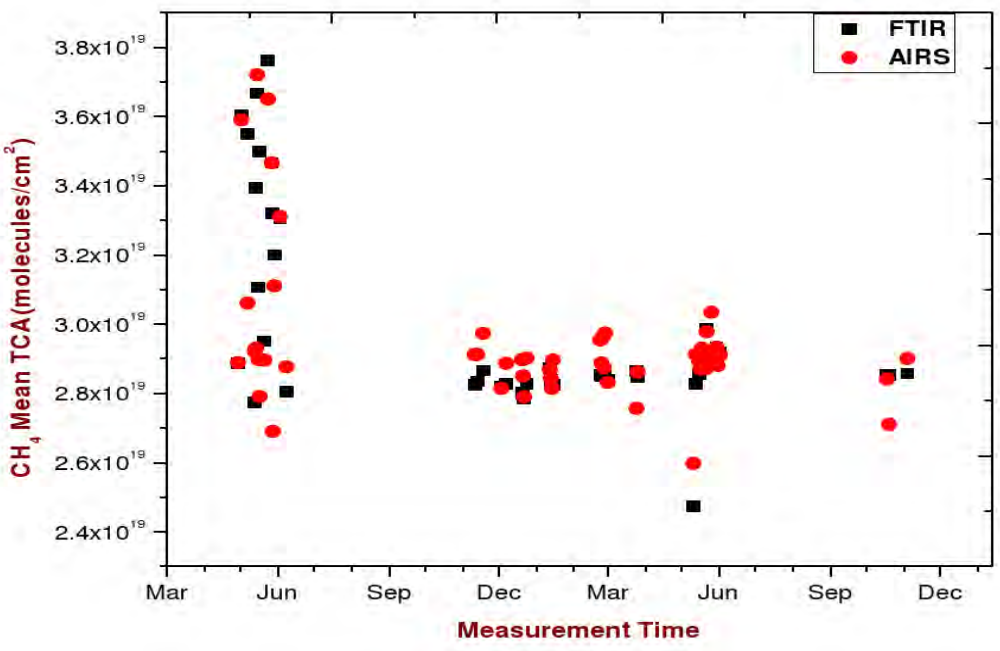

Figure 6.13: The comparison of the retrieved TCA from the spectra of AIRS and FTIR.

The criteria we set for validation is spatial collocation between the records of the two instruments. Hence, the spatial collocation we used is 8.9^o to 9.2^o in latitude and 38.5^o to 39^o in longitude. Daily mean TCA of CH_4 obtained from both of the instruments are are used for comparison.

Then the comparison result is displayed in Figure 6.13, where the black squares indicate the total column amount of methane retrieved from FTIR while the red dots indicate the retrieved total column amount of methane from AIRS record. From the Figure we observe that the retrieved results are fairly in agreement.

The methane measurement from ground-based FTS shows strong correlation with the observation of AIRS. This correlation is displayed in Fig. 6.14.

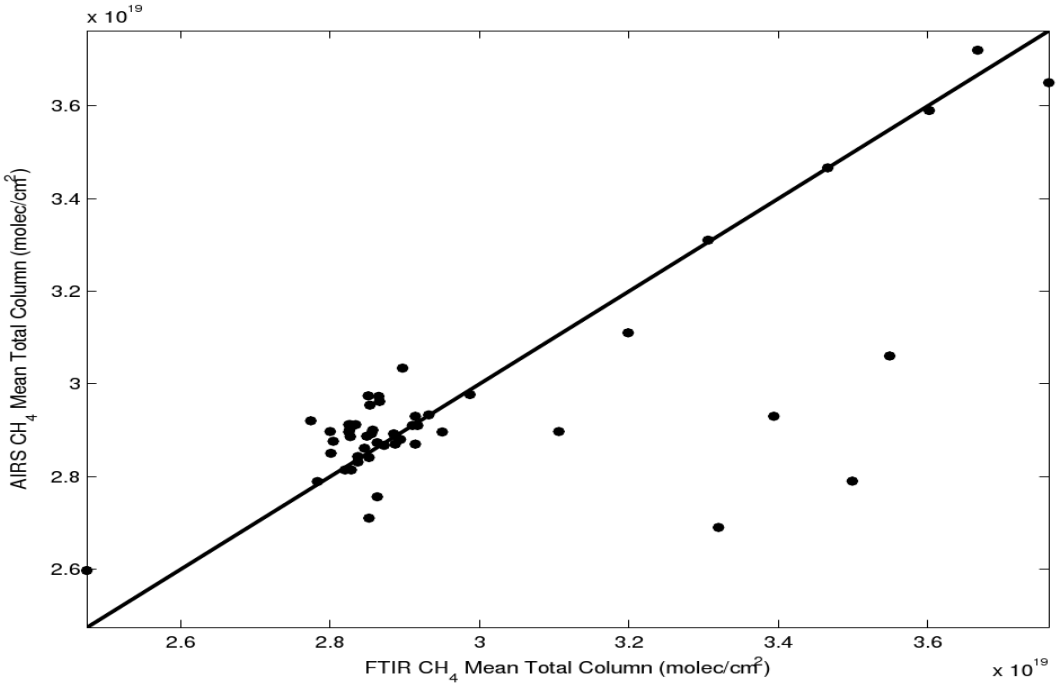

Figure 6.14: Correlation of AIRS and FTIR CH_4 mean total column with r=+0.80.

Chapter 7

Conclusion

Methane is a colorless inflammable gas, is most abundant in the troposphere. It is a strong greenhouse gas and an important source of stratospheric water vapor and tropospheric ozone that contribute to global warming. On a per molecule basis, additional methane is much more effective as a greenhouse gas than additional CO_2. The concentration of methane has doubled since pre-industrial times. The atmospheric mixing ratio of methane is currently 1.90 ppmv. This increase is attributed to the intensified human activity in agriculture, biomass burning, and fossil fuel consumption.

In this work, we have described different basic concepts related to atmospheric methane retrieval and characterization. Retrieval theory needs an indirect measurement in order to derive the required atmospheric parameter. The retrieval simulation has been done based on Tikhonov-Philips regularization and optimal estimation which describe the relationship between the remote measurements and the true atmospheric state, with thorough error analysis involved. The spectra used for the retrieval of methane are recorded between May 2009 and Nov 2010 using high resolution FTS at Addis Ababa. The performance of the instrument is regularly checked by ILS and phase error. The real ILS of the instrument is determined nearly regularly from low pressure HBr cell measurement using a laboratory source (glow bar $\approx$ 1273 K) using the latest version of LINEFIT12 software. The ILS itself is characterized by modulation efficiency loss and phase error.

The phase error is less than 3 mrad except for 10 March 2010 where there is a slight miss alignment in the instrument causing an error of about 9 mrad. Similarly the modulation efficiency declination at the maximum OPD is less than 6% on 10 March 2010 and it is below 1% for the rest of the measurement dates indicating permanent alignment of the instrument during the measurement time. The HBr spectral fit for (2432.20-2432.60) cm^{-1} wavenumber region shows a nice fit between the measured and calculated transmission spectra. The RMS value of the residual is less than 0.3% and it is comparable to the result reported on [29].

The retrieval code we used in this thesis (PROFFIT95) allows to choose between different regularization techniques and handling of different error quantities. The spectral fit between the measured and calculated spectra of CH_4 is also discussed and the maximum error between the measured and calculated spectra for all micro windows of the species is less than 4%, which guarantees fit quality. The vertical profile, information content, total and partial column amounts and seasonal variability of CH_4 from the FTIR spectra measured over Addis Ababa are presented. Extreme events are selected and origins of air mass flow for those particular measurement dates is identified with the help of ARL's HYSPLIT model indicating that these extreme events are due to high (or low) methane contamination that originated from different sectors. Biomass burning and wetlands are the two methane sources most likely to influence short-term methane cycles.

The statistical and systematic error contributions were analyzed for baseline, ILS, LOS, solar line, noise, temperature and spectroscopic data and we found a total percentage error of less than 2% for statistical and less than 14% for systematic.

The total column amount of CH_4 retrieved from our ground-based FTIR measurement is compared with data obtained from AIRS. Results of the two instruments agree well with a correlation coefficient of 0.8.

Bibliography

[1] A. Wiacek (2006). *First Trace Gas Measurements Using Fourier Transform Infrared Solar Absorption Spectroscopy at the University of Toronto Atmospheric Observatory*;a PhD.Dissertation, Department of Physics,UOT.

[2] http://acmg.seas.harvard.edu/people/faculty/djj/books.

[3] Arito H.,I Uchiyama et al.,*Toxicology Letters*, Journal of Japan Society for Atmospheric Environment, **38**,347-357,2003.

[4] World Meteorological Organization, *Scientific assessment of ozone depletion*: 1998, WMO, Geneva, 1999. *Models and long-term trends of tropospheric* O_3.

[5] Intergovernmental Panel on Climate Change, Climate Change 1994, Cambridge University Press, 1995. *Global budgets of tropospheric gases.*

[6] Seinfeld, J.H., and Pandis, S.N.(2006). *Atmospheric Chemistry and Physics; From Air pollution to climate change*, A Wiley-Interscience Publication, 2nd Edition.

[7] I.M Vardavas,and F.W.Taylor (2007). *Radiation and Climate.* International Series of Monographs on Physics; Oxford University Press.

[8] John M. Wallace, Peter V. Hobbs.(2006).*Atmospheric science : an introductory survey -2nd ed.*.University of Washington.

[9] Liou, K.N.(2002). *An Introduction to Atmospheric Radiation*, 2nd Edition, International Geophysical Series, Vol.84, Academic press, New York.

[10] W.Demtröder.(2006). *An Introduction to Atomic-, Molecular-and Quantum-Physics.*

[11] W.G.Rees.(2001). *Physical Principles of Remote Sensing*,2nd Edition,Cambridge University Press.

[12] Dr. F. M. Miskolczi (1989). *High Resolution Atmospheric Radiative Transfer Code (HARTCODE).*,Technical Report.

[13] Chandrashekar S. : *Radiative Transfer*. Dower Pub. Inc. New York (1960).

[14] R. M. GOODY and Y. L. YUNG.*Atmospheric Radiation;Theoretical Basis-2nd ed.*Oxford University Press.

[15] Donald J. Wuebbles and Katharine Hayhoe.*Atmospheric Methane: Trends and Impacts.*Department of Atmospheric Sciences, University of Illinois, Urbana, IL.

[16] IPCC, 2001: Climate change 2001: The scientific basis. Contribution of working group I to the third assessment report of the Intergovernmental Panel on Climate Change. Houghton, J. T., Ding, Y., Griggs, D. J., Noguer, M., van der Linden, P. J., Dai, X., Maskell, K. and Johnson, C. A. (ed.), Cambridge University Press, Cambridge, United Kingdom and New York, NY, USA.

[17] S. George Philander.(2008). *Encyclopedia Of Global Warming and Climate Change.*Volunes 1-3.

[18] Bartlett, K. and Harriss, R. (1993). *Review and assessment of methane emissions from wetlands.* Chemosphere. 26, 261-320.

[19] Cole, C., Duxbury, J., Freney, J., Heinemeyer, O., Minami, K., Mosier, A., Paustian, K., Rosenberg, N., Sampson, N, Sauerbeck, D. and Zhao, Q. (1997). *Global estimates of potential mitigation of greenhouse gas emissions by agriculture. Nutrient Cycling in Agroecosystems.* 49, 221-228.

[20] Ward, G., Doxtader, K., Miller, W. and Johnson, D. (1993). *Effects of intensification of agricultural practices on emission of greenhouse gases.* Chemosphere. 26, 87-93.

[21] Bogner, J., Spokas, K., Burton, E. Sweeney, R. and Corona, V. (1995). *Landfills as atmospheric methane sources and sinks.* Chemosphere. 31, 4119-4130.

[22] Peer, R., Thorneloe, S. and Epperson, D. (1993). *A comparison of methods for estimating global methane emissions from landfills.* Chemosphere. 26, 387-400.

[23] Levine, J.S., Cofer III, W.R . and Pinto, J.P. (1993). *Biomass burning. In 'Atmospheric Methane: Sources, Sinks and Role in Global Change.*' (Eds. M. Khalil), 299-313. (Springer-Verlag, New York, NY).

[24] Beck, L.L., Piccot, S.D. and. Kirchgessner, D.A (1993). *Industrial sources. In 'Atmospheric Methane: Sources. Sinks and Role in Global Change.*' (Eds. M. Khalil) pp. 399-341. (Springer-Verlag, New York, NY).

[25] Crutzen, P., and Bruhl, C. (1993). *A model study of the atmospheric temperatures and concentrations of ozone, hydroxyl, and some other photochemically active gases during the glacial, the pre-industrial Holocene and the present.* Geophysical Research Letters. 20, 1047-1050.

[26] *Intergovernmental Panel on Climate Change. (1996). Climate Change 1995: the Science of Climate Change.* (Eds. J. T. Houghton, L. G. Meira Filho, B. A. Callander, N. Harris, A. Kattenberg, and K. Maskell). 572 pp. Cambridge University Press, Cambridge, U.K.

[27] Prather, M. (1994). *Lifetimes and eigenstates in atmospheric chemistry.* Geophysical Research Letters. 21, 801-804.

[28] Gezahegn S.(2010). *Observation of Atmospheric Carbon monoxide by Ground-based FTIR Spectrometer over Addis Ababa,Ethiopia.* MSc.thesis,Physics Department, Addis Ababa university.

[29] Milkesa G.(2010). *Stratospheric Aerosol Climatology from SAGE II and Observation of its Deriver OCS,Over Equatorial Africa.* MSc.thesis,Physics Department, Addis Ababa university.

[30] J. Kauppinen, J. Partanen.(2001). *Fourier Transforms in Spectroscopy.*

[31] S.Al-Hazaimay.(2008). *Impact of Instrumental Parameters on Atmospheric Trace Gas Retrievals using FTIR Spectroscopy.* Institute of Environma=ental Physics,University of Bremen,Bremen,Germany.

[32] Gang Li.(2003). *FT Spectroscopy of Selected Transient Species..*A PhD.Dissertation,University of Waterloo,Waterloo,Ontario,Canada.

[33] Griffith,et al.,(2003). *Intercomparison of NDCC Ground-Based Solar FTIR Measurements of Atmospheric Gases at Lauder,New Zealand.* Journal of Atmospheric and Oceanic Technlogy. **20**,1138-1153.

[34] Rodgers, C. D.: Inverse Methods for Atmospheric Sounding: Theory and Practice, World Scientific Publishing Co., Singapore, 2000.

[35] Richard C. Aster, Brian Borchers, and Clifford H. Thurber.(2005). *Parameter Estimation and Inverse Problems.*Elsevier Academic Press.

[36] Tilman Steck and Thomas von Clarmann,*Constrained Profile Retrieval applied to MIPAS Observation Mode.*

[37] P. C.Hansen. *Analysis of discrete ill-posed problems by means of the L-curve.* SIAM Review, 34:561-580, 1992.

[38] A. Dudhia and B. M. Dinelli. *Optimisation of the Atmospheric Vertical Grid.* Technical report, ESA, 1997. Draft Final Report.

[39] G. H. Goluband W. Kahan. *Calculating the singular values and pseu- doinverse of a matrix.* SIAM J . Numer. Anal. Ser. B, 2, pages 205-224, 1965.

[40] Tilman Steck.(2002). *Methods for determining regularization for atmospheric retrieval problems.* Applied Optics Vol. 41, No. 9.

[41] L. S. Rothman et al,. *The HITRAN 2006 molecular spectroscopic database.*

[42] Harold Johnston and Douglas Kinnison, *Methane photooxidation in the atmosphere: Contrast between two methods of analysis.*Journal Of Geophysical Research, VOL. 103, NO. D17, PAGES 21,96721,984, September 20, 1998.

[43] Wondimu A. (2009). *Methane VMR and Climatology of Aerosols Over Tropical Latitudes From Remote Sounders.* MSc.thesis,Physics Department,Addis Ababa University.

[44] Raymond M. (1992). *Laser Remote Sensing*, Fundamentals and Applications. J.Wiley and Sons,Inc.

Declaration

This thesis is my original work, has not been presented for a degree in any other University and that all the sources of material used for the thesis have been dully acknowledged.

Name: Endale Gemechu

Signature:————————————.

Place and time of submission: Addis Ababa University, June 2011

This thesis has been submitted for examination with my approval as University advisor.

Name: Dr.Gizaw Mengitu

Signature:————————————.